Geology, petrology and geochemistry of the accreted Paleozoic greenstones in the Hangay region, central Mongolia

博士論文

Geology, petrology and geochemistry of the accreted Paleozoic greenstones in the Hangay region, central Mongolia

（モンゴル中央部ハンガイ地域の古生代付加体緑色岩の地質学,
岩石学及び地球化学）

Ganbat Erdenesaihan

平成２５年

ABSTRACT

The vast territory of Mongolia occupies a large part of the Central Asian Orogenic Belt (CAOB) or Altaids, that developed between the Siberian Craton to the north and the Tarim and Sino-Korean Cratons to the south. Tectonic history of the CAOB has important implications for the growth mechanisms of continental crust in Eurasia. The Hangay-Hentey belt is situated in central Mongolia and made up of a Pacific-type accretionary orogen, which were formed through evolution and closure of the Hangay-Hentey paleo-ocean in the period from Paleozoic to Early Mesozoic. From this belt, new geochemical and petrological results are presented for greenstones from the Erdenetsogt Formation hosted by the Tsetserleg accretionary terrane in the Hangay region with particular emphasis on newly found picritic and andesitic rocks. These rocks occur mostly in the lower portion of Erdenetsogt Formation as massive lavas, sills, and dikes closely associated with varicolored bedded ribbon-cherts and siltstones. The protoliths of the studied greentones comprise (1) enriched, plume-derived tholeiitic greenstones including picrites and ferrobasalts with oceanic plateau basalt affinity, (2) non-enriched, plume-derived tholeiitic basalts with E-MORB affinity, and (3) arc-derived high-Mg andesites (HMAs). The plume-derived rocks are characterized by chemical signatures such as slight LREE enrichment similar to that of tholeiitic OIB and the existence of ferropicrite with high FeO* (>14 wt%) and MgO (12-22 wt%), which is characteristic of large igneous provinces (LIPs) including oceanic plateaus. Their tholeiitic composition and high-Fe and -Ti contents require melting of the source mantle peridotite with addition of some recycled Fe- and Ti-rich basaltic material. The non-enriched basalts may have been generated by a higher degree of melting of the same source mantle. The HMAs are characterized by glassy texture, high MgO content (up to 7 wt%), and significant LREE enrichment with depletion in Nb, and resemble sanukite of the Setouchi volcanic belt, SW Japan. I infer that the Hangay tholeiitic greenstones probably represent an accreted upper section of an oceanic plateau, that developed in the deep-water region of the Hangay-Hentey paleo-ocean in the Devonian. In contrast, the Hangay HMAs may have been produced by subduction of young oceanic plate, which took place after an oceanward back-stepping of the subduction zone that was a result of the collision of the oceanic plateau and the active continental margin of the Central Mongolian Massif during the Carboniferous.

TABLE OF CONTENTS

LIST OF FIGURES

LIST OF TABLES

CHAPTER 1 INTRODUCTION

1.1 Background

The vast territory of Mongolia occupies a large part of the Altaids (Şengör et al., 1993; Şengör and Natal'in 1996; Yakubchuk, 2004) or Central Asian Orogenic Belt (CAOB) which extends from the Ural Mountains to the Pacific Ocean and from the Siberian craton to the Tarim and Sino-Korean cratons and which formed by the accretion of island arcs, ophiolites, oceanic islands, seamounts, accretionary wedges, oceanic plateaus, and microcontinents (Zonenshain et al., 1990; Mossakovsky et al., 1994; Zorin, 1999; Badarch et al., 2002; Khain, 2002; Windley et al., 2007; Xiao, 2008) (Fig. 1.1). The CAOB is probably the largest accretionary orogeny of earth, which evolved from about 1 Ga to 250 Ma (Windley et al., 2007), and thus overlaps in time with the accretionary orogeny of the Japanese Islands. The origin and evolution the CAOB is still controversial and two main models merge to account for the evolution of the CAOB (see review of Wilhem et al., 2012): 1) tectonic duplication and amalgamation of one or several major arcs of same origin; and 2) multiple amalgamation of many microcontinents and island arcs of different origins.

The Hangay-Hentey (or Khangai-Khentei in some literature) belt is located in central Mongolia (Fig.2.1) and records a progressive accretionary orogeny of the CAOB from the Middle Cambrian to the Early Mesozoic. In recent years, numerous oceanic crust fragments have been found and identified within this belt, especially in the Hentey region. Nevertheless, the geology and petrology of its western part (Hangay region) that comprises a Devonian-Carboniferous accretionary complex remain unstudied. In the 1990s, some basaltic greenstones intercalated with siliceous-turbidite-terrigenous sequences were reported from the lower portion of the thick Erdenetsogt Formation (~4000 m) of the Tsetserleg terrane of the Hangay-Hentey belt during 1:50,000 scale geological mapping in the southern flank of the Hangay Range (Lhundev et al., 1994). However, the geochemistry of these greenstones has not been studied in detail, except for brief descriptions by Orolmaa and Erdenesaikhan (2008) and Tsukada et al. (2013). The geochemical characteristics of Middle Paleozoic greenstones are of particular interest for understanding the geodynamic evolution of western end of the Hangay-Hentey belt (Orolmaa et al., 2008; Safonova et al., 2009, 2012). To address these issues, geological fieldworks were conducted in summers of 2011 and 2012 in the Uyanga area of the southern Hangay region.

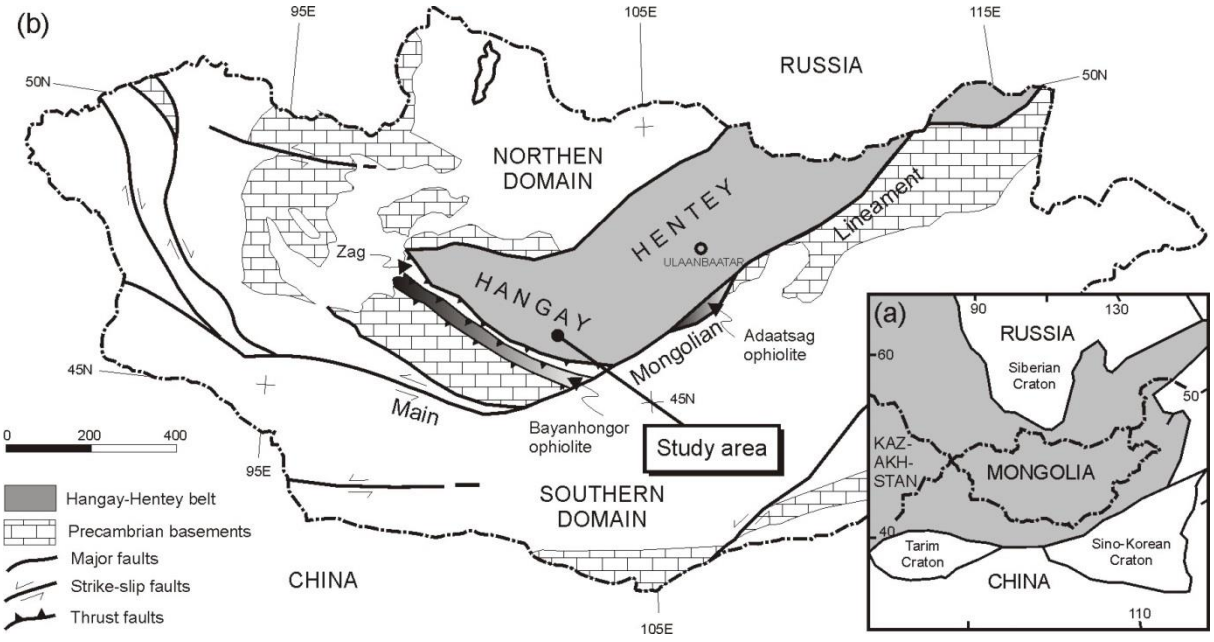

Figure 1.1 (a) Insert map showing outline of the Central Asian Orogenic Belt (CAOB) as shaded area and surrounding Precambrian Cratons, and location of Mongolia. (b) Simplified lithotectonic map of Mongolia, showing the location of the Hangay-Hentey belt (Modified after Badarch et al., 2002).

In this doctoral thesis, newly identified occurrences of picritic (Le Bas, 2000; >12 MgO wt%) and andesitic greenstones within the Middle Paleozoic Tsetserleg accretionary terrane in central Mongolia are presented. In western Mongolia and adjacent areas, picritic and picrodoleritic magmatism formed in various geodynamic settings including accretionary-collision, intraplate including large igneous provinces (LIPs), island arc, and backarc-basin spreading during various periods ranging from Cambrian to Early Carboniferous have been studied (Oyunchimeg et al., 2009; Izokh et al., 2011; Shkol'nik et al., 2013). However, picrites (especially ferropicrites) have yet to be reported from the Hangay-Hentey belt. On the other hand, although andesites have been documented from accretionary complexes (e.g., the Zag-Haraa, Asralthairhan, and Onon) terranes within the Hangay-Hentey belt (Tomurtogoo, 2002, 2006, 2012; Badarch et al., 2002, 2003; Byamba et al., 2009), the high-Mg andesite (HMA) from the Hangay region was discovered for the first time and is reported in this study.

The main part of this thesis is published as Erdenesaihan et al., (2013). The basic characteristics of these particular important rocks are given in following sections. In this thesis, figures are set in the text, but tables are attached at the end of the text.

1.1.1 Ferropicrite

Ferropicrites are sub-alkaline or mildly alkaline primitive rocks that were first recognized by Hanski and Smolkin (1989) and Hanski (1992) in the Early Proterozoic Pechenga volcanic belt in the Kola Peninsula of the Baltic shield and in this study, the criterion for designating picritic rocks >14 wt% FeO* (Fe_2O_3*>15.5 wt%) is adopted. Since this time, not only Precambrian but also Phanerozoic ferropicrites have been recognized from some LIPs and greenstone belts (LIPs: e.g., Siberian Traps, Parana-Etendeka, and greenstone belt of Mino-Tamba, SW Japan) as relatively less amount of lava flows or dikes (Arndt et al., 1998; Gibson et al., 2000; Gibson, 2002; Ichiyama et al., 2006, 2007, 2008). The ferropicrites have long been misidentified as enriched-komatiites or Al-depleted komatiites. Besides significantly higher FeO* contents (Fig 1.1), they differ from komatiites in that they have enriched in Ti (1-2 wt% TiO_2), incompatible trace elements and significantly lower Al_2O_3 contents (generally <10 wt%). These geochemical differences require a different petrogenesis for ferropicrites. Various petrogenetic models have been proposed for the origin of ferropicrites with mantle heterogeneities, i.e., streaks of Fe-rich peridotite (Hanski and Smolkin, 1995; Gibson et al., 2000; Goldstein and Francis, 2008) or recycled oceanic crust (Gibson et al., 2002; Ichiyama et al., 2006).

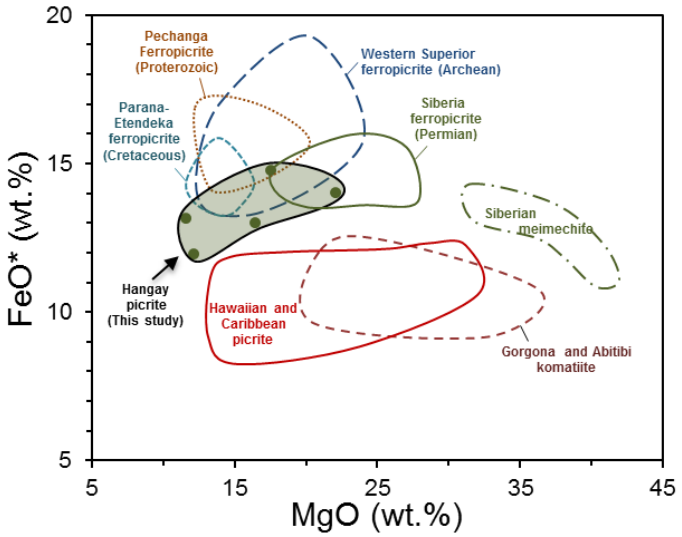

Figure 1.2 Variations of FeO (total Fe) and MgO for Archean to Recent high-Mg rocks. Data sources from: Hawaii (Norman and Garcia, 1999), Caribbean (Revillion et al., 1999), Parana-Etendeka (Gibson et al., 2000), Siberia (Arndt et al., 1995), Pechenga (Hanski and Smolkin, 1989; Hanski, 1992), Western Superior Province (Goldstein and Francis, 2008), Gorgona (Kamnetsky et al., 2010). Abitibi (Stone and Stone, 2000).*

1.1.2 High-Mg andesite (HMA)

The HMA are peculiar island arc volcanic rocks that are currently thought to form by reaction between the sub-arc mantle wedge and SiO_2-rich partial melt from subducted sediments or adakitic melt from hot subducted crust (Tatsumi and Ishizaka 1982; Li et al., 2013). Compositionally, the HMAs are generally classified into four types as sanukitic HMA (Setouchi volcanic belt in SW Japan), adalkitic HMA (Adac Island in the Aleutian arc), bajaitic HMA (Baja California Peninsula), and boninitic HMA (Bonin Island, Western Pacific) (Kamei et al., 2004). The adakitic and bajaitic HMA show high Sr/Y, and TiO_2 compared with the boninitic HMA, whereas the sanukitic HMA have TiO_2 and lower Sr/Y ratios (Fig.1.3). The boninitic HMA are very low in TiO_2 and Y relative to other HMAs. Discrimination diagrams on the basis of above chemical features of HMAs show that the Hangay high-Mg andesites are can be classified into the sanukitic HMA.

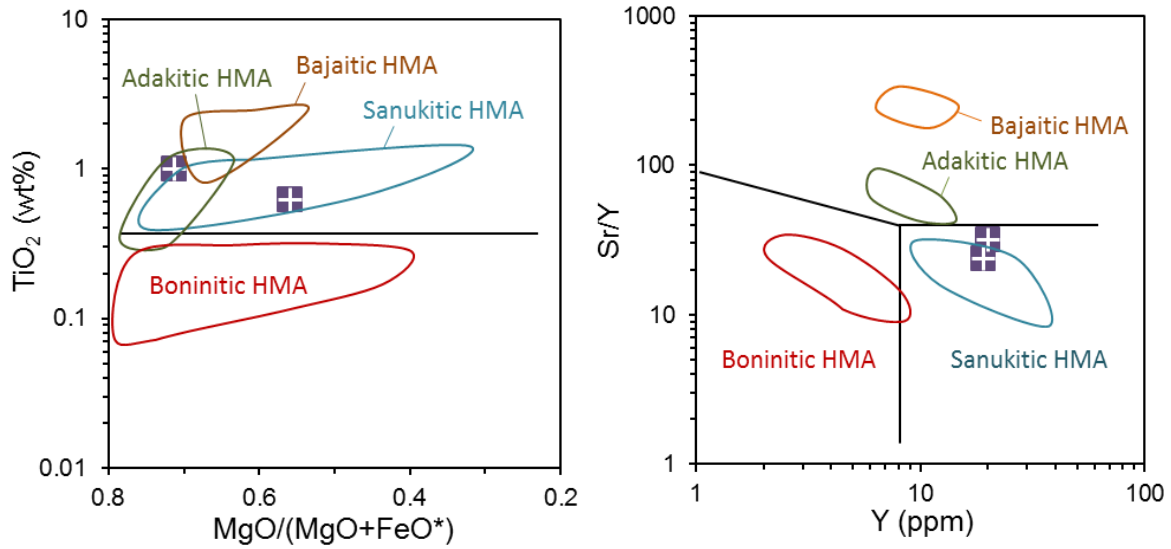

Figure 1.3 Discrimination diagrams for high-Mg andesites (after Kamei et al., 2004). Trace element compositions of the Hangay high-Mg andesites (this study) plotted in the field of the sanukitic HMA. Data sources are from Ishiwatari et al., 2006; Li et al., 2013; Rogers et al., 1985; Rogers and Saunders, 1989; Tatsumi et al., 2003, 2006; Yogodzinski et al., 1995.

1.2 Objective of this study

The main emphasis in this study was on newly discovered picrite (ferropicrite) and high-Mg andesites from the lower portion of much thick Erdenetsogt Formation in the Tsetserleg terrane of the Hangay-Hentey belt. The goals of this research was to clarify the petrogenesis of these greenstones, and examine the Middle Paleozoic oceanic magmatism and subduction-accretionary history related to the crustal growth processes of the Central Asian Orogenic Belt by presenting new field geological, petrological, and geochemical data and comparison with volcanic rocks from presently well-established geologic settings.

1.3 Material and method

Nineteen samples selected for the geochemical study based on their relative freshness under microscopic observation. The samples were analyzed for their mineral chemical, major, and trace element compositions and the results are listed in Tables 1-6.

Whole rock major element (Si, Ti, Al, Fe, Mn, Mg, Ca, Na, K, and P) and nine trace element (V, Cr, Ni, Rb, Sr, Ba, Y, Zr, and Nb) compositions were analyzed by X-ray fluorescence spectroscopy (RIX2100, Rigaku Corp.) at the Graduate School of Science, Tohoku University, using the glass bead method. After grinding and drying at 105°C, 1g of rock powder was mixed with 5 g of lithium tetraborate flux and fused at 1150°C. The resultant glass bead was irradiated using X-rays from a Rh tube. The accelerating voltage and current were 50 kV and 50mA, respectively. Quantitative analyses of major and trace elements were performed using calibration curves determined by measurement of standards from the GSJ Igneous Rock Series.

Major element compositions of igneous minerals were determined by energy-dispersive X-ray spectrometer (JEOL JSM-5410) at the Graduate School of Science, Tohoku University. The analyses were performed under an accelerating voltage of 15kV and a beam current of 1 nA on Co standard.

The REE and trace element concentrations of whole rock (embedded fragments of whole rock glass beads in thin section) and clinopyroxene were determined by laser ablation (193 nm ArF excimer: MicroLas GeoLas Q-plus)-inductively coupled plasma mass spectrometry (Agilent 7500S) (LA–ICP–MS) at the Incubation Business Laboratory Center of Kanazawa University. The analytical details and quality of data are decribed in Morishita et al. (2005). Each analysis was performed by

ablating 50-60 μm diameter spots at 5 Hz with an energy density of 8 J/cm2 per pulse. Signal integration times were 50 s for the gas background and the ablation intervals. NIST SRM 612 glass was used as the primary calibration standard and was analyzed at the beginning of each batch of <3–4 unknowns, with a linear drift correction applied between each calibration. The element concentrations of NIST SRM 612 were selected from the preferred values of Pearce et al. (1997). Data reduction was facilitated using Si as an internal standard for clinopyroxene, based on SiO_2 content obtained by EPMA analysis, following a protocol essentially identical to that outlined by Longerich et al., (1996). The accuracy of measurements estimated from analyses of the reference material (NIST SRM 614), was better than 4% in relative standard deviation for all elements.

CHAPTER 2 GEOLOGY AND TECTONICS OF THE HANGAY-HENTEY BELT

2.1 Review of geology and tectonics of the Hangay-Hentey belt

Traditionally, the territory of Mongolia has been divided broadly into northern and southern orogenic domains, each with a distinct crustal structure (Badarch et al., 2002). The northern domain consists dominantly of Precambrian to Middle Paleozoic rocks and may belong to the southern counterpart of the Siberian Craton, whilst the southern domain is dominated by Early to Late Paleozoic rocks and may belong to the northern counterpart of the Tarim and Sino-Korean (or North-China) Cratons. These domains are separated by the Main Mongolian Lineament (Fig. 1.1). The Hangay-Hentey belt occupies the southeastern margin of the northern domain. The tectonic nature of this belt has been a subject of discussion since the first plate tectonic synthesis of Mongolia by Zonenshain, (1973), who was interpreted the Hangay-Hentey belt as “miogeosyncline basin” filled with much thick Paleozoic turbidites and underlying by continental crust. Until recent, the similar interpretations (turbidite terranes) has been shared by Kovalenko et al. (1996, 2004), Buchan et al. (2001), Badarch et al. (2002, 2003), and Jahn, (2004), viewing it as a continental block (“hidden” Archean-Neoproterozoic basement) overlain by a thick sedimentary cover. Beside this idea, the first idea that explaining its origin related to the subduction-accretionary process was suggested by Şengör et al., (1993), and Şengör and Natal’in, (1996), taking into consideration the presence of pelagic chert lenses in turbidites and complicated deformation of the belt. They envisaged that the Hangay-Hentey belt has been formed by development of the Hangay-Hentey Ocean between the Siberian Craton and the Tarim and Sino-Korean Cratons from Vendian-Cambrian to Permian period. Presently, the latter hypothesis is widely accepted and evidenced by recent comprehensive sedimentological, biostratigraphical, and geochemical studies conducted on rocks of oceanic plate stratigraphy, which occur as thrust slices (Tomurtogoo, 2002, 2006, 2012; Kurihara et al., 2006, 2009, Tsukada et al., 2006, 2013; Kelty et al., 2008; Safonova et al., 2009; Bussien et al., 2011; Purevjav and Roser, 2012, 2013), and the hypothesis is partly demonstrated in the new tectonostratigraphic subdivision map of Mongolia (Tomurtogoo, 2012). The opening time of the Hangay-Hentey ocean or Mongol-Okhotsk ocean has been variably interpreted in the literatures: Vendian (Şengör et al., 1993; Şengör and Natal’in, 1996;

Tomurtogoo et al., 2005), Silurian (Zorin, 1999; Badarch et al., 2002; Windley et al., 2007; Bussein et al., 2011), or Permian (Zonenshain et al., 1990). Although the most recent studies show that both Vendian and Silurian times are acceptable (Wilhem et al., 2012, references therein). However, the closure process and tectonic setting of the Hangay- Hentey paleo-ocean are still debated. The paleo-ocean existed between ancient cratons has been assigned various names, such as the Paleo-Asian, Paleo-Pacific, Khangai-Khantey, Hangay-Hentey, and Mongol-Okhotsk paleo-ocean. In this research, I use the term “Hangay-Hentey paleo-ocean” to present the western extension of the Mongol-Okhotsk paleo-ocean. Published paleolatitudinal data and reconstruction indicate that the Central Mongolian (or Tuva-Mongolian microcontinent) Massif, beneath which the Hangay-Hentey oceanic plate subducted, was already adjacent to the Siberian craton in the Vendian (Late Proterozoic) and Early Cambrian time (Kravchinsky et al., 2001).

2.2 Geology of the Uyanga area

Figure 2.1a shows the terrane subdivision of the Hangay-Hentey belt proposed by Tomurtogoo (2012). As demonstrated by Byamba et al. (2009), the ages of accretionary complexes within the Hangay-Hentey belt young progressively eastward from Ordovician-Late Silurian through Devonian-Carboniferous to Permian-Triassic. The Devonian–Carboniferous turbidite sequences within this belt are notable for their great thickness (reaching 10,000 m in the Hangay region; Amantov et al., 1970). These sequences were derived from the Neoproterozoic–Early Palaeozoic basement, its cover, and overlying arc volcanoes, based on detrital-zircon age and provenance analysis (Filippova, 1969; Kelty et al., 2008; Bussien et al., 2011; Purevjav and Roser, 2012, 2013).

The Tsetserleg terrane in the western part of the Hangay- Hentey belt consists of the Lower to Middle Devonian Erdenetsogt, Middle to Late Devonian Tsetserleg, Lower Carboniferous Jargalant, and Permian Baidrag formations. The Erdenetsogt Formation with an area of 10,000 km^2 is distributed widely in the Hangay region and composed predominantly of unmetamorphosed, gently folded, turbidite-dominated sediments. According to Lhundev et al. (1994), the formation is further divided into two subunits with conformable contact: (1) a lower volcanic-sedimentary sequence including chiefly bluish-gray and greenish-gray tuffaceous-siltstones, medium- to fine-grained sandstones, and variously colored and bedded radiolarian ribbon-chert intercalated with basaltic greenstones (thickness of ~830 m) and (2) an upper sedimentary subunit consisting dominantly of

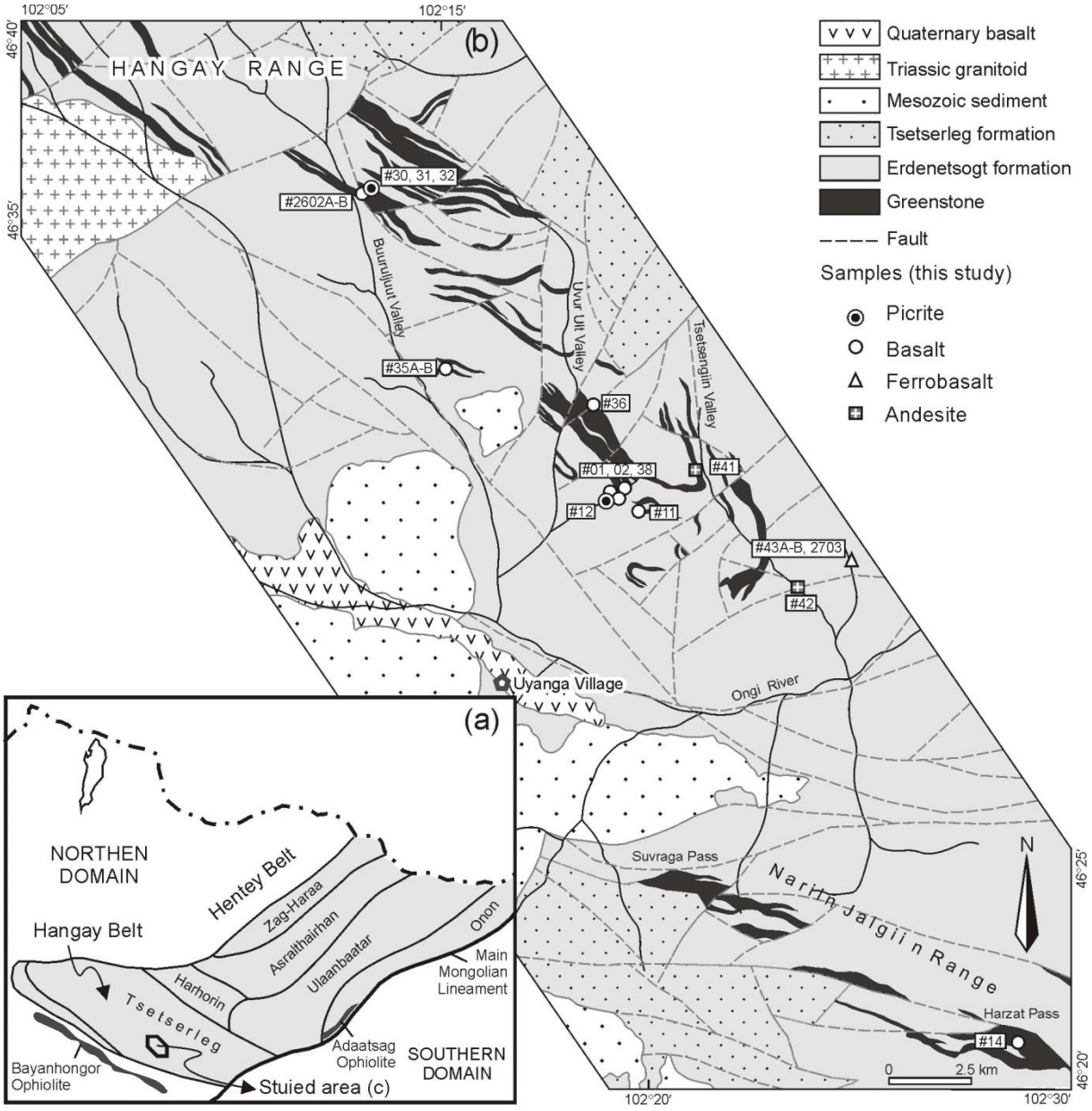

Figure 2.1 (a) Insert map shows terrane subdivision of the Hangay-Hentey belt by Tomurtogoo (2012) and location of study area. (b) Simplified geological map of the Uyanga area, south Hangay region (modified after Geological Map L-48-49-A, B, D, 1:50 000, Lhundev et al., 1994).

blackish-gray and bluish-gray sandstone and siltstones with minor layers of cherts and limestones (thickness of ~1100 m). These are overlain by the Middle to Late Devonian Tsetserleg Formation, which is dominated by terrigenous-sediments (Fig.2.1). Teraoka et al. (1996) described some large olistolith containing manganiferous chert and schistose green sandstone in the lower subunit. The age of the Erdenetsogt Formation determined by fossils in the sedimentary sequences intercalated with

the greenstones as well as intrusive rocks cut it ranges from Early to Late Devonian. For example, Bayarsaihan et al. (1988) found coral and brachiopods, and assigned these to the Lower to Middle Devonian. Kurimoto et al. (1997) reported Late Devonian (Famennian) conodonts from the bedded red chert. Siliceous tuff in the lower subunit yielded an age of 400 Ma by Sm-Nd dating (Orolmaa and Erdenesaihan, 2008). The basement of the Erdenetsogt Formation is uncertain. Late Permian to Early Triassic undeformed granitoids interpreted as subduction-collisional (Orolmaa et al., 2008, 2010), are widely intruded into the study area. Geochemical studies have revealed that the granitoids in the Hangay region were derived mainly from partial melting of juvenile materials with some involvement of Precambrian basement (Kovalenko et al., 1996, 2004; Jahn et al., 2000, Jahn, 2004). For this reason, several researchers (Buchan et al., 2001; Badarch et al., 2002) have argued that the thick Devonian-Carboniferous Hangay-Hentey turbidite sediments are underlain by a 'hidden' Precambrian terrane. These pre-Permian accretionary complexes are overlain unconformably by Permian shallow marine molasses (Badarch et al., 2003). Quaternary continental volcanic rocks also occur in this region as well.

The possible eastern extension of the Erdenetsogt Formation as has been suggested by many researchers (Dorjsuren, 2006; Tomurtogoo, 2006, 2012; Byamba et al., 2009) in the Hentey area is called the Gorkhi Formation in the Ulaanbaatar terrane, which includes similar oceanic plate assemblages of Late Silurian to Late Devonian age as constrained by microfossils in chert (Kurihara et al., 2009). The associated basaltic greenstone in this formation was studied by Tsukada et al. (2006, 2013) and Safonova et al. (2009). They suggest that alkali basalts with typical oceanic island basalt (OIB) affinity formed as an oceanic island or seamount in an intra-plate oceanic setting of the Paleo-Asian or Paleo-Pacific paleo-ocean that existed between the Angara (Siberia) craton and North China (Sino-Korean) blocks.

CHAPTER 3 FIELD OCCURRENCE AND PETROGRAPHY

The area investigated is located in the Uyanga Village of the Ovurhangay Province, 470 km southwest of the Ulaanbaatar City. The basaltic greenstones are exposed mainly along the Uvur-Ult and Buuruljuut Valleys (gold mining sites) to the northeast of the Uyanga Village and in the Nariin Jalgiin Range to the southeast (Fig.2.1). Sample localities are listed in Table 1.

3.1 Field occurrence

The lower part of the Erdenetsogt Formation is characterized by basalt-chert sequences. Although a massive limestone cap is absent, a minor amount of limestone was reported by a previous study (Lhundev et al., 1994). The greenstones occur as massive lavas, porphyritic and aphyric dikes (up to 5 m thick and 400 m long), hyaloclastite, and mafic tuffs and sills. In several localities, a conformable relationship between cherts and lavas were observed (#35, #02 and #43 in Fig.2.1b). For example, in the Uvur-Ult Valley, the varicolored, massive or bedded ribbon cherts attain a thickness of 40 m and are always intercalated with greenstones (Figs. 3.2). In the Tsetsengiin Valley, the chert-basalt sequences are folded concordantly and tightly and occurr as composite boudins roughly 10 m in size in the siltstone matrix (Fig. 3.1c). The basaltic greenstones are divided easily in the field into ferrobasalt and normal basalt by using a magnetometer. The ferrobasalts contain abundant magnetite and have very high magnetic susceptibility, ranging from 16 to 36×10^{-3}SI, whereas the normal basalts in the field area have values of 1-0.3×10-3SI. I found, for the first time in this area, picrites at two localities (Figs. 2.2 and 3.1). The picrites found in the Buuruljuut Valley (46°35’43.1”N, 102°13’27.1”E) occur as olivine-rich zones with thickness of 20-40 cm at the base of massive basaltic lavas outcropping with shear contact and sometimes showing gradation in olivine concentration, whereas the picrite found in the Uvur-Ult Valley occur as cobbles in a river bed. Another new discovery from this area is high-magnesian andesite sills (N50°W; 30°SW) that intrude into siltstone along the west side of the Tsetsengiin Valley (46°31’13.9”N, 102°21’13.3”E). I observed three parallel andesite sills up to 1.7 m thick with a distinct pinkish-green color, which contrasts with the dark-green color of the other greenstones (Fig. 3.1d).

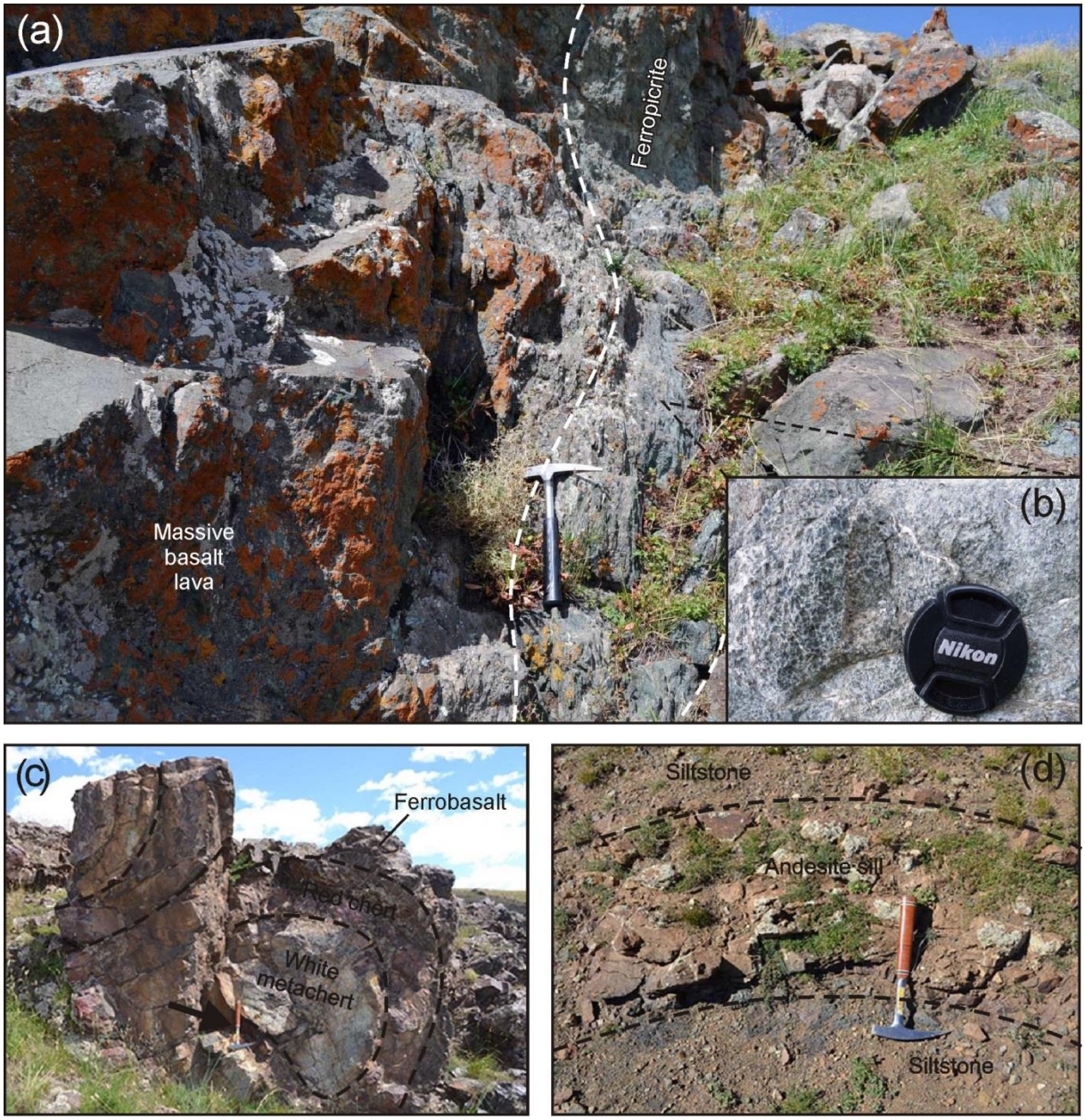

Figure 3.1 Field photographs of the Hangay greenstones and their associated cherts. (a-b) Ferropicrite at the Buuruljuut area. (c) Folded chert and ferrobasalt at the Tsetsengiin gol area. (d) Andesite sill intruded into siltstone at the Tsetsengiin gol area.

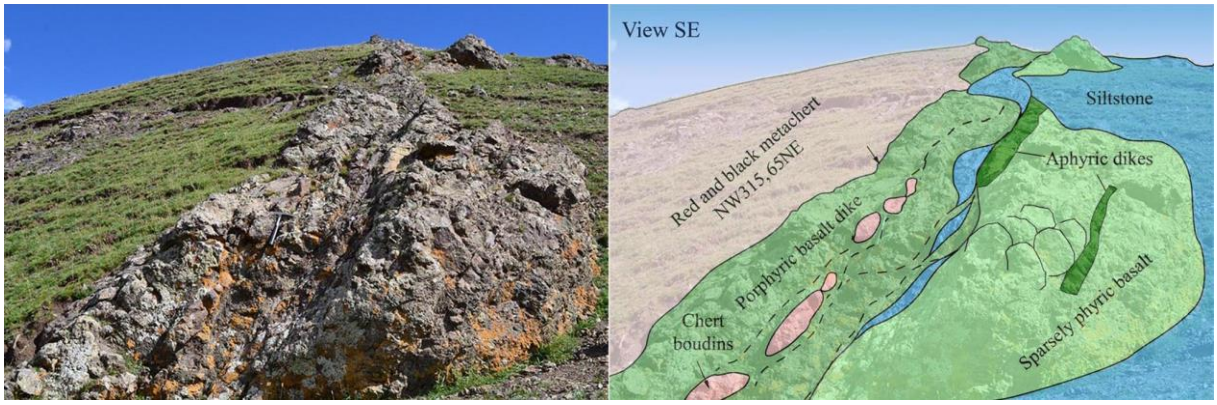

Figure 3.2 Field photography of the outcrop at the Uvur-Ult area: (a) Outcrop of a chert-greenstone complex viewed from NW to SE. (b) Interpretation of (a), showing intercalation of basaltic dikes and cherts.

3.2 Petrography

Petrographical observations were made on 37 thin sections (Table 1). Representative analysis of the minerals are shown in Tables 3-6. Porphyritic basaltic rocks were named according to major phenocryst phases, but only where the total abundance of phenocrysts was >1 vol.% (e.g. plagioclase-phyric basalt or olivine-clinopyroxene-phyric basalt). Phenocryst phases were always listed in order of decreasing abundance so that the dominant phase was listed first. The term phenocryst was used for any crystal that was significantly (typically five times) larger than the average size of the groundmass crystals, larger than 0.5 mm (MacKenzie et al., 1982), and euhedral or subhedral in shape. The prefix micro- was added to the phenocrysts which have diameters between 0.05 and 0.5 mm (e,g. clinopyroxene microphenocrysts) (MacKenzie et al., 1982), and larger than the modal groundmass grain size.

3.2.1 Picrite (#12)

The picritic greenstones including ferropicrites are highly olivine-phyric (up to 32 vol.%) with clinopyroxene phenocrysts (up to 5 vol.%, but preserved in only sample #12). Intergranular and partly intersertal texture. The olivines are subhedral to anhedral and have an average size of 4 mm. They are completely replaced (and therefore could not be analyzed) by secondary chlorite, talc, calcite, and quartz and always contain fresh spinel crystals as inclusion (Fig.3.3). Scattered large euhedral spinel grains (up to 1.5 mm) also occur. The clinopyroxenes are mostly subhedral to anhedral (up to 2 mm)

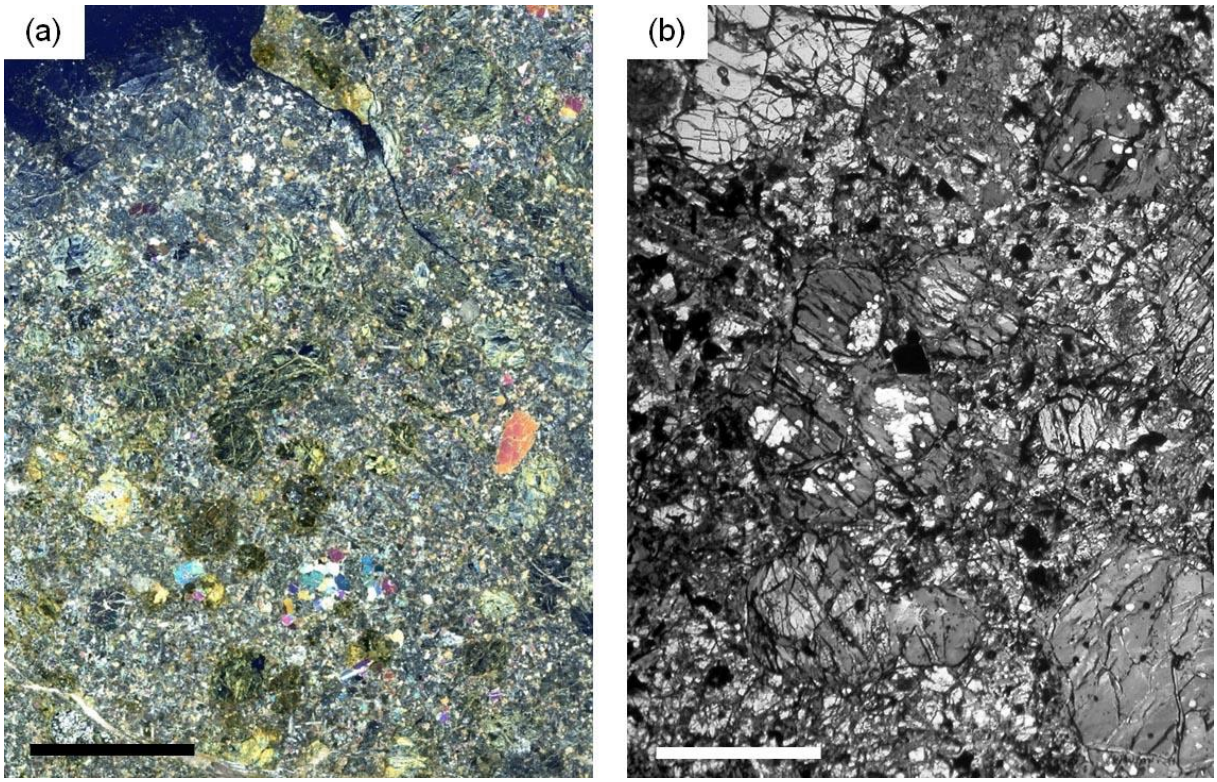

Figure 3.3 Thin section photomicrographs of picrite (#12) under cross-polarized light. (a) Highly olivine-phyric picrite showing subhedral to anhedral phenocrysts of olivine (now replaced by chlorite) and clinopyroxene (well-preserved) set in groundmass of albitized plagioclase laths and fine grained clinopyroxene aggregates. Width of scale is 5 mm. (b) Euhedral well-preserved spinel inclusions (isotropic) in completely altered olivine phenocrysts. Width of scale is 1 mm.

and sometimes form glomerocrysts of microphenocrysts. Groundmass is hypocrystalline and composed of well-preserved anhedral aggregates of clinopyroxenes (14 vol.%) and plagioclase laths (50 vol%, replaced by albite, chlorite, sericite, and epidote) and chloritized volcanic glass. Accessory phases (<2 vol.%), in order of abundance, are fine-grained Ti-Fe oxides and ilmenite needles and titanites. The rock shows no resorbed crystals indicating disequilibrium of crystal growth.

3.2.2 Sparsely clinopyroxene-plagioclase-olivine-phyric basalt (#01)

This is the most dominant type of basalt in the study area. The basalt composed of plagioclase (5 vol.%), clinopyroxene (1 vol.%), and olivine (0.5 vol.%) phenocrysts and show intergranular texture (Fig.3.4). The glomerophenocrysts of plagioclase and equant clinopyroxenes occur. Euhedral olivines ranging in size from 0.5 to 1.2 mm and are completely replased by quartz, calcite, and chlorites.

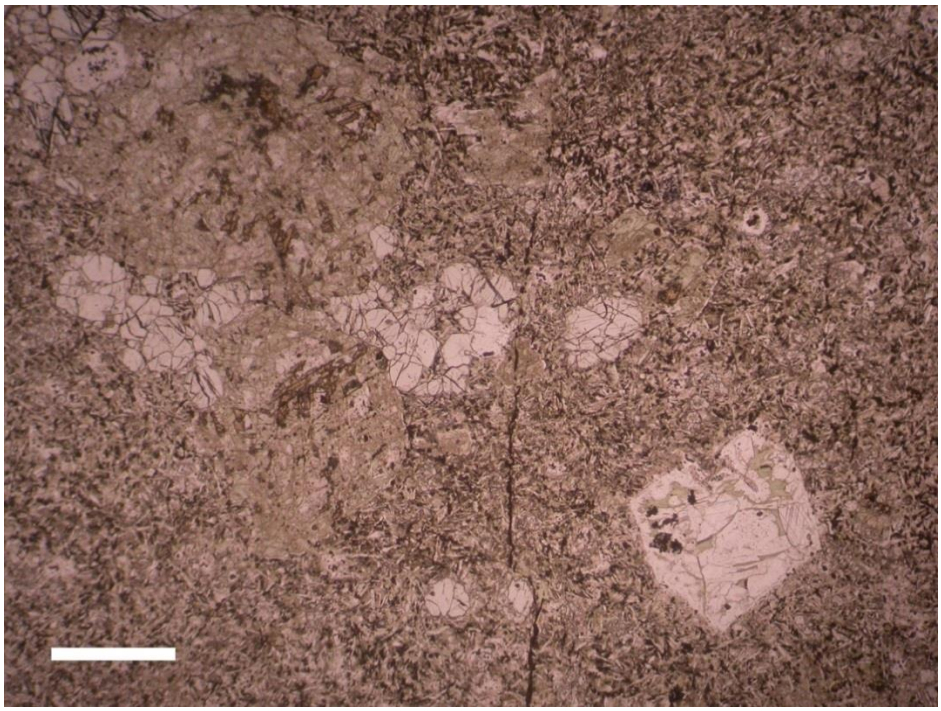

Figure 3.4 *Thin section photomicrograph of sparsely phyric basalt (#01) under plane-polarized light. Completely altered euhedral olivine phenocryst (replaced by calcite and chlorite), plagioclase and well-preserved subhedral clinopyroxenes set in the fine grained groundmass. Width of scale is 1 mm.*

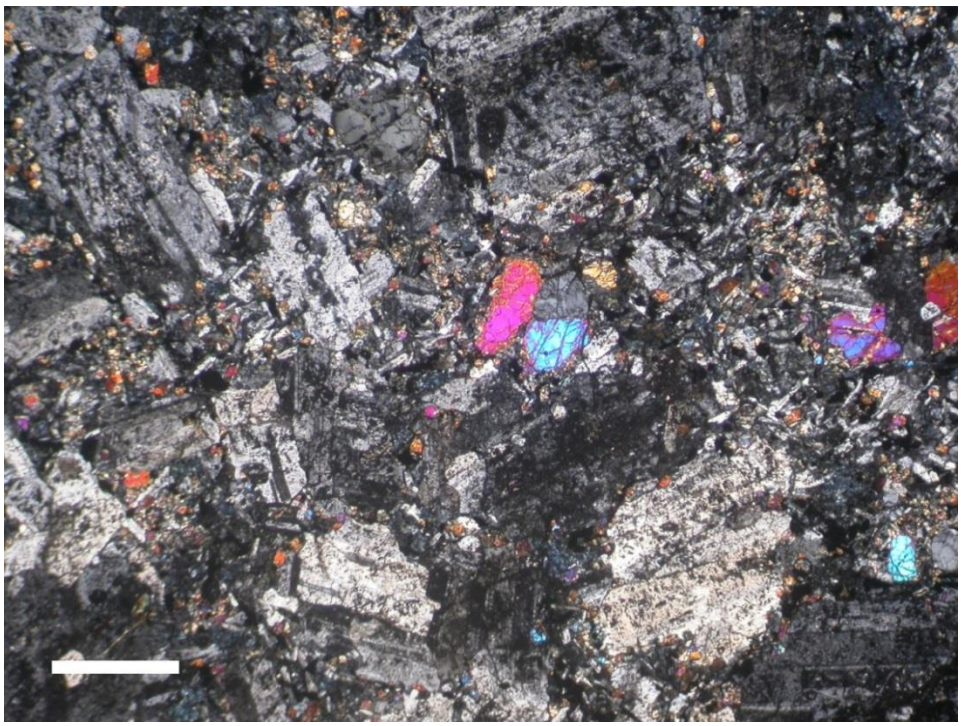

Figure 3.5 *Thin section photomicrograph showing the porphyric doleritic basalt dyke (#11) under cross-polarized light. Width of scale is 1mm.*

in size). The plagioclases are albitized and saussuritized in all cases and some of them show polysynthetic twining (up to 2.5 mm in size). The groundmass is hypocrystalline and composed of euhedral plagioclase laths and anhedral fine-grained clinopyroxene aggregates, interstitial chloritized volcanic glass and opaque minerals. Titanite is the most dominant opaque mineral (up to 1 vol.%). Absence of olivine in the groundmass donates the tholeiitic affinity.

3.2.3 Porphyric dolerite dyke (#11)

The rock mainly consists of megaphenocrysts of plagioclase (50 vol.%) and occasional clinopyroxene phenocrysts (1 vol.%) (Fig.3.5). The plagioclase phenocrysts with an average size of 25 mm, and highly albitized and polysynthetic twinning is well preserved. The clinopyroxenes (1.1 mm in size) occur as subhedral phenocrysts and well preserved. The groundmass is coarse-grained holocrystalline and consists of fine-grained anhedral aggregates of clinopyroxenes and plagioclase laths. Fe-Ti oxide and titanite also occur as accessory phases (<1 vol.%).

3.2.4 Sparsely plagioclase-clinopyroxene-microphyric dolerite (#02)

The rock contains contains occasional phenocryststs (up to 1 mm in size) and mostly microphenocrysts of plagioclase and clinopyroxenes set in Intergranular textured groundmass. Plagioclase is replaced by albite in all cases. Subhedral to anhedral microphenocrysts of

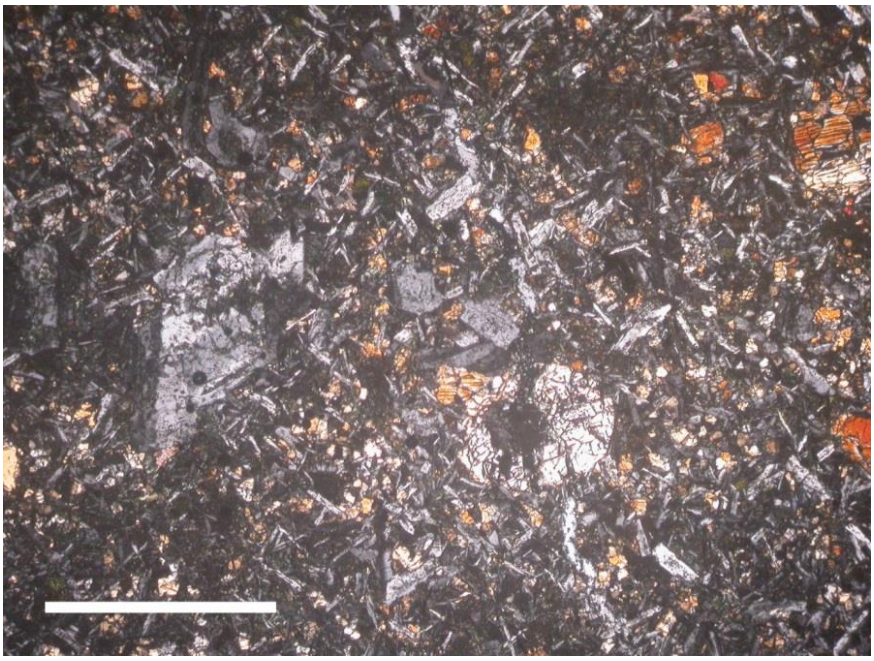

Figure 3.6 Thin section photomicrograph of dolerite (#02) under cross-polarized light. Width of scale is 1mm.

clinopyroxenes are well-preserved. Groundmass is holocrystalline and composed of plagioclase laths as well as microlits, anhedral clinopyroxenes aggregates (7 vol.%), opaque minerals. Titanite and magnetite are the most common opaque minerals.

3.2.5 Vesicular sparsely plagioclase-phyric basalt (#36)

Phenocrysts of plagioclase (5 vol.%) are euhedral to subhedral, up to 1 mm in size and sometimes occur as glomerocrysts. Occasional subhedral microphenocrysts (up to 0.6 mm in size) of clinopyroxenes (0.5 vol.%) occur. Groundmass in this rock is hypocrystalline comprising lath to microlits of plagioclases (50 vol.%), clinopyroxene (5 vol.%), opaque minerals and interstitial chloritized glass. The rock sparsely vesicular having rounded to anhedral-shaped vesicles ranges from 0.5 to 2.5 mm in diameter and mostly filled by calcite and rarely chlorite and abundance is ~7 vol.%. The most abundant opaque minerals are magnetite (1 vol%) and blotch of sulfides are present (< 0.5 vol.%).

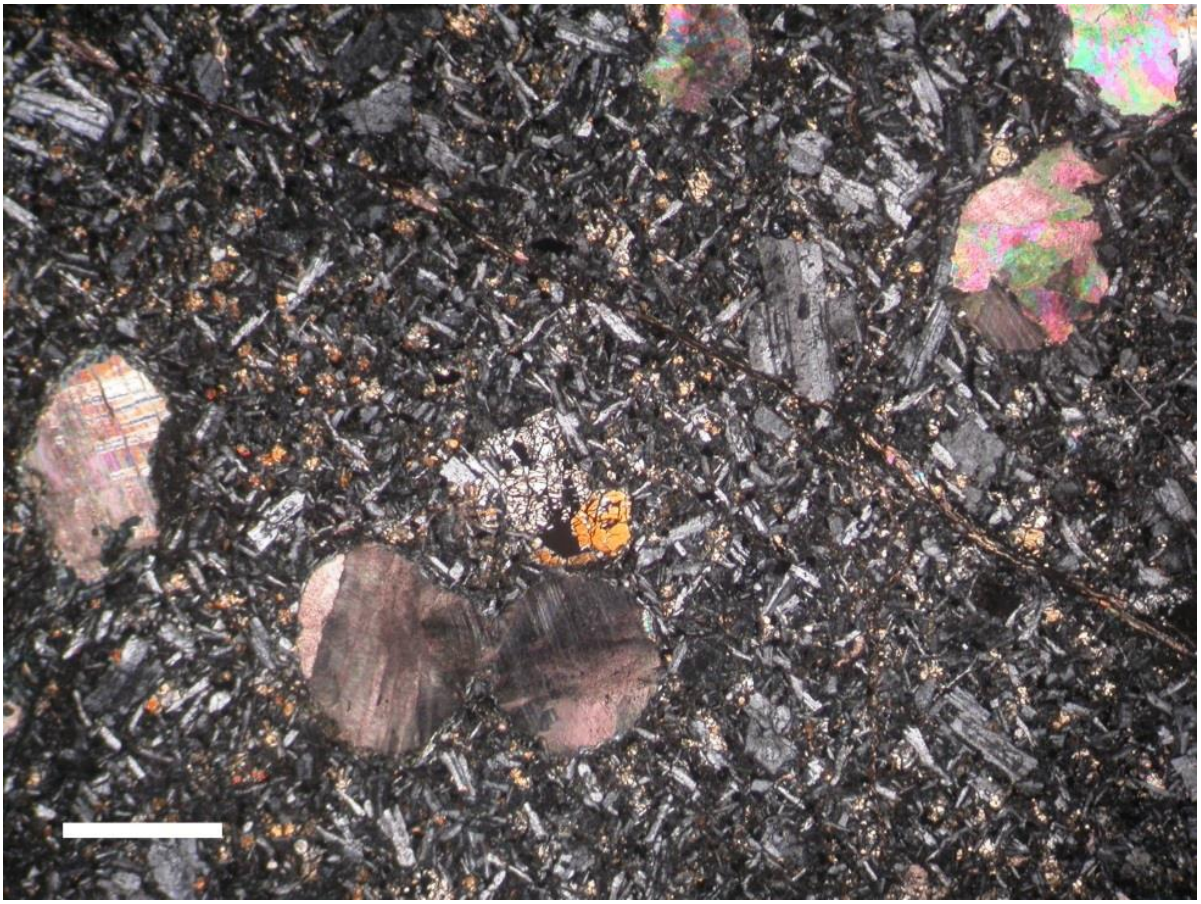

Figure 3.7 Thin section photomicrograph of vesicular basalt (#36) under cross-polarized light. The 1mm.

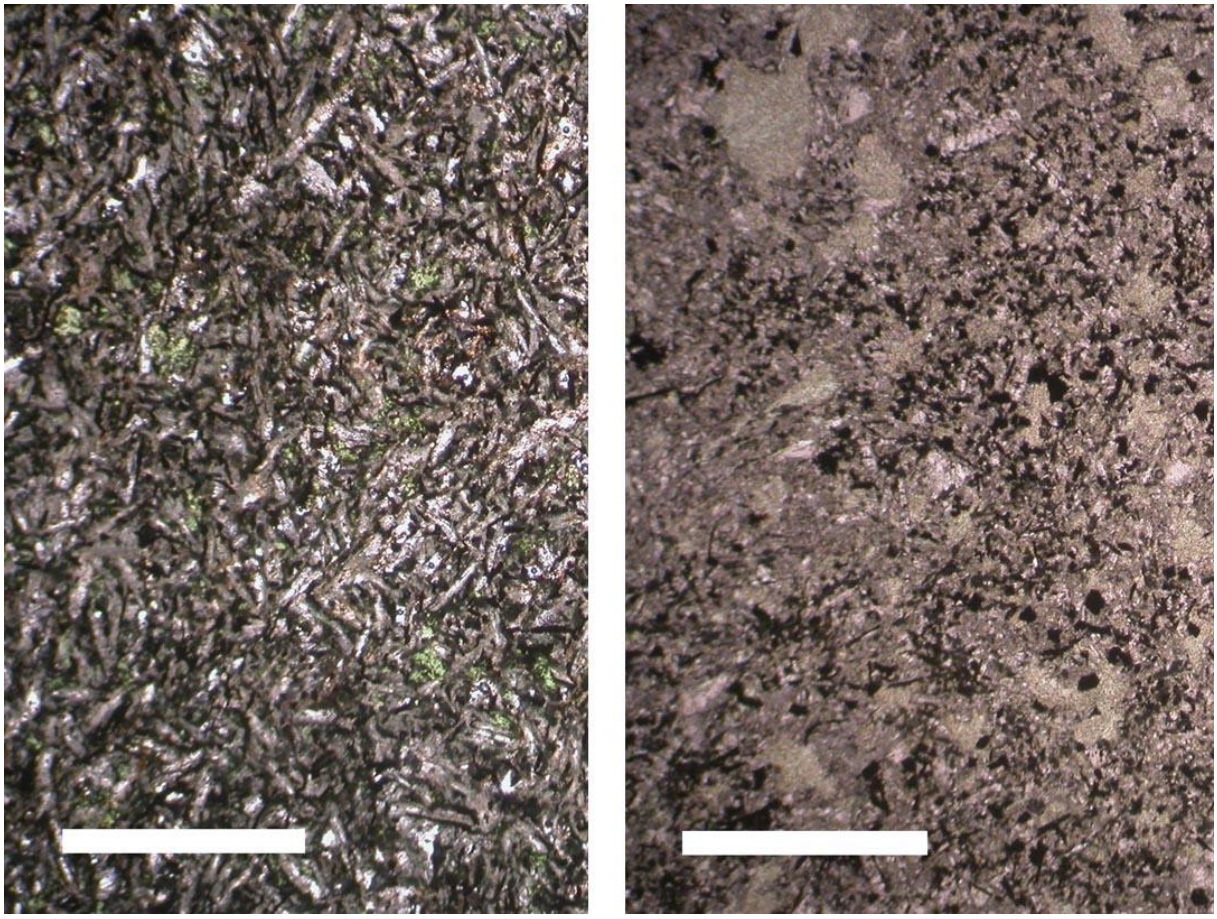

Figure 3.8 Thin section photomicrographs of aphyric basalts with abundant Fe-Ti oxides under plane-polarized light. (a) #35B showing trachitic texture. (b) vesicular #43A. Width of scale is 1 mm.

3.2.6 Aphyric basalt (#35B and 43A)

This aphyric basalt consists mainly of plagioclase laths, interstices of which are chlorite and smectite after volcanic glass. Sample #35B exhibits relatively coarser-grained and show trachytic textured groundmass and rich in ilmenite, identified by its elongated needles.

The sample #43A has aphanitic groundmass and sparsely vesicular (filled by calcite). Vesicles are anhedral, up to 0.4 mm in diameter. The magnetite is the dominant opaque mineral, identified by its euhedral cubic form. Rare elongate needles of ilmenite and blotch of sulphide also occur.

3.2.7 Porphyric basalt dyke (#38)

In hand specimen, plagioclases are can be identified (generally with an average size of 3 mm, and have 35 vol.%). The rock consists of euhedral megacrysts of plagioclase with melt inclusions (now altered) and clinopyroxene phenocrysts enclosed by aphanitic groundmass. Although the

plagioclases are highly saussuritized,

Figure 3.9 Thin section photomicrograph of highly porphyritic basalt dike (#38) under cross-polarized light. The rock shows large euhedral plagioclase phenocrysts and occasional clinopyroxene crystals set in aphanitic groundmass. The margin of dyke is characterized by a glassy margin. Width of scale is 5 mm.

the igneous strongly zoned texture is preserved. The clinopyroxene are euhedral, ranges in size from 0.5 to 2 mm, and are completely altered in this rock by chlorite. Note that the groundmass crystallinity becomes more glassy toward the rim of this dike, implying that the dike were intruded into the chert. There were no contact metamorphic effects on overlying chert (Fig. 3.2).

3.2.8 Andesites (#41 and #42).

The high-Mg andesite found in the Tsetsengiin Valley (Fig. 2.2) is relatively aphyric and contains less than 10 vol.% phenocrysts including completely altered anhedral olivine (2 vol.%, up to 1.2 mm in size). Well-preserved euhedral to subhedral microphenocrysts of clinopyroxene (4 vol.%, ranges in size from 0.1 to 0.5 mm in size), and brown and green amphiboles (0.5 vol.%) are present in an

aphanitic groundmass (Fig. 3.10). The amphiboles are identified as hornblende by electron microprobe analysis (Table 6). Notable relict igneous spinel inclusions were observed in both olivine and clinopyroxene microphenocrysts of this rock. No phenocrysts of plagioclase or bronzite has crystallized in the rock as do in boninites. An absence of plagioclase phenocryst and glassy nature are common feature of the sanukitic high-Mg andesites.

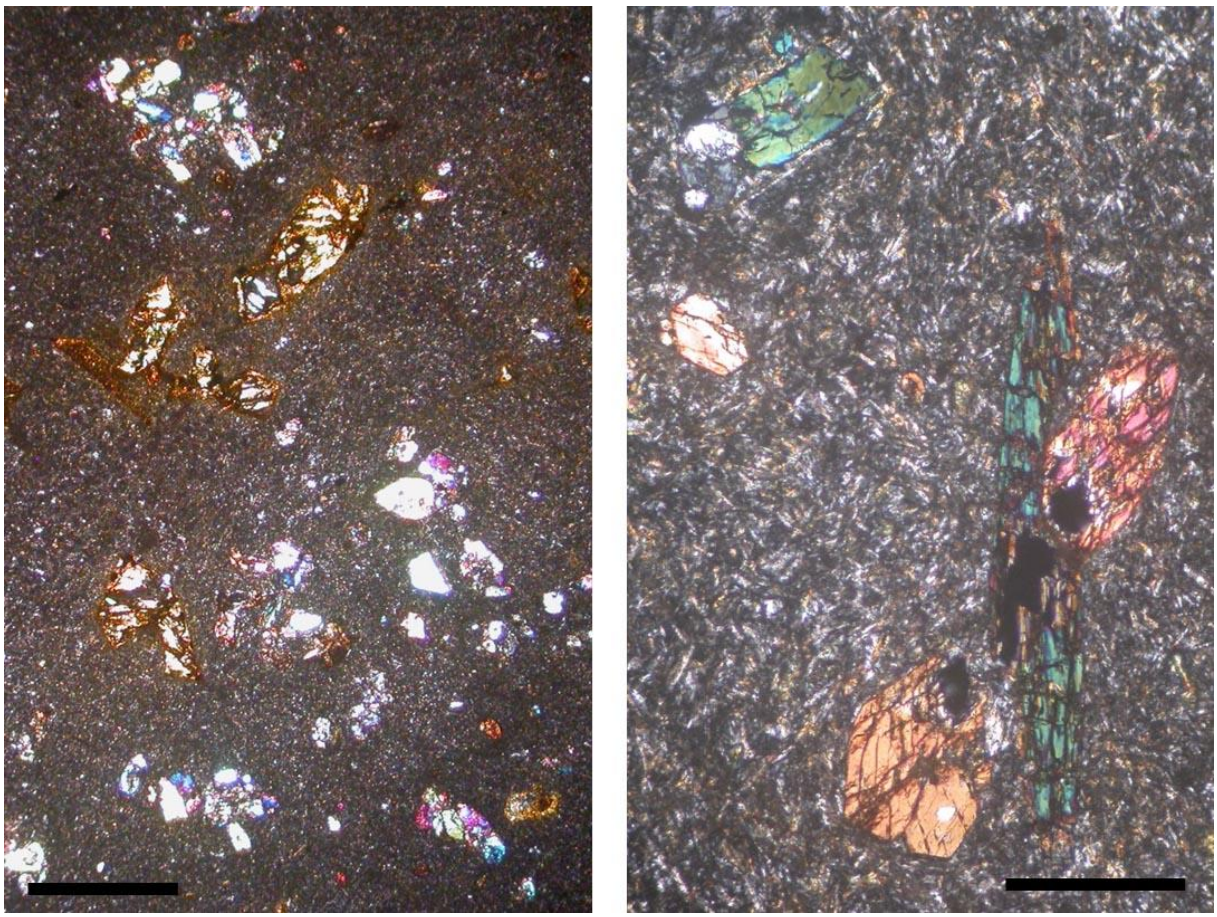

Figure 3.10 Thin section photomicrographs of the andesite under cross-polarized light. (a) Microphenocrysts of completely altered olivines and well-preserved clinopyroxene glomerocrysts set in aphanitc groundmass. Width of scale is 1 mm. (b) Microphenocrysts of euhedral hornblende in sample #41. Width of scale is 0.25 mm.

3.3 Alteration

As seen on above petrographical description, all of the studied moderately to highly altered Hangay greenstones are experienced by pumpellyite-actinolite facies low-temperature metamorphism, which is very common metamorphism at the upper extrusive oceanic crust. Chlorite, epidote, albite,

pumphellyite, actinolite, talc, calcite, quartz, and opaque minerals are common secondary minerals (Fig.3.11).

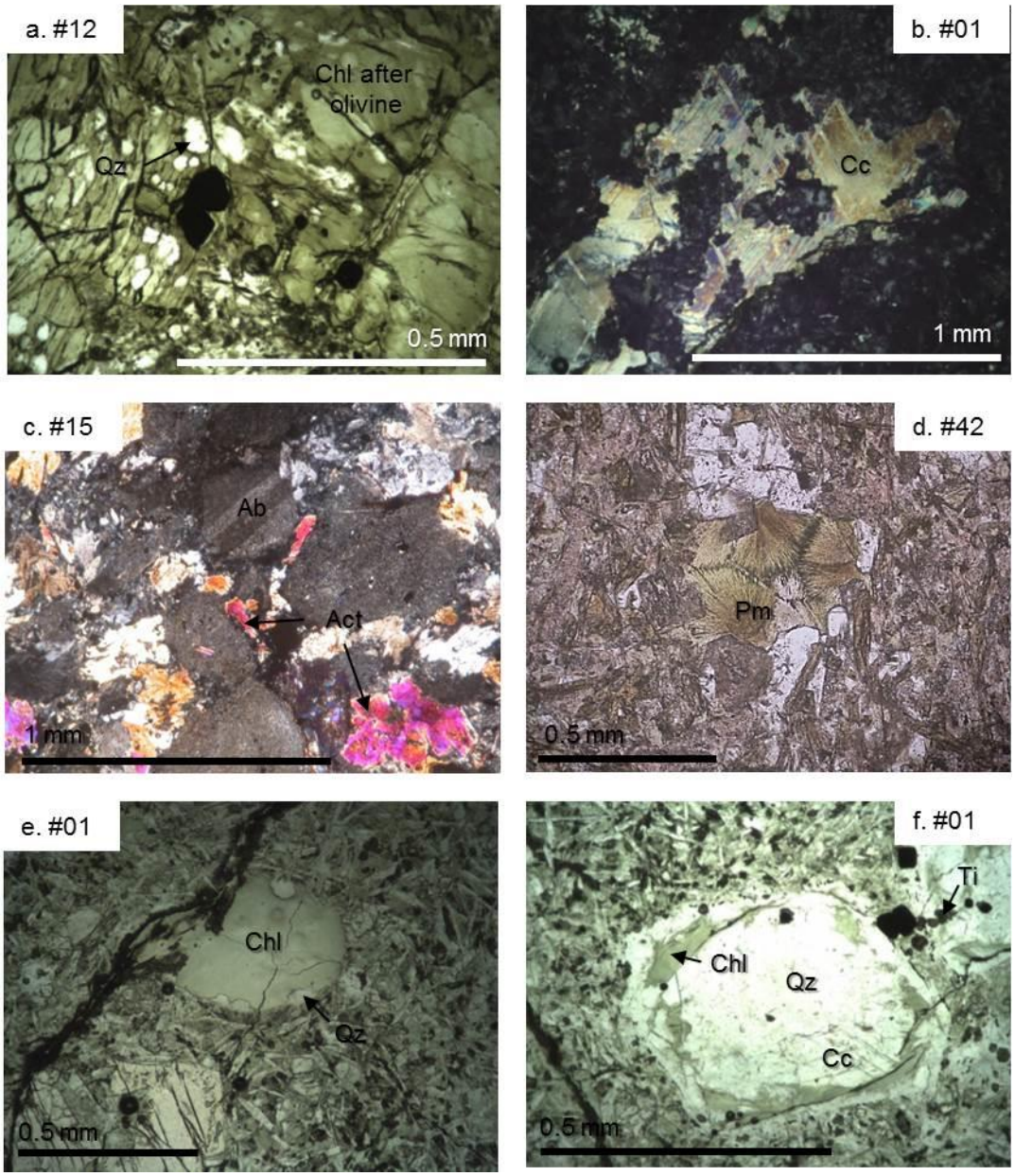

Figure 3.11 Thin section photomicrographs of alteration minerals in the Hangay greenstones under cross-polarized lights. Corresponding sample numbers are given.

CHAPTER 4 RESULTS

The greenstones in the Hangay area experienced low-temperature alteration and weathering. However, there is general agreement that the rare earth elements (REEs), high field strength elements (HFSEs), and some transition metals are relatively immobile under alteration (Winchester and Floyd, 1977; Ludden and Thompson, 1978; Condie, 2001). In this paper, I discuss the chemistry of the greenstones based on these least mobile elements of the whole rock chemical composition and on the mineral chemistry of well-preserved igneous clinopyroxenes and spinels.

4.1 Whole rock chemistry and classification

Whole rock major and trace element data for the Hangay greenstones are presented in Table 2. All major oxides were normalized to a 100% anhydrous basis before chemical interpretation. The Hangay greenstones have basaltic or andesitic compositions with silica contents ranging from 43.4-51.5 wt% and 53.4-58.2 wt%, respectively.

The Hangay greenstones can be divided broadly into three major geochemical types defined by their incompatible element distributions: (1) enriched plume-type with slight LREE enrichment similar to tholeiitic OIB (average $La/Yb_{PM}>3.8$; Hawaiian tholeiite ~3.0 and alkali basalt ~8.0; Best, 2003), (2) non-enriched plume-type approximately equal to E-MORB (average $La/Yb_{PM}<1.8$), and (3) arc-type with LREE enrichment, negative Nb and Ta anomalies, and $La/Yb_{PM}>9.3$. The first type is most abundant and consists of picrites (ferropicrite), basalt, dolerite and ferrobasalts. The latter two types are relatively less common in this area.

4.1.1 Picritic and basaltic greenstones

The picrites are characterized by their higher MgO (18-22 wt%) and lower Al_2O_3 (8.62-12.75 wt%) contents. Two of the five picrites sampled (>12 wt% MgO) from the Hangay region showed ferropicritic compositions, as defined by Hanski and Smolkin (1989) and Hanski (1992), with >14 wt% FeO*. The basalts, dolerites and ferrobasalts have lower MgO (4.4-8.9 wt%) and higher Al_2O_3 (13-20 wt%). However, the ferrobasalts are distinctly enriched in FeO* (14-17 wt%) and TiO_2 (3.9-5.4 wt%) (Table 2).

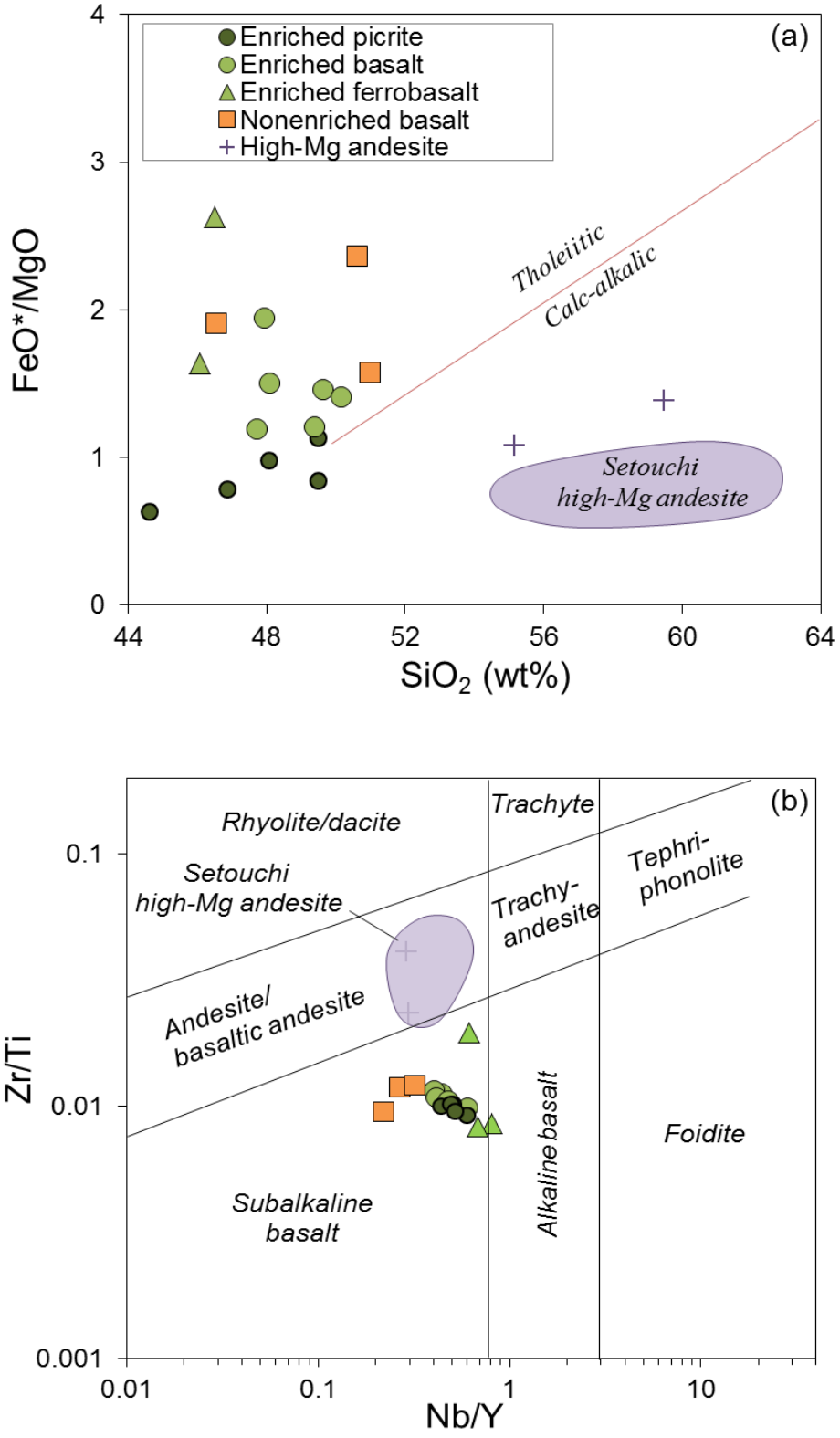

Figure 4.1 (a) FeO/MgO versus SiO_2 plot for the Hangay greenstones (after Miyashiro, 1974). The Shodo-Shima high-Mg andesite of the Setouchi volcanic belt, SW Japan (Tatsumi et al. 2006), is shown for comparison. (b) Zr/Ti-Nb/Y plot after Pearce (1996). Ti is recalculated from TiO_2.*

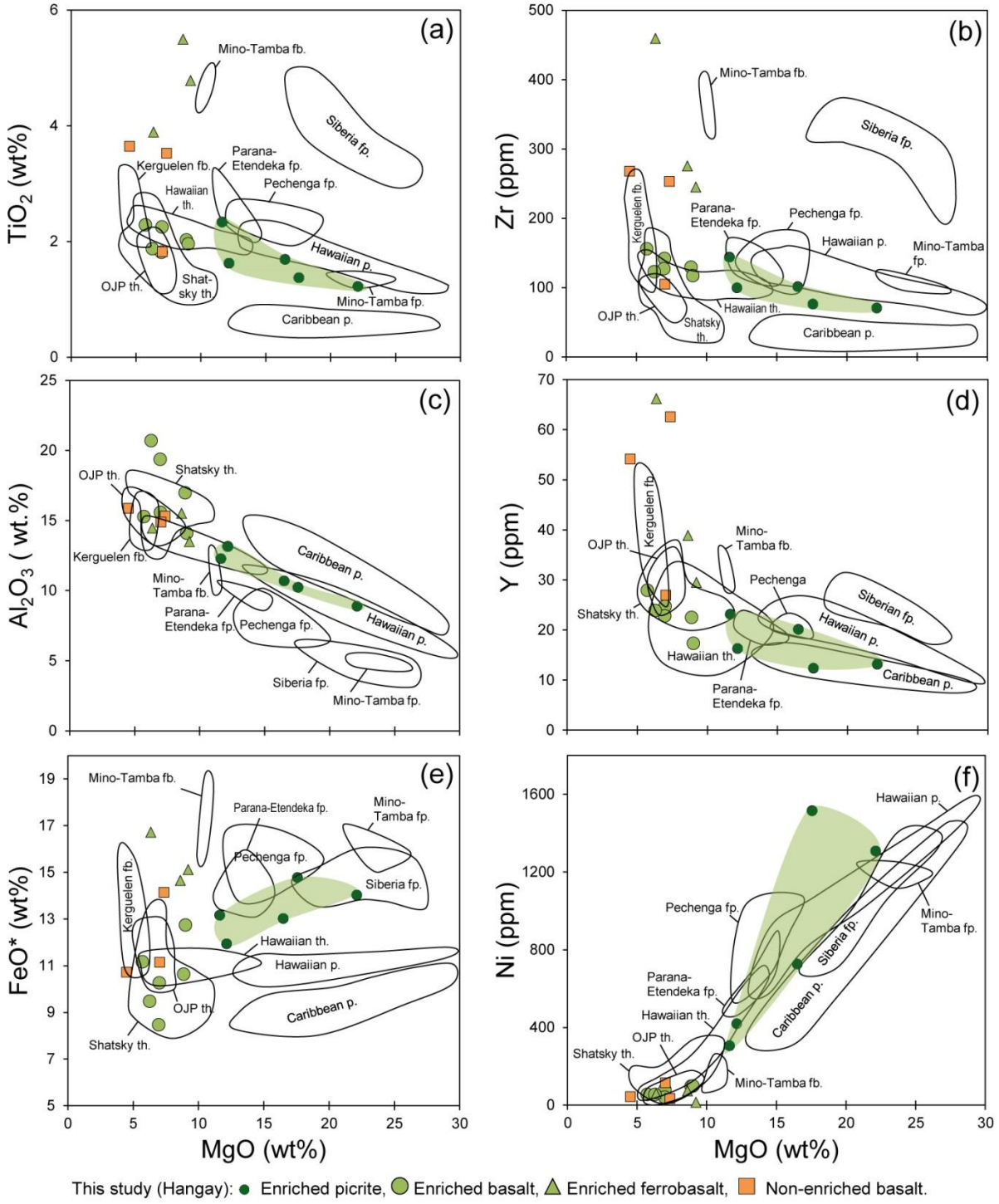

Figure 4.2 Major and trace element variations with respect to MgO of the Hangay basaltic greenstones. Data for these and subsequent figures are from: Hawaii (Norman and Garcia, 1999), Ontong Java (Tejada et al., 2002), Shatsky Rise (Sano et al., 2012), Kerguelen (Neal et al., 2002), Caribbean (Kerr et al., 1996; Révillon et al., 1999), Mino-Tamba (Ichiyama et al., 2006, 2008); Parana-Etendeka (Gibson et al., 2000), Siberia (Arndt et al., 1995), and Pechenga (Hanski and Smolkin, 1989; Hanski, 1992). Rock abbreviations: tholeiites (th.), ferrobasalts (fb.), picrites (p.), and ferropicrites (fp.).

The FeO*/MgO-SiO_2 and Zr/Ti-Nb/Y diagrams (Fig. 4.1) illustrate that all the basaltic greenstones are tholeiitic except for the high-Mg andesites that are calc-alkalic (see next section). The MgO variation diagrams (Fig. 4.2) show that the Hangay picrites contain unusually high FeO* contents compared to those of common picritic rocks from Hawaii (oceanic island) and the Caribbean (oceanic plateau), but their TiO_2 and Zr contents are intermediate between those of Hawaiian and Caribbean picritic rocks.

The Ni (14-1514 ppm), Cr (25-2550 ppm), and Co (107-26 ppm) contents gradually increase from basaltic rocks to picritic rocks among the Hangay greenstones (Table 2), indicating an olivine-spinel crystal accumulation process or increase of the degree of melting in the mantle. The Hangay basaltic greenstones exhibit two pronounced distributions in primitive-mantle-normalized plots (Fig. 4.3a-b). The most dominant basalts and picrites display a sub-parallel pattern with slight LREE enrichment similar to that of tholeiitic OIB in the primitive-mantle-normalized multi-element plot that indicates their common source, and for this reason, they are grouped as enriched plume-type. The ferrobasalts also exhibit parallel, but elevated patterns, and are thought to be fractionated varieties of enriched plume-type magma. In contrast to these rocks, some basalts (#35A, and #35B) and one dolerite (#14) exhibit a sub-horizontal pattern similar to that of E-MORB, and these are thus grouped as non-enriched plume-type (Fig. 4.3b). The enriched plume-type rocks show greater depletion in Y, Yb and HREEs and a positive Ti anomaly (except for sample #43B) in comparison with the non-enriched plume-type rocks (Fig. 4.3a).

4.1.2 Andesitic greenstones

The Hangay andesites have higher contents of MgO (up to 7 wt%), and SiO_2 (53-58 wt%), lower TiO_2 (0.7-1.0 wt%), and calc-alkalic compositions (Fig. 4.1). I refer to these rocks as “high-Mg andesite”. In this study, the Hangay andesites are compared with boninite from the Bonin Ridge forearc-seamount and high-Mg andesite (sanukite) from the Setouchi volcanic belt of SW Japan. The FeO*/MgO ratios (1.0-1.4) and TiO_2 (0.7-1.0 wt%) contents are higher than those of boninite (FeO*/MgO=0.5-0.9 and TiO_2<0.5 wt%) (Li et al., 2013) and closer to that of the Setouchi high-Mg andesites (FeO*/MgO =0.5-1.0 and TiO_2 0.4-0.9 wt%), (Tatsumi and Ishizaka, 1982) (Fig. 4.1). The most important characteristic of the Hangay high-Mg andesites is a pronounced depletion of Nb and Ta relative to neighboring incompatible elements in the primitive-mantle-normalized plot (Fig. 4.3d). These anomalies are

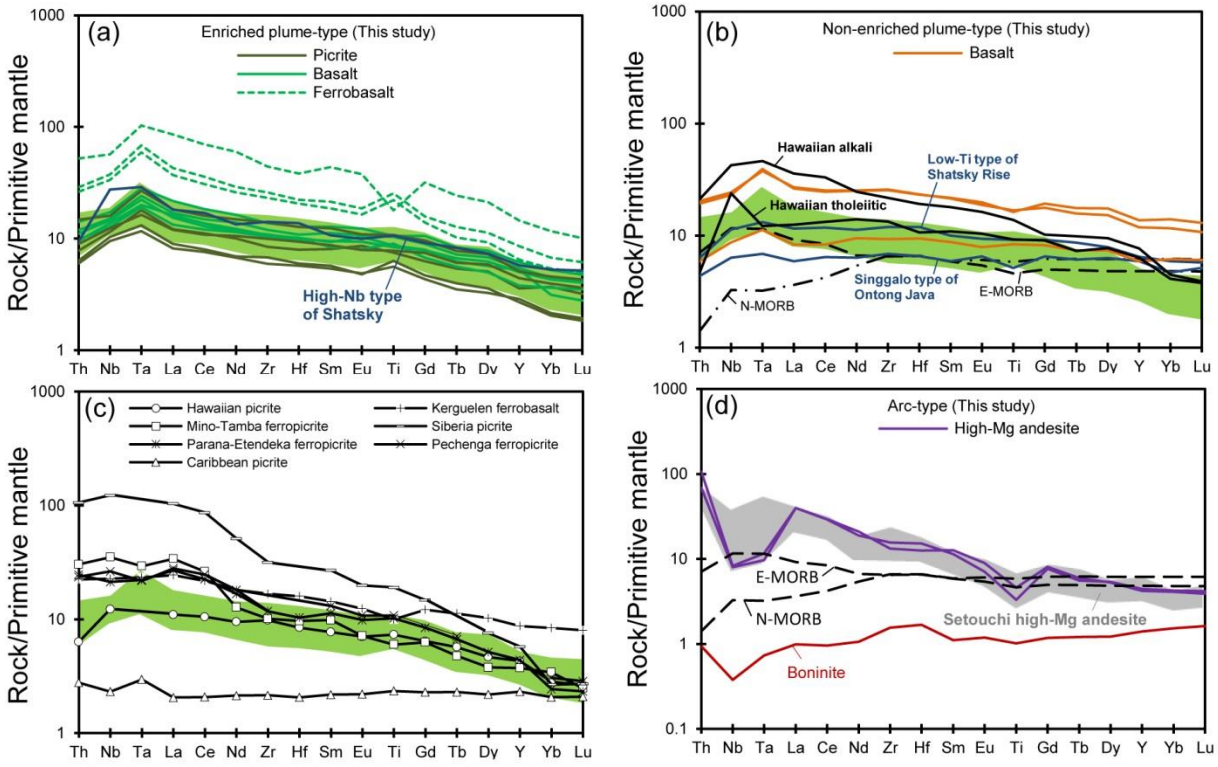

Figure 4.3 Primitive-mantle-normalized trace element profiles of the Hangay greenstones. The pattern for the Hangay picrites is reproduced, as green area, on diagrams a, b and c for comparison. (a) Enriched plume-type greenstones compared with the average of high-Nb type basalts of Shatsky Rise (Sano et al., 2012). (b) Non-enriched plume-type basalts are compared with the averages of the low-Ti type of Shatsky Rise (Sano et al., 2012), Singgalo type of Ontong Java (Fitton and Godard, 2004, and Hawaiian tholeiitic and alkali basalts (Best, 2003). (c) For comparison, terrestrial tholeiitic and picritic basalts, ferrobasalts and ferropicrites (references as in Fig.5) are shown. (d) Arc-type greenstones. Data used for comparison from Setouchi and Choshi, Japan as shaded area (Tatsumi et al., 2006; Hoang et al., 2009), and boninite from the Hahajima Seamount (Li et al., 2013). Primitive-mantle, enriched mid-ocean ridge basalt (E-MORB), and normal mid-ocean ridge basalt (N-MORB) values are from Sun and McDonough (1989).

attributed to the strong immobility of Nb and Ta in aqueous fluids rising from subducted slab into the mantle wedge (Condie, 2001; Tatsumi and Ishizaka, 1981, 1982; Tatsumi et al., 2006). In addition to the Nb and Ta depletion, the Hangay high-Mg andesites are consistently enriched in the most incompatible elements compared with boninites (Fig. 6d) but their enrichment is similar to that of Setouchi high-Mg andesites.

4.2 Mineral chemistry

Well-preserved igneous clinopyroxenes, hornblendes, and spinels were analyzed from the picrites, basalts, and high-Mg andesites. Representative mineral analyses are summarized in Tables 3-6, and plotted in Figs 4.4-4.7.

4.2.1 Clinopyroxene composition

The analyzed clinopyroxenes (n=82) from the basaltic greenstones correspond to augite with an average composition of $Wo_{42}En_{48}Fs_{10}$ and follow a characteristic tholeiitic fractionation trend, whereas clinopyroxenes (n=15) from the high-Mg andesite show Ca-enriched diopsidic rim (average of $Wo_{43}En_{48}Fs_{9}$), on a ternary plot (Fig. 4.4a). Figure 4.4b, shows that the clinopyroxene from both the basaltic and andesitic greenstones plot in the tholeiitic and calc-alkalic field. Although no compositional differences are observed in their Mg# (=Mg/(Mg+Fe^{2+}) atomic ratio), which ranges from 0.77 to 0.87 (in cores), distinct magmatic trends are observed in the Si versus Mg# plot (Fig. 4.4c). These differences are also observed in the core-to-rim major element concentrations of the clinopyroxenes (Fig. 4.4b and Table 3). Crystal rims in basaltic rocks are Fe- and Ti-enriched compared with the Ca- and Mg-enriched cores. In contrast, some crystal rims in andesites (sample #42) show Fe- and Ti-depletion compared with the Ca- and Mg-depleted cores. This suggests that the crystal cores in the basaltic rocks formed in Mg-rich melts whereas their rims crystallized from more fractionated Fe-rich magmas. In contrast, the andesitic rocks contain reversely zoned clinopyroxene phenocrysts, possibly due to magma mixing.

Trace element compositions were measured mostly on phenocryst cores (Table 3). In terms of the chondrite-normalized REE patterns (Fig. 4.5), the relict clinopyroxenes from the Hangay basaltic greenstones exhibit convex patterns with slight depletion in both LREES and HREEs. On the other hand, clinopyroxenes and hornblendes from the high-Mg andesites show a sub-parallel and an enriched-LREE pattern with Ti-depletion. A crystal rim measured in picrite (sample #12) shows higher trace element concentrations than does its core and is similar to compositions measured on clinopyroxene cores of the basalt. This could mean that the picrite represents a primitive, less evolved portion of the basaltic magma, and is not a simple olivine accumulation product.

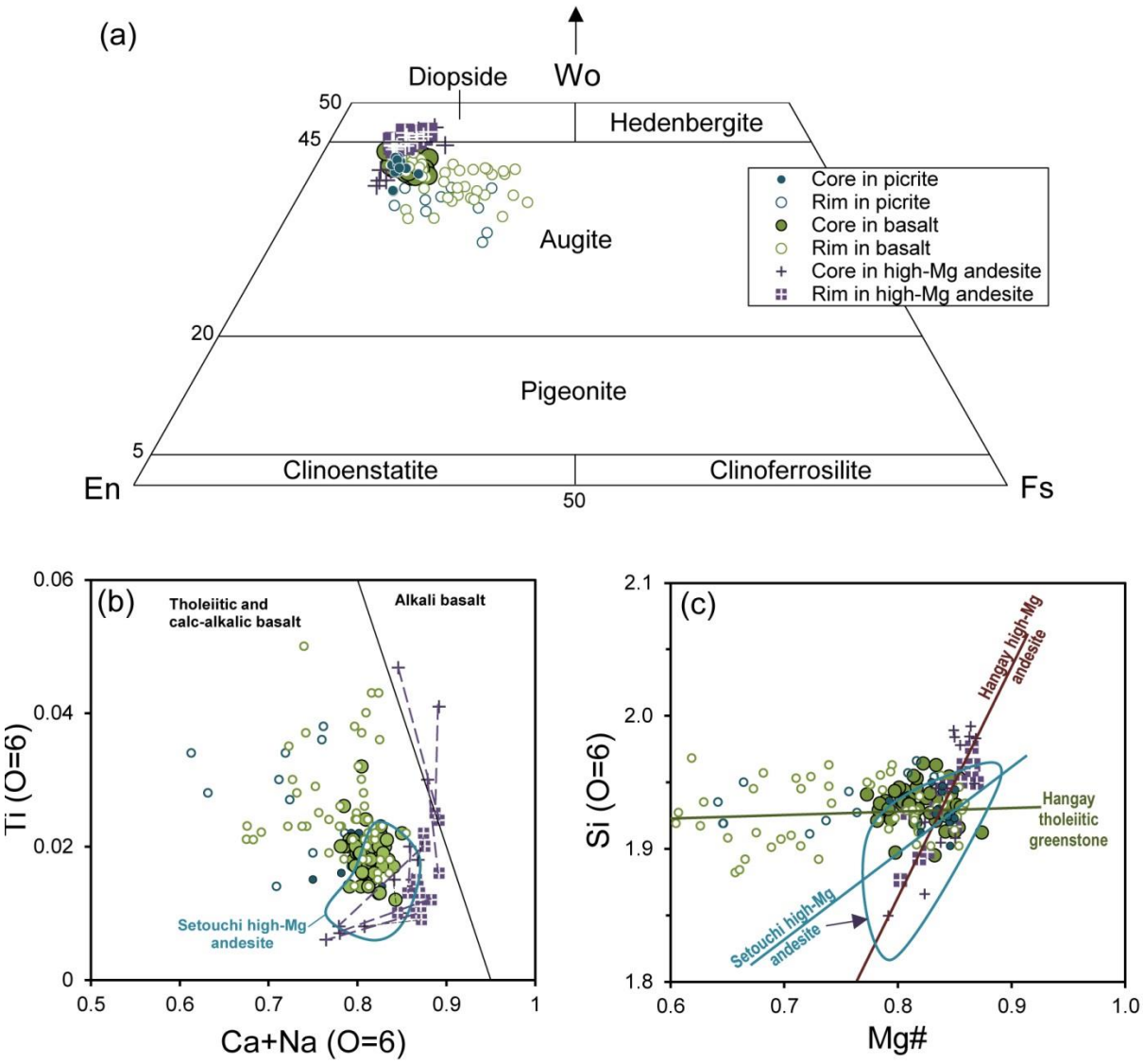

Figure 4.4 Chemical characteristics of clinopyroxenes in the Hangay greenstones: (a) Classification plot after Morimoto et al. (1988). (b) Discrimination diagram after Leterrier et al. (1982). Cores and rims of the reversely zoned clinopyroxenes in the high-Mg andesites are connected by broken lines. (c) Si-Mg# (Mg#=Mg/(Mg+Fe^{2+}) atomic ratio) relationship plot. A linear reduction is shown for each group. Clinopyroxenes from the Setouchi high-Mg andesite (outlined) are shown for comparison (Tatsumi et al., 2003, 2006).

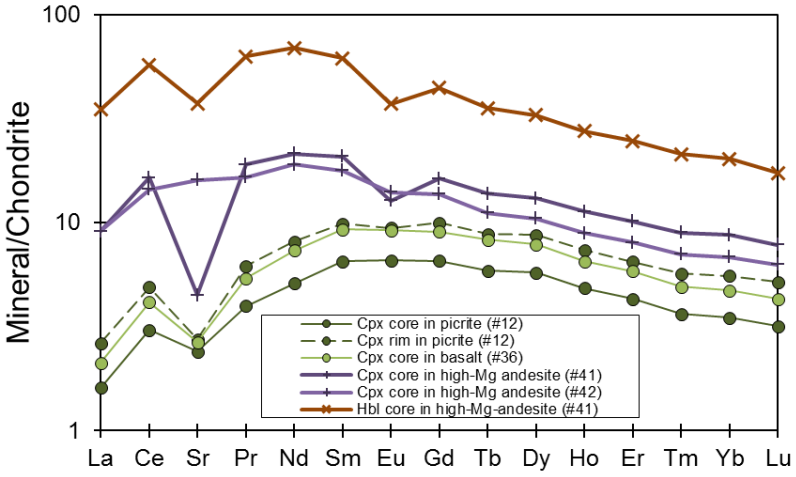

Figure 4.5 Chondrite-normalized trace element profiles of clinopyroxenes and hornblendes in the Hangay greenstone. Chondrite value is from Sun and McDonough (1989).

4.2.2 Spinel composition

The chemical compositions of spinels were analyzed mostly in picrites, high-Mg andesites, and some sparsely olivine-phyric basalts (Table 5). The Cr# (=Cr/(Cr+Al) atomic ratio) of 0.54-0.70 of spinels in the Hangay basaltic-picritic greenstones is higher than that of spinel in MORB, resembling that of Hawaiian tholeiitic basalt and picrite, which these spinels also resemble in terms of Ti (Fig. 4.6), but

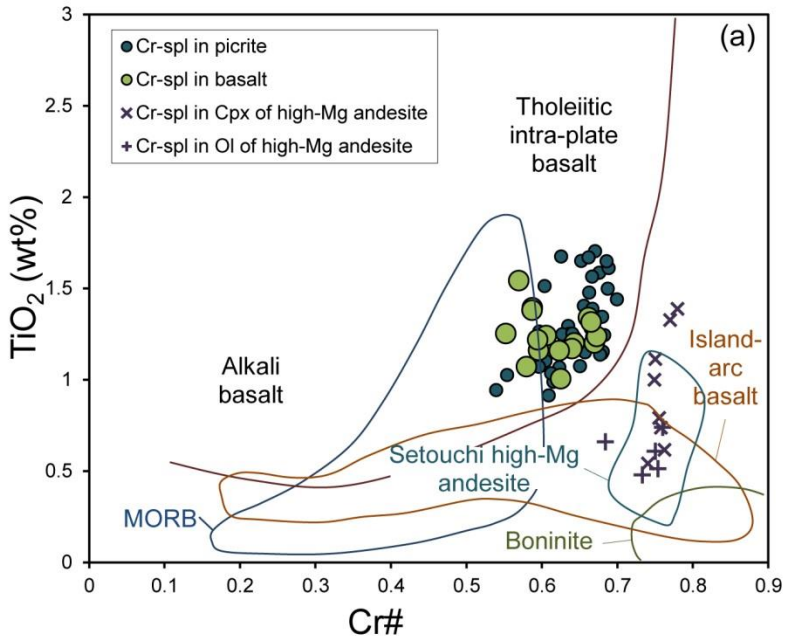

Figure 4.6 TiO_2-Cr# (Cr#=Cr/(Cr+Al)atomic ratio) relationship plot after Arai (1992). Data from high-Mg andesite from the Setouchi belt, SW Japan (Tatsumi et al., 2006).

the spinels are distinctly lower in Fe^{3+} than the Hawaiian spinels (Fig. 4.7a). Spinels in the high-Mg andesite (Cr# 0.61-0.78) are higher in Cr# and Fe^{3+}, and lower in Ti than spinels in the basaltic-picritic greenstones, and are closer to those in the Setouchi sanukitic high-Mg andesite (Fig.4.6). It implies that the high-Mg andesites were generated from the highly depleted magma source compared with the basaltic-picritic greenstones, but lesser depleted source than boninites. As shown on the spinel TiO_2-Cr# plot (Fig. 4.6), the basaltic-picritic greenstones and high-Mg andesites correspond to the intra-plate tholeiite and island-arc basalt fields, respectively.

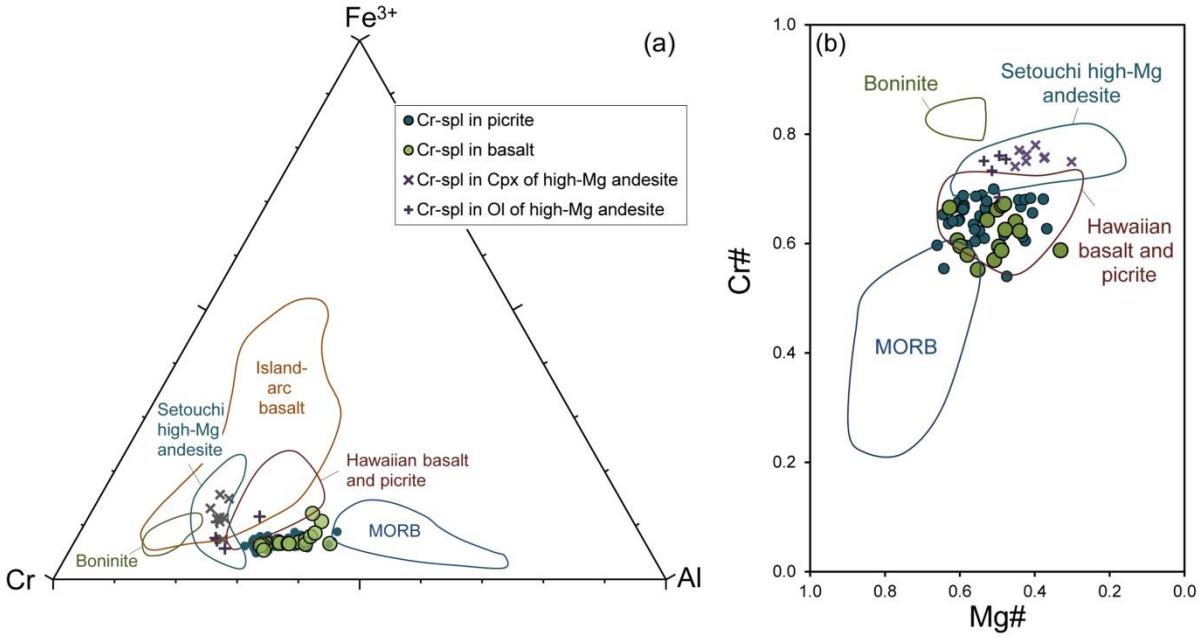

Figure 4.7 (a) Al-Cr-Fe^{3+} trivalent cation plot. (b) Relationship between Cr# (=Cr/(Cr+Al)atomic ratio) and Mg# (=Mg/(Mg+Fe^{2+})atomic ratio) after Barnes and Roeder, (2001).Spinel data fields: High-Mg andesite from Setouchi belt, SW Japan (Tatsumi et al., 2006); MORB-mid ocean ridge basalt (Sigurdsson and Schilling, 1976; Dick and Bullen, 1984); Island arc basalt (Barnes and Roeder, 2001); Hawaii tholeiitic picrite and basalt (Nichols and Stout, 1988; Wilkinson and Hensel, 1988); Boninite from Sobolev et al. (1994) for comparison.

CHAPTER 5 DISCUSSIONS

Here I now discuss the petrogenesis and geotectonic significance of the Hangay greenstones, with focus on the newly discovered tholeiitic picrites (ferropicrites) and calc-alkalic high-Mg andesites and the field relationship between the basaltic greenstones and the deep-water pelagic chert.

5.1 Petrogenesis of the basaltic greenstones

Generally, well-studied oceanic islands display a characteristic geochemical evolution over their volcanic histories as was defined for the Hawaiian Islands (e.g. MacDonald and Katsura, 1964). For instance, most of the mass of oceanic islands is formed during the shield-building stage, when typically up to 98% of the volcanic edifice is produced in a relatively short time span (<5 m.y.). During this stage, almost entirely tholeiitic or mildly alkalic basalts form from relatively large mantle melt fractions. Subsequently, alkali basalts that form by smaller degrees of partial melting may cover the shield volcano as cap rock (Condie, 2001; Staudigel and Clague, 2010). This evolution is also applicable to many other oceanic intraplate volcanoes, including oceanic plateaus (Tejada et al., 1996; Kerr et al., 2000; Kerr and Mahoney, 2007; Bryan et al., 2008). Accordingly, in the primitive-mantle-normalized incompatible element plots (Fig. 4.3), the Hangay basaltic greenstones are similar to basalts drilled from the upper part of many oceanic islands and plateaus such as Hawaii (Garcia et al., 2010), Ontong Java (Fitton and Godard, 2004), Shatsky Rise (Sano et al., 2012), and Kerguelen (Frey et al., 2000; Neal et al., 2002). In particular, the enriched plume-type basalts of the Hangay greenstones show slightly depleted LREE patterns, similar to those of high-Nb type basalts of Shatsky Rise (Fig.4.3a), whereas the non-enriched type with relatively flat patterns is similar to basalts of the low-Ti type at Shatsky Rise and of the Singgalo type at Ontong Java (Fig. 6b). Moreover, the relatively depleted HFSEs of the enriched plume-type basalts in this plot would be interpreted to indicate residual garnet in the mantle source, whereas the nonenriched-plume type has only weak depletion of HREEs.

Comparisons of major and trace elements among the Hangay tholeiitic basalts and other terrestrial tholeiitic lavas reveal similarities with Hawaiian oceanic island lavas and Ontong Java, Shatsky Rise and Kerguelen oceanic plateau lavas (Fig. 4.2). However, the Hangay picrites are distinguished from other picritic rocks (e.g. Hawaiian, Caribbean) by their relatively high abundance of Fe_2O_3* (>12.85 wt%). Their Ti and Zr contents are intermediate between those of Hawaiian and

Caribbean picrites at given MgO. These unusual geochemical characteristics partly resembling the high-Fe and -Mg rocks of the Pechenga area (Kola Peninsula, Russia, Hanski and Smolkin, 1989; Hanski, 1992), Parana-Etendeka area (Gibson et al., 2001), Siberia LIP (Arndt et al., 1995) indicate that the Hangay picrites have ferropicritic rather than komatiitic affinity (Figs. 1.2 and 4.2). The Hangay picritic rocks occur at the base of a massive lava pile and form only thin olivine-rich zones (thickness of ~30 cm) compared to the rest of the basaltic flows. Gibson (2002) suggested that high-Fe and -Mg magmas (komatiites and ferropicrites) typically occur at basal cumulate zones of thick tholeiitic volcanic sequences as the earliest melting stage of mantle plume starting-heads (e.g., Parana-Etendeka, Gorgona of the Caribbean, Siberia etc.). This is a diagnostic feature of LIPs including continental flood basalts and oceanic plateaus. However, high-Fe and -Mg magmas also form later stage dikes and sills after the main basaltic activities (e.g. Mino-Tamba, SW Japan and Siberian LIPs, Russia: Hanski and Smolkin, 1989, 1995; Ichiyama et al., 2006; Goldstein and Francis, 2008). The concept of melting of a heterogeneous mantle source of peridotite with enriched domains such as solidified partial melt pockets or recycled Fe-rich material (eclogites of basaltc or gabbroic origin), has been proposed by several workers as a mechanism for generating unusually high Fe melts while maintaining high Mg content (Hanski and Smolkin, 1989; Hanski, 1992; Gibson et al., 2000; Gibson, 2002; Tuff et al., 2005; Ichiyama et al., 2006; Goldstein and Francis, 2008). For example, Tuff et al. (2005) proposed garnet-pyroxenite as the magma source of the Parana-Etendeka ferropicrite. Goldstein and Francis (2008) demonstrated that Archean ferrobasalts from the Western Superior Province, Ontario, Canada were generated by melting of an olivine-dominated mantle source with a Mg# of ~0.85 at ~5GPa. Gibson (2002) suggested that high-Fe and -Mg melts were produced by a moderate amount of partial melting of “re-feritilized” peridotite at potential temperatures of >1450°C and pressures >4.5 GPa. His study also suggested that hybrid Fe-rich peridotite is thought to result from a series of progressive mixing and reaction processes between subducted oceanic crust (eclogite) and convecting peridotitic mantle. It is interpreted that contribution of recycled oceanic crust (eclogite after basalt or gabbro) to the Hangay basaltic greenstones accounts for their slight LREEs enrichment similar to that of tholeiitic OIB (Fig. 4.3).

In terms of incompatible and REE distributions in these various oceanic tectonic settings, the overall element distributions in the Hangay basaltic greenstones are similar to those of oceanic island and oceanic plateau basalts. However, the presence of ferropicrite among the studied Hangay

greenstones strongly suggests that the Hangay greenstones were originated in an oceanic plateau setting rather than having an oceanic island origin because ferropicrites have been found in only Archean to Cenozoic LIPs including oceanic plateaus, but not yet from oceanic islands (Gibson et al., 2000, Gibson, 2002). Moreover, the voluminous tholeiite with slight LREEs enrichment, similar to tholeiitic OIB in the primitive-mantle-normalized plot, an abundance of ferrobasalt, an absence of alkali basalt and the fact that the tholeiite is directly covered by deep-water pelagic chert in the study area also supports this idea.

5.2 Nature of the source of the Hangay basaltic greenstones

The differences between plume- and arc-derived greenstones are seen clearly on the Nb/Y against Zr/Y trace element ratio plot of Fitton et al. (1997) (Fig. 5.1a). As expected, the arc-type high-Mg andesites plot well away from the basaltic greenstones and confirm their subduction zone origin, whereas the plume-type greenstones plot on the Iceland array. This plot as well as the other plots as discussed above (Figs. 4.2-4.6) show that all of the basaltic greenstones of the Hangay region appear adjacent to one another and form a distinct trend, implying a common magmatic origin. However, there are slight differences in the ratios of Nb/Y and Zr/Y among the Hangay basaltic greenstones, suggesting different degrees of melting (Fitton et al., 1997), which could be controlled by two different processes: (1) increasing melt fraction and decreasing depth of melting with plume ascent (Lassiter and DePaolo, 1997), or (2) varying degrees of melting related to regions with different compositions in a mantle plume head (Condie, 2001; Ichiyama et al., 2008).

(Process 1) Although oceanic plateaus differ geochemically from continental flood basalts, studies indicate that some lithospheric thinning may occur during the formation of an oceanic plateau (Lassiter and Depaolo, 1997). If this were the case for the Hangay basaltic greenstones, the enriched-type basalts and picrites that were generated by smaller degrees of melting would have melted earlier at greater lithospheric thickness than the later non-enriched type basalts. The thickness of lithosphere beneath which Hangay basaltic greenstone magma melting occurred, can be predicted by comparing well-studied oceanic island and plateau basalts. According to the Nb/Y and Zr/Y ratio plot (Fig. 5.1a), the ratios in the Hangay basaltic greenstones are distinctly higher than those of Ontong Java oceanic plateau basalts, but lower than those of Mino-Tamba oceanic plateau picrites.

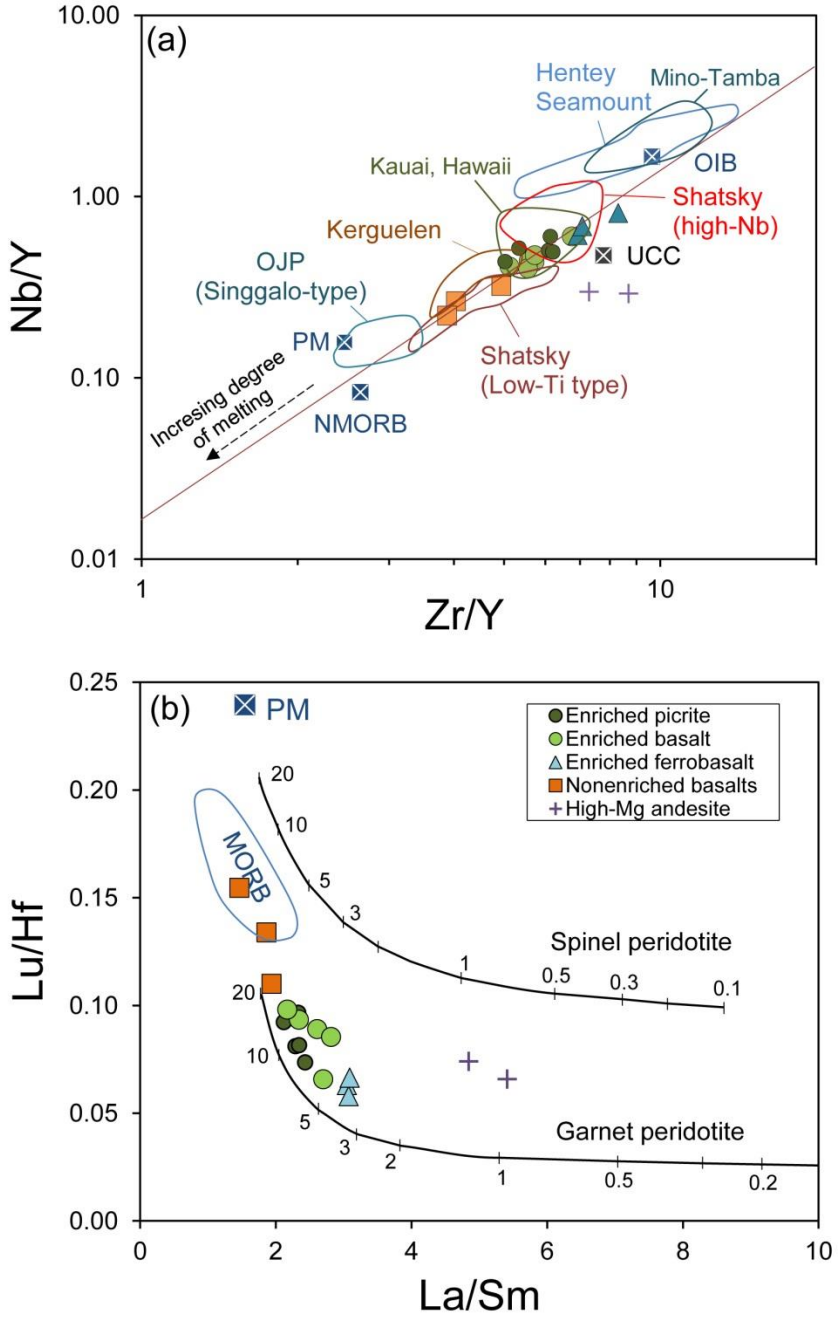

Figure 5.1 (a) Nb/Y-Zr/Y variation diagram for the Hangay greenstones. Diagonal line (Fitton et al., 1997). Data are from low-Ti type basalts of Shatsky Rise (Sano et al., (2012), Singgalo type basalts of Ontong Java (Fitton and Godard, 2004), alkali basalt of Hentey (Tsukada et al., 2013), tholeiitic basalt of Hawaii (Garcia et al., 2010), and ferrobasalt of Kerguelen (Neal et al., 2002) and picritic basalts of Mino-Tamba (Ichiyama et al., 2008). (b) Lu/Hf-La/Sm variation diagram of Hangay basaltic greenstones (after Regelous et al. 2003). Primitive-mantle (PM), enriched mid-ocean ridge (E-MORB), normal mid-ocean ridge (N-MORB), and oceanic island basalt (OIB) values from Sun and McDonough (1989). Upper continental crust (UCC) value from Condie, (1993).

Fitton and Godard (2004) suggested that the Ontong Java Plateau magmas were produced by a large degree of melting (30% melting of a peridotitic primitive magma source) of very hot (>1500°C) mantle beneath very thin lithosphere. In contrast, the Mino-Tamba picritic greenstones were produced by partial melting of a deep mantle (4-5GPa) source with recycled eclogite beneath thick oceanic lithosphere (Ichiyama et al., 2008). It is suggested that the Hangay greenstones may have been generated at an intermediate lithospheric depth comparable to those of Hawaiian tholeiites, Kerguelen ferrobasalts, and high-Nb type basalts of Shatsky Rise. In contrast to the enriched type, the non-enriched type has slightly lower Nb/Y and Zr/Y ratios, similar to those of the low-Ti type basalt of Shatsky Rise (>15% degree of melting) and the Singgalo type basalt of Ontong Java, suggesting a higher degree of melting for the non-enriched type. As a plume rises to the lithosphere, adiabatic decompression results in lower solidus temperatures and causes progressively greater degrees of melting (Condie, 2001). This indicates that the source of the non-enriched-type basalts underwent a greater degree of melting than the source of the enriched type that caused its flat HREE pattern on the primitive-mantle-normalized plot, with no garnet left behind in the residue (Kerr et al., 2000). This is confirmed by their higher Lu/Hf and lower La/Sm ratios in Figure 5.1b. This plot suggests that the dominant enriched plume-type basalts represent garnet peridotite melts formed at medium degrees of melting (5-15 %), whereas the non-enriched type basalts represent melts produced by higher degrees of melting (>20%) within the same garnet peridotite field.

(Process 2) The differences in the degrees of melting between the Hangay enriched and non-enriched types of basalts could also indicate the regions with different compositions in the mantle plume head. According to the plume models of Griffiths and Campbell (1990), the hottest part of a new upwelling mantle plume is the central conduit or tail. The Hangay picrite and ferropicrite may represent the melting products of the hottest part of the upwelling plume (>1500°C), and the voluminous enriched plume-type basalts may be the result of melting of cooler parts of the plume. The ferrobasalts with parallel and elevated patterns in the primitive-mantle-normalized plot (Fig. 4.3) may be the shallow fractionation product of this magma. From the discussion in above section, it is apparent that the non-enriched plume-type basalts were generated by higher degrees of melting at shallower depths in the rising plume (Fig. 5.1). Furthermore, smaller volumes of melting that occurred at the deep plume tail may have produced smaller amounts of enriched alkali basalts, such as those reported by Tsukada et al. (2013) in other parts of the Hangay-Hentey belt. In addition, the enriched ferrobasalt

and non-enriched basalts are in direct contact with chert (Figs. 3.1 and 3.2), implying that they may have erupted after the most dominant enriched-plume type magma (enriched basalt and picrite). The absence of alkali basalt, which is most characteristic for oceanic islands or seamounts as well as oceanic plateaus, as stated above, may suggest that the Hangay plume-derived magma activity in the study area occurred within a short period of time on the axis of the plume, and that the site of the plume magmatism then shifted to other areas.

In addition, the Hangay tholeiitic greenstones show a notably low ratio of Nb/Y (0.3-0.8) compared with the alkali basaltic greenstones studied from coeval accretionary terrane in the Hentey region with HIMU and OIB affinities (Tsukada et al., 2006, 2013; Safonova et al., 2009). This may suggest intra-oceanic magmatic heterogeneity within the Hangay-Hentey paleo-ocean basin in Middle Paleozoic time.

5.3 Petrogenesis of the high-Mg andesites

The Hangay high-Mg andesites are clearly distinguished from the Hangay basaltic greenstones by their glassy texture (<10 vol.% of phenocrysts) (Fig. 3.10), calc-alkalic chemical trend (Fig. 4.1), high MgO content (up to 7 wt%), significant enrichment of LREEs and depletion of Nb and Ta (Figs. 4.3, 4.5) and the appearance of reversely zoned clinopyroxene phenocrysts (Fig. 4.4). These features confirm their arc-derived origin. High-Mg andesite occurrences have been reported from the Bonin Islands, the western Pacific (boninites), the California Peninsula (bajaite) and the Setouchi belts in SW Japan (sanukite). The Hangay high-Mg andesites differ from boninite (FeO*MgO=0.5-0.9 and TiO_2<0.5 wt%) and bajaite by their higher FeO*/MgO (1.0-1.4), TiO_2 (0.7-0.9 wt%), and Y and Yb contents (Fig. 1.3). Furthermore, the rock is also enriched in LREEs in contrast to boninites, which show no LREE enrichment (Fig. 4.3d). The Hangay high-Mg andesites also do not contain phenocrysts of clinoenstatite, magnesian pigeonite, or bronzite, but boninites often do. Consequently, it is compositionally similar to the “sanukitic” high-Mg andesite reported from the Setouchi volcanic belt of SW Japan (Figs. 1.2, 4.1, 4.3d, and 4.6). The high abundances of Ni (45-74 ppm), Co (16-24 ppm), and Cr (200-300 ppm) supported by high Mg# and Cr# of spinel suggest that the Hangay high-Mg andesites were derived from melting of mantle wedge peridotite (Tatsumi and Ishizaka, 1981, 1982; Shimoda et al., 1998, Tatsumi et al., 2006). It is widely accepted that most arc magmas are derived from hydrous melting of peridotites in the mantle wedge induced by fluids released from subducted

oceanic crust or overlying sediments. However, the high-Mg andesite may not be generated by steady subduction, but only rarely by subduction of a young and hot oceanic slab or at the initiation of subduction (Tatsumi and Ishizaka, 1982; Tatsumi et al., 2001, 2006; Kamei et al., 2004; Li et al., 2013).

5.4 Geotectonic implications

Because geochemical and petrological evidences combined with field observations clearly reveal that the basaltic and andesitic greenstones of Hangay were generated from different magma sources, it is possible to propose the following tectonic reconstruction model for the Hangay region (Fig. 5.2). An oceanic plateau was generated in the pelagic region (probably below the carbonate compensation depth) of the Hangay-Hentey paleo-ocean during the Devonian and it also implies that the ocean was wide. The subduction direction was probably the same as that for the Bayanhongor ophiolite zone, where SW-dipping and NE-vergent thrusting occurred (Buchan, 2001; Tomurtogoo, 2006; Osozawa et al., 2008). During subduction of the oceanic crust beneath the active continental margin of the Central Mongolian (or Tuva-Mongolian) Massif probably in the Early Carboniferous, the oceanic plateau approached the subduction zone and jammed in the trench. A part of the oceanic plateau was sliced off during subduction and incorporated into trench sediments. Only the uppermost section of the plateau was sliced off, as evidenced by the direct contact with chert and an absence of plutonic rocks. The jam forced the subduction zone to move oceanward (to the NE), where younger oceanic plate existed (so called “back-stepping”). Such subduction back-stepping occurred in the Caribbean plateau, when the oceanic plateau collided with the northwestern active continental margin of South America (Kerr and Mahoney, 2007 and references therein). After this occurred, a subsequent Hangay arc system formed along the new subduction zone, and the high-Mg andesites were intruded into the accreted oceanic and trench deposits. One possible explanation of the origin of the high-Mg andesite is that the newly subducting oceanic crust probably contained a hot and young oceanic ridge that caused the excess heat that produced the high-Mg andesitic rocks (Fig. 5.2). A good example of this is the Miocene Setouchi volcanic belt, which formed by subduction of very young oceanic lithosphere of the Philippine Sea plate beneath the Eurasian plate that produced sanukitic high-Mg andesites (Tatsumi and Ishizaka, 1982; Tatsumi et al., 2001, 2006). After the arc had already evolved to mature stage, the Permian-Triassic granitoids were intruded widely throughout the Hangay region (Kovalenko et al., 1996; Orolmaa et al., 2008, 2010) and the front of the active continental margin migrated to the

NE, or oceanward. The arc-derived magmatism that occurred through the subduction-accretionary process in this area, probably led to the formation of the gold deposits in the Uyanga area (Ult gold placer), which is being mined today. I infer that there is no underlying cratonal basement beneath the Hangay-Hentey belt, at least not in the southern Hangay region. In addition, the distribution of Permian shallow marine molasses unconformably overlying extensive Devonian-Carboniferous deposits may suggest that closure of the Hangay-Hentey paleo-ocean occurred in the Late Permian in the Hangay region.

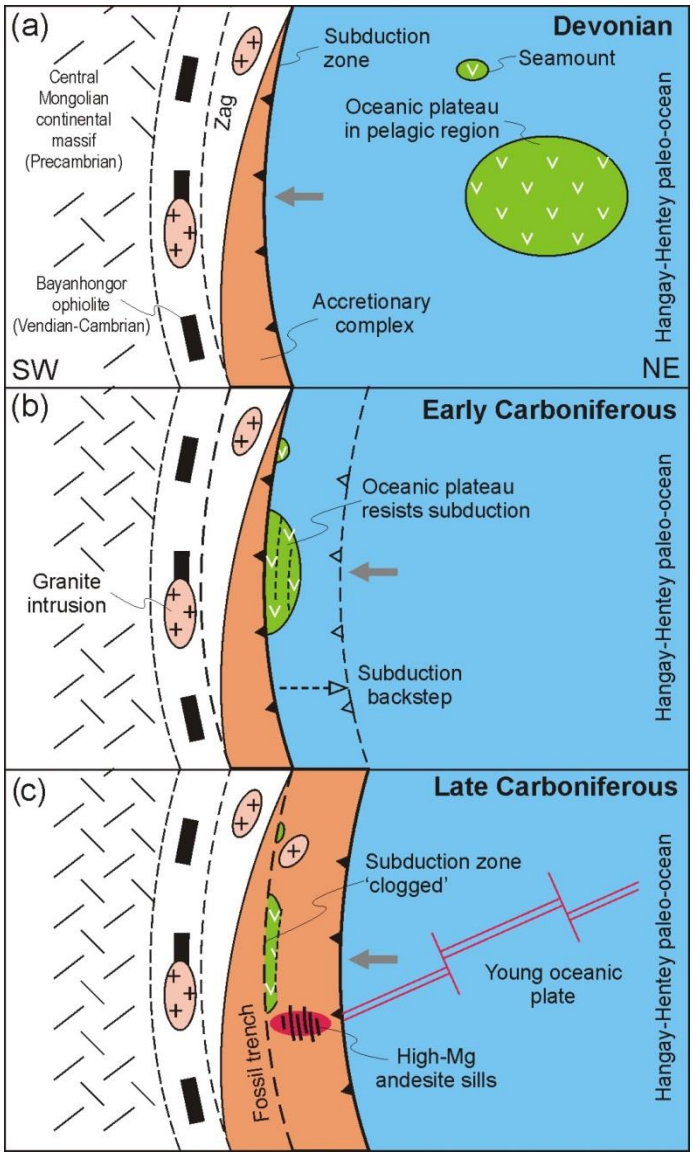

Figure 5.2 Tectonic reconstruction of westernmost part of the Hangay-Hentey belt from Early Devonian to Carboniferous. (a) A Devonian oceanic plateau forms within the Hangay-Hentey paleo-ocean. (b) The oceanic plateau approaches the subduction zone and obduction/jamming occurs. (c) An arc form. Detailed interpretations are given in the text.

CHAPTER 6 CONCLUSIONS AND SUMMARY

The present investigation of greenstones from the Hangay region established the following new understandings of the Paleozoic orogeny that formed an integral part of Central Asian Orogenic Belt.

1. The lower portion of the Early to Middle Devonian Erdenetsogt Formation in the Hangay region consists of a chert-, siltstone-, and basaltic greenstone-dominated sequence of a typical oceanic plate stratigraphy.
2. The first detailed geochemical and petrological study combined with field observations of the greenstones from the Hangay region revealed that the Hangay greenstones were generated in two distinct geotectonic settings and from two differeny magma sources. (1) deep-seated, mantle-plume derived, high Fe- and Mg- tholeiitic greenstones that formed an oceanic plateau, and (2) arc-derived calc-alkalic high-Mg andesites related to subduction of young oceanic plate.
3. The oceanic plateau greenstones at Hangay are characterized as voluminous tholeiitic greenstones that include picrite, ferropicrite, and fractionated ferrobasalt with no Nb and Ta negative anomalies and slight LREE enrichment, similar to tholeiitic OIB.
4. The arc-derived high-Mg andesites are characterized by a pronounced depletion in Nb and Ta, LREE enrichment and the characteristic feature of glassy texture and mineral chemistry resembling that of sanukitic high-Mg andesites.
5. The Hangay plume-derived greenstones developed as an oceanic plateau within the deep-water pelagic region of the Hangay-Hentey paleo-ocean during the Devonian, whereas the Hangay high-Mg andesites were produced by subduction-zone magmatism that occurred after accretion of the oceanic plateau.
6. The occurrence of ferropicrite, abundance of ferrobasalt, and dominance of tholeiite that is directly covered by chert provide visible evidence for the oceanic plateau origin of the Hangay greenstones. On the other hand, the high-Mg andesite sills provide evidence for the initiation of subduction-zone magmatism in this accretionary complex.

ACKNOWLEDGMENTS

Many people have helped make this thesis a reality for me.

First of all, I want to thank my supervisor, Prof. Akira Ishiwatari. Everything positive about my academic experience here at Tohoku University, as well as on cruise of IODP, Expedition 330 can be attributed to you. I very much enjoyed working on greenstones, and found my thesis topic stimulating and exciting. You are always available to answer questions and to give advice and feedback, and your open-door policy was very much appreciated. I have benefit from your knowledge and years of experience, both in field and in academic research environment. A very big thank to you.

I would like to thank Dr. Demberel Orolmaa, senior researcher at Institute of Geology and Mineral Resources of Mongolian Academy of Sciences, for her assistance and guidance in the field. A.Togt-Erdene and B.Bathuyag are greatly appreciated for their field drive in Mongolia.

I am very grateful to Tsuyoshi Miyamoto for his assistance and advice with XRF and SEM-EDS analysis at the Department of Earth Science, Tohoku University.

Thank to Professor Shoji Aria who gave a chance to analyze my samples at the Department of Earth Science of Kanazawa University and ability to have meaningful discussions about my research. Thank to Dr. Akihiro Tamura for his guidance to operating the LA-ICP-MS at Kanazawa and process the analyze data.

I would like to thank all my research group members of Geology-Petrology laboratory of the Department of Earth science, Graduate School of Science, Tohoku University for their constant assistance, advice, and variable comments on my research. Thank you to all very much -all the good times, parties, and field trips etc. It certainly made my time in Japan much more enjoyable.

I wish to thank to Dr.Naoto Hirano and Prof. Jargalan Sereenen for their advice and discussions.

I am very grateful to the IGPAS (MEXT) scholarship including an IIARE from which I received the funding for my research at Tohoku University.

Finally, thank you very much to my family, for their constant support throughout my degree. Thank you very much.

REFERENCES

Amantov, V.A., Blagonravov, V.A., Borzakovsky, Yu.A., Durante, M.V., Zonenshain, L.P., Luvsandanzan, B., Matrosov, P.S., Suetenko, O.D., Filippova, I.B. and Khasin, R.A. (1970) Main features of Paleozoic stratigraphy of Mongolia in stratigraphy and tectonics of Mongolia (Marinov, N.A. Ed.). Nauka, Moscow, 8-62. (in Russian)

Arai, S. (1992) Chemistry of chromian spinel in volcanic-rocks as a potential guide to magma chemistry. Mineralogical Magazine, 56(383), 173-184.

Arndt, N., Lehnert, K. and Vasil'ev, Y. (1995) Meimechites: highly magnesian lithosphere-contaminated alkaline magmas from deep subcontinental mantle. Lithos, 34(1–3), 41-59.

Arndt, N., Chauvel, C., Czamanske, G. and Fedorenko, V. (1998) Two mantle sources, two plumbing systems: tholeiitic and alkaline magmatism of the Maymecha River Basin, Siberian flood volcanic province. Contributions to Mineralogy and Petrology, 133, 297-313.

Badarch, G., W. D. Cunningham, W.D. and Windley, B.F. (2002) A new terrane subdivision for Mongolia: implications for the Phanerozoic crustal growth of Central Asia. Journal of Asian Earth Sciences, 21(1), 87-110.

Badarch, G., Orolmaa, D. and Erdenesaihan, G. (2003) Tectonic evolution of the Hangay-Hentey fold belt. Journal of Geologic Problems, 22 (06), 43-73. (in Mongolian)

Barnes, S.J. and Roeder, P.L. (2001) The range of spinel compositions in terrestrial mafic and ultramafic rocks. Journal of Petrology, 42(12), 2279-2302.

Bayarsaihan, T., Gansuh, Ts., Hurelbaatar, A., Dorjsuren, B., Henzii, S., Dagva-Ochir, Ya. and Orgil, Ts. (1988) Geological sheet maps L-47-4 and -10, 1:200,000. Geological mapping report 4421, Ulaanbaatar, Mongolia. (in Mongolian)

Best, M.G. (2003) Igneous and metamorphic petrology. pp.729, Backwell Science, Oxford.

Bryan, S.E. and Ernst, R.E. (2008) Revised definition of Large Igneous Provinces (LIPs). Earth-Science Reviews, 86, 175-202.

Buchan, C., Cunningham, W.D., Windley, B.F. and Tomurhuu, D. (2001) Structural and lithological characteristics of the Bayankhongor Ophiolite Zone, Central Mongolia. Journal of the Geological Society, 158(3), 445-460.

Bussien, D., Gombojav, N., Winkler, W. and von Quadt, A. (2011) The Mongol–Okhotsk Belt in Mongolia: An appraisal of the geodynamic development by the study of sandstone provenance and detrital zircons. Tectonophysics, 510(1-2), 132-150.

Byamba, J., Dorjsuren, B., Dorjnamjaa, D., Tomurkhuu, D. and Makhbadar, Ts. (2009). Central Mongolian fold belt. In Geology and mineral resources of Mongolia: Tectonics lithospheric plates. Vol, IV, (Byamba, J., Badamgarav, J., Bayasgalan, A., Arvisbaatar, N., Turutanov, E.H., Dorjsuren, B., Tomurhuu, D., Dejidmaa, G., Dorjnamjaa, D., Mahbadar, Ts. and Amarjargal, A. Eds.). pp.487, Soyombo printing, Ulaanbaatar, Mongolia, 199-302. (in Mongolian)

Condie, K.C. (1993) Chemical composition and evolution of the upper continental crust: Contrasting results from surface samples and shales. Chemical Geology 104(1-4), 1-37.

Condie, K.C. (2001) Mantle plumes and their records in Earth history. 5, Plumes as tracer of mantle processes. pp.306. Cambrage University Press, UK.

Dick, H.B. and Bullen, T. (1984) Chromian spinel as a petrogenetic indicator in abyssal and alpine-type peridotites and spatially associated lavas. Contributions to Mineralogy and Petrology, 86(1), 54-76.

Dorjsuren, B., Bujinlkham, B., Minjin, C. and Tsukada, K. (2006) Geological settings of the Ulaanbaatar terrane in the Hangay-Hentey zone of the Devonian accretionary complex, Central Asian Orogenic belt. In Structural and tectonic correlation across the Central Asian Orogenic Collage: Implications for continental growth and intracontinental deformation. Abstracts with programs for the 2nd workshop of IGCP Project-480 (Tomurhuu et al., Eds.). Institute of Geology and Mineral Recourses, Mongolian Academy of Sciences, Ulaanbaatar, Mongolia, 39-42.

Erdenesaihan, G., Ishiwatari, A., Orolmaa, D., Arai, S. and Tamura, A. (2013) Middle Paleozoic greenstones in the Hangay region, central Mongolia: Remnants of an accreted oceanic plateau and forearc magmatism. Journal of Mineralogical and Petrological Science, (XX), XX. (in press)

Filippova, I.B. (1969) The Khangay synclinorium: main features of structure and evolution. Geotektonika, 5, 76-78. (in Russian)

Fitton, J.G. and Godard, M. (2004) Origin and evolution of magmas on the Ontong Java Plateau, in Origin and evolution of the Ontong Java Plateau. Geological Society, Longon, Special Publications, 229, 151-178.

Fitton, J.G., Saunders, A.D., Norry, M.J., Hardarson, B.S. and Taylor, R.N. (1997) Thermal and chemical structure of the Iceland plume. Earth Planetary Science Letter, 153, 197-208.

Frey, F.A., Coffin, M., Wallace, P.J., Weis, D., Zhao, X., Wise, S.W., Wahnert, V., Teagle, D.A.H., Saccocia, P.J., Reusch, D.N., Pringle, M.S., Nicolaysen, K.E., Neal, C.R., Muller, R.D., Moore, C.L., Mahoney, J.J., Keszthelyi, L., Inokuchi, H., Duncan, R.A., Delius, H., Damuth, J.E., Damasceno, D., Coxall, H.K., Borre, M.K., Boehm, F., Barling, J., Arndt, N.T. and Antretter, M. (2000) Origin and evolution of a submarine large igneous province: the Kerguelen Plateau and Broken Ridge, southern Indian Ocean. Earth and Planetary Science Letters, 176 (1), 73-89.

Garcia, M.O., Swinnard, L., Weis, D., Greene, A.R., Tagami, T., Sano, H. and Gandy, C.E. (2010) Petrology, Geochemistry and Geochronology of Kaua'i Lavas over 4.5 Myr: Implications for the origin of rejuvenated volcanism and the evolution of the Hawaiian plume. Journal of Petrology, 51 (7), 1507-1540.

Gibson, S.A. (2002) Major element heterogeneity in Archean to recent mantle plume starting-heads. Earth and Planetary Science Letters, 195, 59-74.

Gibson, S.A., Thompson, R.N. and Dickin, A.P. (2000) Ferropicrites: geochemical evidence for Fe-rich streaks in upwelling mantle plumes. Earth and Planetary Science Letters, 174, 355-374.

Goldstein, S.B. and Francis, D. (2008) The petrogenesis and mantle source of Archean ferropicrites from the Western Superior Province, Ontario, Canada. Journal of Petrology, 49 (10), 1729-1753.

Griffiths, R.W. and Campbell, I.H. (1990) Stirring and structure in mantle starting plumes. Earth and Planetary Science Letters, 99, 66-78.

Hanski, E.J. (1992) Petrology of the Pechanga ferropicrites and cogenetic, Ni-bearing gabbro-wehrlite intrusions, Kola Peninsula, Russia. Bulletin, 367, pp.192, Geological Survey of Finland.

Hanski, E.J. and Smolkin, V.F. (1989) Pechenga Ferropicrites and Other Early Proterozoic Picrites in the Eastern Part of the Baltic Shield. Precambrian Research, 45, 63-82.

Hanski, E.J. and Smolkin, V.F. (1995) Iron- and LREE-enriched mantle source for early Proterozoic intraplate magmatism as exemplified by the Pechenga ferropicrites, Kola Peninsula, Russia. Lithos, 34, 107-125.

Hoang, N., Yamamoto, T., Itoh, J.I. and Flower, M.F.J. (2009) Anomalous intra-plate high-Mg andesites in the Choshi area (Chiba, Central Japan) produced during early stages of Japan Sea opening? Lithos, 112(3-4), 545-555.

Ichiyama, Y., Ishiwatari, A., Hirahara, Y. and Shuto, K. (2006) Geochemical and isotopic constraints on the genesis of the Permian ferropicritic rocks from the Mino–Tamba belt, SW Japan. Lithos, 89(1-2), 47-65.

Ichiyama, Y., Ishiwatari, A. and Koizumi, K. (2008) Petrogenesis of greenstones from the Mino-Tamba belt, SW Japan: Evidence for an accreted Permian oceanic plateau. Lithos, 100, 126-146.

Ichiyama, Y., Ishiwatari, A., Koizumi, K., Ishida, Y. and Machi, S. (2007) Olivine-spinifex basalt from the Tamba Belt, southwest Japan: Evidence for Fe- and high field strength element-rich ultramafic volcanism in Permian Ocean. Island Arc, 16, 493-503.

Ishiwatari, A., Yanagida, Y., Li, Y.-B., Ishii, T., Haraguchi, S., Koizumi, K., Ichiyama, Y. and Umeka, M. (2006) Dredge petrology of the boninite- and adakite-bearing Hahajima Seamount of the Ogasawara (Bonin) forearc: An ophiolite or a serpentinite seamount?. Island Arc 15(1), 102-118.

Izokh, A.E., Vishnevskii, A.V., Polyakov, G.V. and Shelepaev, R.A. (2011) Age of picrite and picrodolerite magmatism in western Mongolia. Russian Geology and Geophysics, 52(1), 7-23.

Jahn, B.-M. (2004) The Central Asian Orogenic Belt and growth of the continental crust in the Phanerozoic. In Aspects of the Tectonic Evolution of China (Malpas, J., Fletcher, C.J.N., Ali, J.R. and Aitchinson, J.C. Eds). Geological Society, London, Special Publications, 226, 73-100.

Jahn, B.-M., Wu, F. and Chen, B. (2000) Granitoids of the Central Asian Orogenic Belt and continental growth in the Phanerozoic. Transactions of the Royal Society of Edinburgh, Earth Sciences, 91, 181-193.

Kamei, A., Owada, M., Nagao, T. and Shiraki, K. (2004) High-Mg diorites derived from sanukitic HMA magmas, Kyushu Island, southwest Japan arc: evidence from clinopyroxene and whole rock compositions. Lithos, 75(3-4), 359-371.

Kamenetsky, V.S., Gurenko, A.A. and Kerr, A.C. (2010) Composition and temperature of komatiite melts from Gorgona Island, Colombia, constrained from olivine-hosted melt inclusions. Geology 38(11), 1003-1006.

Kelty, T.K., Yin, A., Dash, B., Gehrels, G.E. and Ribeiro, A.E. (2008) Detrital-zircon geochronology of Paleozoic sedimentary rocks in the Hangay-Hentey basin, north-central Mongolia: implications for the tectonic evolution of the Mongol-Okhotsk Ocean in central Asia. Tectonophysics, 451, 290-311.

Kerr, A.C. and Mahoney, J.J. (2007) Oceanic plateaus: Problematic plumes, potential paradigms. Chemical Geology, 241, 332-353.

Kerr, A. C., Tarney, J., Marriner, G. F., Klaver, G. T., Saunders, A. D. and Thirlwall, M. F. (1996) The geochemistry and petrogenesis of the late-Cretaceous picrites and basalts of Curacao, Netherlands Antilles: a remnant of an oceanic plateau. Contributions to Mineralogy and Petrology, 124, 29-43.

Kerr, A.C., White, R.V. and Saunders, A.D. (2000) LIP Reading: Recognizing oceanic plateaux in the geological record. Journal of Petrology, 41(7), 1041-1056.

Khain, E.V., Bibikova, E.V., Kroner, A., Zhuravlev, D.Z., Sklyarov, E.V., Fedotova, A.A. and Kravchenko-Berezhnoy, I.R. (2002) The most ancient ophiolite of the Central Asian fold belt: U-Pb and Pb-Pb zircon ages for the Dunzhugur Complex, Eastern Sayan, Siberia, and geodynamic implications. Earth and Planetary Science Letters, 199(3), 311-325.

Kovalenko, V.I., Yarmolyuk, V.V., Kovach, V.P., Kotov, A.B., Kozakov, I.K. and Sal'nikova, E.B. (1996) Sources of Phanerozoic granitoids in Central Asia: Sm-Nd isotope data. Geochemistry International, 34, 628-640.

Kovalenko, V.I., Yarmolyuk, V.V., Kovach, V.P., Kotov, A.B., Kozakov, I.K., Sal'nikova, E.B. and Larin, A.M. (2004) Isotope provinces, mechanisms of generation and sources of the continental crust in the Central Asian Mobile Belt: Geological and isotopic evidence. Journal of Asian Earth Sciences, 23, 605-627.

Kravchinsky, V. A., Konstantinov, K. M. and Cogne, J.P. (2001) Palaeomagnetic study of Vendian and Early Cambrian rocks of South Siberia and Central Mongolia: Was the Siberian platform assembled at this time? Precambrian Research, 110(1), 61-92.

Kurihara, T., Tsukada, K., Otoh, S., Kashiwagi, K., Minjin, C., Sersmaa, G., Dorjsuren, B., and Bujinlkham, B. (2006) Middle Paleozoic radiolarians from the Gorkhi Formation, Central Mongolia. In Structural and tectonic correlation across the Central Asian Orogenic Collage: Implications for continental growth and intracontinental deformation. Abstracts with programs for the 2nd workshop of IGCP Project-480 (Tomurhuu et al., Eds.). Institute of Geology and Mineral Recourses, Mongolian Academy of Sciences, Ulaanbaatar, Mongolia, 67.

Kurihara, T., Tsukada, K., Otoh, S., Kashiwagi, K., Chuluun, M., Byambadash, D., Boijir, B., Gonchigdorj, S., Nuramkhan, M., Niwa, M., Tokiwa, T., Hikichi, G. and Kozuka, T. (2009) Upper

Silurian and Devonian pelagic deep-water radiolarian chert from the Khangai–Khentei belt of Central Mongolia: Evidence for Middle Paleozoic subduction–accretion activity in the Central Asian Orogenic Belt. Journal of Asian Earth Sciences, 34(2), 209-225.

Kurimoto, Ch., Ichinnorov, N., Koike, T., Tungalag, F., Bayarmandal, L. (1997) The discovery of Late Devonian (Famenian) conodonts in the Bayanhongor area. Bulletin of the Geological Survey of Japan, 48(9), 487-491.

Lassiter, J.C. and DePaolo, D.J. (1997) Plume/lithosphere interaction in the generation of continental and oceanic flood basalts: Chemical and isotopic constraints. In large igneous provinces: Continental, oceanic, and planetary flood volcanism (Mahoney, J.J. and Coffin, M.F. Eds). American Geophysical Union, Washington, D.C, 335-355.

Le Bas, M.J. (2000) IUGS Reclassification of the high-Mg and Picritic volcanic rocks. Journal of Petrology, 41(10), 1467-1470.

Leterrier, J., Maury, R.C., Thonon, P., Girard, D. and Marchal, M. (1982) Clinopyroxene composition as a method of identification of the magmatic affinities of paleo-volcanic series. Earth and Planetary Science Letters, 59(1), 139-154.

Lhundev, Sh., Tomurchudur, Ch., Purevdorj, Z., Baaday, D., Unurjav, L. and Ganbold, Yu. (1994) Geology and Mineral resources of the Uyanga area 1:50 000. Geological mapping and prospecting report 4756, pp, 619, Ulaanbaatar, Mongolia. (in Mongolian)

Li, Y.-B., Kimura, J.-I., Machida, S., Ishii, T., Ishiwatari, A., Maruyama, S., Qiu, H.-N., Ishikawa, T., Kato, Y., Haraguchi, S., Takahata, N., Hirahara, Y, and Miyazaki, T. (2013) High-Mg adakite and Low-Ca boninite from a Bonin fore-arc seamount: Implications for the reaction between slab melts and depleted mantle. Journal of Petrology, 54(6), 1149-1175.

Longerich, H.P., Jackson, S.E. and Gunther, D. (1996) Inter-laboratory note. Laser ablation inductively coupled plasma mass spectrometric transient signal data acquisition and analyte concentration calculation. Journal of Analytical Atomic Spectrometry, 11(9), 899-904.

Ludden, J.N. and Thompson, G. (1978) Behaviour of rare earth elements during submarine weathering of tholeiitic basalt. Nature, 274(5667), 147-149.

MacDonald, G.A. and Katsura, T. (1964) Geochimical composition of Hawaiian lavas. Journal of Petrology, 5, 82-133

MacKenzie, W.S., Donaldson, C.H. and Guilford, C. (1982) Atlas of igneous rocks and their textures. pp.148, Longman Group Ltd, UK.

Maruyama, S., Santosh, M. and Zhao, D. (2007) Superplume, supercontinent, and post-perovskite: Mantle dynamics and anti-plate tectonics on the core–mantle boundary. Gondwana Research, 11(1-2), 7-37.

Miyashiro, A. (1974) Volcanic Rock Series in Island Arcs and Active Continental Margins. American Journal of Science 274(4), 321-355.

Morimoto, N., Fabries, J., Ferguson, A.K., Ginzburg, I.V., Ross, M., Seifert, F.A., Zussman, J., Aoki, K. and Gottardi, G. (1988) Nomenclature of pyroxenes. American Mineralogist, 73(9-10), 1123-1133.

Morishita, T., Ishida, Y., Arai, S. and Shirasaka, M. (2005) Determination of multiple trace element compositions in thin (> 30 μm) layers of NIST SRM 614 and 616 using laser ablation-inductively coupled plasma-mass spectrometry (LA-ICP-MS). Geostandards and Geoanalytical Research, 29(1), 107-122.

Mossakovsky, A.A., Ruzhentsev, S.V., Samygin, S.G. and Kheraskova, T.N. (1994) Central Asian fold belt: Geodynamic evolution and history of formation. Geotectonics, 27, 445-474.

Neal, C.R., Mahoney, J.J. and Chazey, W.J. (2002) Mantle sources and the highly variable role of continental lithosphere in basalt petrogenesis of the Kerguelen Plateau and Broken Ridge LIP: Results from ODP Leg 183. Journal of Petrology 43(7), 1177-1205.

Nicholls, J. and Stout, M.Z. (1988) Picritic melts in Kilauea: Evidence from the 1967-1968 Halemaumau and Hiiaka eruptions. Journal of Petrology, 29(5), 1031-1057.

Norman, M.D. and Garcia, M.O. (1999) Primitive magmas and source characteristics of the Hawaiian plume: petrology and geochemistry of shield picrites. Earth and Planetary Science Letters 168(1-2), 27-44.

Orolmaa, D. and Erdenesaihan, G. (2008) Geology and geochemistry of Devonian basalts in the Hangay region. Geological Institute Transaction, 18, 50-60. (in Mongolian)

Orolmaa, D., Erdenesaihan, G., Borisenko, A.S., Fedoseev, G.S., Babich, V.V. and Zhmodik, S.M. (2008) Permian-Triassic granitoid magmatism and metallogeny of the Hangayn (central Mongolia). Russian Geology and Geophysics, 49(7), 534-544.

Orolmaa, D., Munkhbayar, S., Erdenesaihan, G. and Odgerel, D. (2010) Geochemistry of the Early Mesozoic granitoids of the Hangay-Hentey Fold Belt. Geological Institute Transaction, 20, 52-64. (in Mongolian)

Osozawa, S., Tsolmon, G., Majigsuren, U., Sereenen, J., Niitsuma, S., Iwata, N., Pavlis, T. and Jahn, B.M. (2008) Structural evolution of the Bayanhongor region, west-central Mongolia. Journal of Asian Earth Sciences, 33, 337-352.

Oyunchimeg, T., Izokh, A.E., Vishnevsky, A.V. and Kalugin, V.M. (2009) Isoferroplatinum mineral assemblage from the Burgastain Gol placer (Western Mongolia). Russian Geology and Geophysics, 50(10), 863-872.

Pearce, N.J.G., Perkins, W.T., Westgate, J.A., Gorton, M.P., Jackson, S.E., Neal, C.R. and Chenery, S.P. (1997) A compilation of new and published major and trace element data for NIST SRM 610 and NIST SRM 612 glass reference materials. Geostandards Newsletter, 21(1), 115-144.

Pearce, J.A. (1996) A user's guide to basalt discrimination diagrams. (Wyman, D.A. Ed.). Trace element geochemistry of volcanic rocks: Applications for massive sulphide exploration. Short Courses Notes, vol. 12, Geological Association of Canada, 79–113.

Purevjav, N. and Roser, B. (2012) Geochemistry of Devonian–Carboniferous clastic sediments of the Tsetserleg terrane, Hangay Basin, Central Mongolia: Provenance, source weathering, and tectonic setting. Island Arc, 21(4), 270-287.

Purevjav, N. and Roser, B. (2013) Geochemistry of Tsetserleg terrane (Mongolia) sandstone and mudrocks: Evaluation of grain size effect in immature volcanolithic arc sediments. Earth Science (Chikyu Kagaku), 67, 63-74.

Regelous, M., Hofmann, A.W., Abouchami, W. and Galer, S.J.G. (2003) Geochemistry of lavas from the Emperior seamounts, and the geochemical evolution of Hawaiian Magmatism from 85 to 42 Ma. Journal of Petrology, 44 (1), 113-140.

Révillon, S., Arndt, N.T., Hallot, E., Kerr, A.C. and Tarney, J. (1999) Petrogenesis of picrites from the Caribbean Plateau and the North Atlantic magmatic province. Lithos 49(1-4), 1-21.

Rogers, G. and Saunders, A.D. (1989) Magnesian andesites from Mexico, Chile and the Aleutian Islands: implications for magmatism associated with ridge-trench collision. In Boninites and related Rocks (Crawford, A.J. Ed.). Unwin Hyman, London, 416–445.

Rogers, G., Saunders, A.D., Terrell, D.J., Verma, S.P. and Marriner,G.F. (1985) Geochemistry of Holocene volcanic rocks associated with ridge subduction in Baja California, Mexico. Nature, 315, 389-392.

Safonova, I.Y., Utsunomiya, A., Kojima, S., Nakae, S., Tomurtogoo, O., Filippov, A.N. and Koizumi, K. (2009) Pacific superplume-related oceanic basalts hosted by accretionary complexes of Central Asia, Russian Far East and Japan. Gondwana Research, 16(3-4), 587-608.

Safonova, I.Y. and Santosh, M. (2012) Accretionary complexes in the Asia-Pacific region: Tracing archives of ocean plate stratigraphy and tracking mantle plumes. Gondwana Research, http://dx.doi.org/10.1016/j.gr.2012.10.008 (in press)

Sano, T., Shimizu, K., Ishikawa, A., Senda, R., Chang, Q., Kimura, J.-I., Widdowson, M. and Sager, W.W. (2012) Variety and origin of magmas on Shatsky Rise, northwest Pacific Ocean. Geochemistry, Geophysics, Geosystems, 13(8), Q08010, doi:10.1029/2012GC004235.

Şengör, A.M.C., Natal'in, B.A. and Burtman, V.S. (1993) Evolution of the Altaid tectonic collage and Paleozoic crustal growth in Eurasia. Nature, 364(6435), 299-307.

Şengör, A.M.C. and Natal'in, B.A. (1996) Paleotectonics of Asia: Fragments of synthesis. In The tectonic evolution of Asia (Yin, A. and Harrison, M. EDs.). pp. 486-641, Cambridge University Press.

Shimoda, G., Tatsumi, Y., Nohda, S., Ishizaka, K. and Jahn, B.M. (1998) Setouchi high-Mg andesites revisited: Geochemical evidence for melting of subducting sediments. Earth and Planetary Science Letters, 160(3-4), 479-492.

Shkol'nik, S.I., Belichenko, V.G. and Reznitskii, L.Z. (2013) High-magnesium picrite–basalt associations of the Tunka terrane (Baikal–Hövsgöl region) as an indicator of the back-arc basin spreading. Russian Geology and Geophysics, 54(2), 153-165.

Sigurdsson, H. and Schilling, J.G. (1976) Spinels in Mid-Atlantic Ridge basalts: Chemistry and occurrence. Earth and Planetary Science Letters, 29(1), 7-20.

Sobolev, A.V. and Danyushevsky, L.V. (1994) Petrology and geochemistry of boninites from the north termination of the Tonga trench: Constraints on the generation conditions of primary high-Ca boninite magmas. Journal of Petrology, 35(5), 1183-1211.

Staudigel, H. and Clague, D.A. (2010) The geological history of deep-Sea volcanoes biosphere, hydrosphere, and lithosphere interactions. Oceanography, 23, 58-71.

Sun, S.-S. and McDonough, W.F. (1989) Chemical and isotopic systematics of oceanic basalts: implications for mantle composition and processes. Geological Society, London, Special Publications, 42(1), 313-345.

Tatsumi, Y., Ishikawa, N., Anno, K., Ishizaka, K. and Itaya, T. (2001) Tectonic setting of high-Mg andesite magmatism in the SW Japan arc: K-Ar chronolgy of the Setouchi volcanic belt. Geophysical Journal International, 144 (3), 625-631.

Tatsumi, Y. and Ishizaka, K. (1981) Existence of andesitic primary magma: An example from southwest Japan. Earth and Planetary Science Letters, 53(1), 124-130.

Tatsumi, Y. and Ishizaka, K. (1982) Magnesian andesite and basalt from Shodo-Shima island, southwest Japan, and their bearing on the genesis of calc-alkaline andesites. Lithos, 15(2), 161-172.

Tatsumi, Y., Shukuno, H., Sato, K., Shibata, T. and Yoshikawa, M. (2003) The petrology and geochemistry of high-magnesium andesites at the western tip of the Setouchi volcanic belt, SW Japan. Journal of Petrology, 44(9), 1561-1578.

Tatsumi, Y., Suzuki, T., Kawabata, H., Sato, K., Miyazaki, T., Chang, Q., Takahashi, T., Tani, K., Shibata, T. and Yoshikawa, M. (2006) The petrology and geochemistry of Oto-Zan composite lava flow on Shodo-Shima island, SW Japan: Remelting of a solidified high-Mg andesite magma. Journal of Petrology, 47(3), 595-629.

Tejada, M.L.G., Mahoney, J.J., Duchan, R.A. and Hawkins, M.P. (1996) Age and geochemistry of basement and alkalic rocks of Malaita and Santa Isabel, Solomon islands, southern margin of Ontong Java Plateau. Journal of Petrology, 37(2), 361-394.

Tejada, M.L.G., Mahoney, J.J., Neal, C.R., Duncan, R.A. and Petterson, M.G. (2002) Basement geochemistry and geochronology of Central Malaita, Solomon Islands, with implications for the origin and evolution of the Ontong Java Plateau. Jourbal of Petrolology, 43, 449-484.

Teraoka, Y., Suzuki, M., Tungalag, F., Ichinnorov, N. and Sakamaki, Y. (1996) Tectonic framework of the Bayanhongor area, west Mongolia. Bulletin of the Geological Survey of Japan, 47, 447-455.

Tomurtogoo, O. (2002) Tectonic map of Mongolia at the scale of 1:1,000,000, and tectonics of Mongolia (Explanatory notes of the map). Mineral Resources Authority of Mongolia, Ulaanbaatar.

Tomurtogoo, O. (2006) Tectonics and geodynamics of Mongolia. Mongolian science: Geological science, 53, 213-271.

Tomurtogoo, O. (2012) Tectonic subdivision of Mongolian Orogenic Belts. Geological Institute Transaction, 21, 5-25. (in Mongolian)

Tomurtogoo, O., Windley, B.F., Kröner, A., Badarch, G. and Liu, D.Y. (2005) Zircon age and occurrence of the Adaatsag ophiolite and Muron shear zone, central Mongolia: constraints on the evolution of the Mongol–Okhotsk ocean, suture and orogen. Journal of the Geological Society 162(1), 125-134.

Tsukada, K., Kurihara, T., Niwa, K., Otoh, S., Hikichi, G. y., Kashiwagi, K., Kozuka, T., Chuluun, M., Dorjsuren, B., Gonchigdorj, S. and Bujinlkham, B. (2006) Geochemical feature of basalt from the Gorkhi Formation, Khangay-Khentey belt, Central Mongolia. In Structural and tectonic correlation across the Central Asian Orogenic Collage: Implications for continental growth and intracontinental deformation. Abstracts with programs for the 2nd workshop of IGCP Project-480 (Tomurhuu et al., Eds.). Institute of Geology and Mineral Recourses, Mongolian Academy of Sciences, Ulaanbaatar, Mongolia, 82-83.

Tsukada, K., Nakane, Y., Yamamoto, K., Kurihara, T., Otoh, S., Kashiwagi, K., Chuluun, M., Gonchigdorj, S., Nuramkhaan, M., Niwa, M. and Tokiwa, T. (2013) Geological setting of basaltic rocks in an accretionary complex, Khangai-Khentei Belt, Mongolia. Island Arc, 22, 227-241.

Tuff, J., Takahashi, E. and Gibson, S.A. (2005) Experimental constraints on the role of garnet pyroxenite in the genesis of high-Fe mantle plume derived melts. Journal of Petrology, 46 (10), 2023-2058.

Wilhem, C., Windley, B.F. and Stampfli, G.M. (2012) The Altaids of Central Asia: A tectonic evolutionary innovative review. Earth-Science Reviews, 133, 303-341.

Wilkinson, J.F.G. and Hensel, H.D. (1988) The petrology of some picrites from Mauna Loa and Kilauea volcanoes, Hawaii. Contributions to Mineralogy and Petrology, 98(3), 326-345.

Winchester, J.A. and Floyd, P.A. (1977) Geochemical Discrimination of Different Magma Series and Their Differentiation Products Using Immobile Elements. Chemical Geology, 20(4), 325-343.

Windley, B.F., Alexeiev, D., Xiao, W.J., Kroner, A. and Badarch, G. (2007) Tectonic models for accretion of the Central Asian Orogenic Belt. Journal of the Geological Society, 164, 31-47.

Xiao, W.J., Han, C.M., Yuan, C., Sun, M., Lin, S.F., Chen, H.L., Li, Z.L., Li, J.L. and Sun, S. (2008) Middle Cambrian to Permian subduction-related accretionary orogenesis of Northern Xinjiang,

NW China: Implications for the tectonic evolution of Central Asia. Journal of Asian Earth Sciences, 32(2-4), 102-117.

Yakubchuk, A. (2004) Architecture and mineral deposit settings of the Altaid Orogenic Collage: A revised model. Journal of Asian Earth Sciences, 23(5), 761-779.

Yogodzinski, G.M., Kay, R.W., Volynets, O.N., Koloskov, A.V. and Kay, S.M., 1995. Magnesian andesite in the western Aleutian Komandorsky region: implications for slab melting and processes in the mantle wedge. Geological Society of America, Bulletin, 107, 505- 519.

Zonenshain, L.P. (1973) The evolution of Central Asiatic geosynclines through sea-floor spreading. Tectonophysics 19(3), 213-232.

Zonenshain, L.P., Kuz'min, M.I., Natapov, L.M., Page, B.M. and AGU Geophysical Monograph Board. (1990) Geology of the USSR: A plate-tectonic synthesis. Geodymanics Series, 21, pp.242. American Geophysical Union, Washington, D.C.

Zorin, Y.A. (1999) Geodynamics of the western part of the Mongolia–Okhotsk collisional belt, Trans-Baikal region (Russia) and Mongolia. Tectonophysics, 306(1), 33-56.

TABLES

Table 1. Sample locations and analyze lists.

Sample No	Rock type	Latitude	Longitude	Thin section	EDS			XRF	LA-ICP-MS
					Cpx	Spl	Amp		
01	Highly porphyric basalt dyke	46°30'50.4"°	102°19'19.7"	●	●	●		●	
02	Microdolerite	46°31'22.7	102°18'59.0"	●	●			●	●
03	Dolerite	46°31'25.7"	102°19'00.4"	●					
04	Dolerite	46°32'17"	102°18'45.4"	●					
05	Volcanic tuff	46°30'28.8"	102°19'42.4"	●					
06	Basalt	46°30'47.6"	102°19'18.9"	●					
07	Basalt	46°30'34.1"	102°19'47.6"	●	●				
08	Basalt	46°30'47.6"	102°19'18.9"	●					
09	Dolerite	46°30'34.2"	102°19'52.3"	●					
11	Dolerite dyke	46°30'35.2"	102°19'49.3"	●	●			●	●
12	Picrite	46°30'46.6"	102°19'10.1"	●	●	●		●	●
13	Basalt	46°30'44.4"	102°19'02.2"	●					
14	Microdolerite	46°22'06.7"°	102°28'54.8"	●	●			●	●
15	Dolerite	46°24'34.1"	102°20'40.2"	●	●				
16	Vesicular basalt	46°24'33.5"	102°20'59.5"	●					
28	Hyaloclastite	46°35'45.3"	102°13'19.0"	●	●				
29	Basalt	46°35'43.5"	102°13'28.5"	●		●			
30A	Picrite	46°35'44.2"	102°13'28.5"	●				●	●
30B	Volcanic tuff	46°35'44.2"	102°13'28.5"	●					
31	Ferropicrite	46°35'43.1	102°13'27.1"	●		●		●	●
32	Ferropicrite	46°35'43.1	102°13'27.1"	●		●		●	●
34	Basalt	46°36'30.0"	102°13'16.5	●		●			
35A	Aphyric basalt	46°32'50.6	102°15'15.0"	●				●	●
35B	Aphyric basalt	46°31'12.2"	102°19'52.0"	●				●	●
36	Vesicular basalt	46°13'15.2"	102°19'47.0"	●	●			●	●
37	Hyaloslastite	46°30'47.5"	102°19'15.7"	●		●			
38	Highly porphyric basalt dyke	46°30'47.5"	102°19'15.7"	●				●	●
40	Basalt dyke	46°30'47.5"	102°19'15.7"	●					
41	Andesite sill	46°31'13.3"	102°21'07.0"	●	●	●	●	●	●
42	Andesite	46°29'17.0"	102°23'37.8"	●	●	●		●	●
43A	Aphyric ferrobasalt	46°29'44.2"	102°24'48.6"	●				●	●
43B	Aphyric ferrobasalt	46°29'44.2"	102°24'48.6"	●				●	●
2602A	Basalt	46°35'43.0	102°13'27.1"	●				●	●
2602B	Picrite	46°35'43.1	102°13'27.1"	●		●		●	●
2701-1	Metabasalt	46°30'35.2"	102°19'49.3"	●	●	●			
2701-2	Metabasalt	46°30'35.2"	102°19'49.3"	●	●	●			
2703	Aphyric ferrobasalt	46°29'44.2"	102°24'48.6"	●				●	●

Table 2. XRF analyses for the whole rock major (wt%) and some trace elements and LA-ICP-MS analyses of trace elements data (ppm) for greenstones from the Hangay region.

Rock	Ferropicrite		Picrite			Dolerite			Basalt
Occurrence	Lava	Lava	Cobble	Lava	Lava	Lava	Lava	Dyke	Lava
Location	BU	BU	ULT	BU	BU	ULT	HZT	ULT	BU
Sample	#32	#31	#12	#30	#2602B	#02	#14	#11	#2602A
SiO_2	43.38	47.13	46.60	46.48	45.56	48.74	49.73	51.45	47.47
TiO_2	1.18	1.30	1.57	2.19	1.64	2.21	1.78	1.89	1.85
Al_2O_3	8.62	9.74	12.75	11.52	10.36	15.29	14.51	20.17	13.33
Fe_2O_3T	15.14	15.62	12.85	13.72	14.05	11.18	12.07	9.80	13.39
MnO	0.17	0.15	0.19	0.17	0.21	0.19	0.18	0.50	0.21
MgO	21.52	16.74	11.81	10.94	16.04	6.87	6.87	7.26	8.54
CaO	7.14	4.43	9.27	7.52	7.70	9.26	7.58	7.76	6.85
Na_2O	n.d.	n.d.	1.56	1.13	1.32	4.02	4.01	3.91	2.77
K_2O	n.d.	n.d.	0.22	n.d.	0.15	0.28	0.73	1.15	0.06
P_2O_5	0.12	0.16	0.16	0.28	0.17	0.19	0.12	0.32	0.22
Total	97.27	95.27	96.98	93.95	97.20	98.23	97.59	104.22	94.67
Rb	0.13	0.19	2.94	0.29	1.36	3.79	12.0	30.0	2.13
	*1.30	*0.80	*4.10	*1.50	*1.50	*4.45	*14.1	*35.7	*2.60
Ba	5.80	8.91	130	94	53	197	122	892	96
	*2.50	*12.4	*118	*108	*54	*215	*127	*944	*102
V	225	232	296	300	274	329	404	279	321
	*160	*176	*255	*256	*227	*282	*366	*247	*280
Cr	2173	2550	813	615	1240	305	276	112	590
	*1801	*1754	*1125	*499	*1140	*238	*214	*83	*455
Ni	1306	1514	418	304	724	79	113	39	97
	*1491	*1620	*493	*332	*821	*85	*129	*37	*99
Y	12	12	18	26	21	24	27	22	17
	*13	*12	*16	*23	*20	*25	*27	*23	*17
Zr	67	76	95	156	112	134	104	117	122
	*70	*76	*99	*144	*101	*142	*104	*127	*117
Nb	7.3	8.5	10	17	11	14	6.4	12	14
	*6.8	*7.4	*8.2	*11	*8.8	*11	*5.9	*9.2	*11
Sr	12	132	281	550	107	722	441	1160	574
	*13	*126	*262	*473	*97	*670	*412	*1057	*504
Co	102	108	68	51	87	36	44	30	37
Th	0.51	0.54	0.66	1.26	0.76	1.01	0.50	0.83	0.94
Ta	0.48	0.54	0.74	1.10	0.67	0.99	0.46	0.79	0.91
La	5.60	6.17	8.34	12.57	8.22	11.6	5.73	9.15	11.0
Ce	13.0	14.0	20.0	28.0	19.0	27.0	15.0	21.0	23.0
Pr	1.88	2.01	2.77	4.12	2.85	3.87	2.40	3.18	3.21
Nd	9.16	9.37	14.0	20.0	14.0	19.0	13.0	15.0	16.0
Hf	1.76	1.86	2.45	3.93	2.91	3.35	2.91	3.05	3.05
Sm	2.39	2.53	3.57	5.49	3.87	4.98	3.91	4.21	3.74
Eu	0.82	0.80	1.45	1.83	1.33	1.80	1.33	1.58	1.35
Gd	2.59	2.80	3.74	5.74	4.43	5.33	4.89	4.68	4.01
Tb	0.38	0.43	0.58	0.83	0.66	0.78	0.80	0.72	0.61
Dy	2.41	2.64	3.73	5.36	4.33	5.02	5.46	4.58	3.66
Ho	0.47	0.50	0.74	1.03	0.78	0.94	1.10	0.87	0.72
Er	1.21	1.27	1.90	2.64	2.20	2.48	3.08	2.42	1.92
Tm	0.17	0.17	0.26	0.35	0.30	0.35	0.46	0.35	0.29
Yb	1.06	1.00	1.82	2.25	1.95	2.20	3.02	2.13	1.79
Lu	0.14	0.14	0.24	0.32	0.27	0.31	0.45	0.30	0.26

Locality abbreviations: ULT-Uvur Ult valley, BU-Buuruljuut valley, TSE-Tsetsengiin valley. SUV-Suvraga mountain pass, HZT-Harzat mountain pass. *-XRF analysis result. T-total Fe as Fe_2O_3. n.d.-not detected.

Table 2. (Continued)

Rock	Basalt					Ferrobasalt			High-Mg andesite	
Occurrence	Lava	Lava	Lava	Dyke	Dyke	Lava	Lava	Lava	Sill	Lava
Location	ULT	TSE	TSE	ULT	ULT	TSE	TSE	TSE	TSE	TSE
Sample	#36	#35A	#35B	#38	#01	#43A	#43B	#2703	#41	#42
SiO_2	45.75	45.01	49.01	46.28	46.23	44.76	47.13	42.58	58.26	53.35
TiO_2	2.18	3.41	3.53	1.80	1.97	4.65	3.94	5.36	0.70	0.96
AI_2O_3	14.58	14.78	15.35	19.91	16.45	13.10	14.64	15.15	15.42	14.72
Fe_2O_3T	11.83	15.19	11.52	10.12	11.44	16.31	18.82	15.90	6.76	8.12
MnO	0.39	1.40	0.33	0.33	0.19	0.60	0.33	0.79	0.09	0.12
MgO	5.46	7.13	4.38	6.04	8.61	8.96	6.45	8.42	4.40	6.75
CaO	9.92	5.47	5.89	5.94	8.96	4.98	4.77	5.24	3.83	7.30
Na_2O	4.42	3.08	3.75	3.29	2.49	1.82	2.85	2.30	4.18	3.43
K_2O	0.59	0.67	2.58	2.35	0.43	1.35	0.51	1.23	4.13	1.74
P_2O_5	0.32	0.60	0.52	0.20	0.16	0.65	1.94	0.71	0.17	0.21
Total	95.46	96.74	96.86	96.26	96.93	97.16	101.37	97.68	97.93	96.70
Rb	5.23	11.9	56.2	37.5		7.67	10. 2	23.2	101	32.0
	*7.10	*13.9	*60.8	*43.8	*8.10	*9.10	*13.1	*26.0	*117	*37.1
Ba	661	341	856	479		328	612	349	964	327
	*624	*355	*847	*484	*256	*644	*377	*403	*950	*309
V	356	502	502	317		216	374	406	232	278
	*298	*490	*496	*247	*247	*381	*209	*437	*145	*200
Cr	146	25	28	158		77	3.14	106	200	299
	*109	*14	*14	*118	*338	*12	*2.30	n.d.	*198	*269
Ni	54	33	42	53		14	58	72	45	74
	*50	*25	*38	*53	*97	*50	*4.80	*69	*46	*79
Y	28	68	56	23		31	67	39	20	20
	*28	*63	*54	*24	*23	*30	*66	*39	*20	*19
Zr	154	286	288	121		259	494	290	175	148
	*156	*253	*268	*123	*129	*245	*459	*275	*176	*139
Nb	17	24	25	13		36	67	42	6.5	5.8
	*12	*17	*17	*10	*11	*24	*41	*27	*5.9	*5.7
Sr	457	195	198	311		475	236	280	641	455
	*416	*176	*183	*301	*336	*224	*447	*266	*622	*413
Co	34	45	58	47		26	39	49	16	24
Th	1.20	1.65	1.73	0.81		4.42	2.24	2.45	9.04	5.82
Ta	1.16	1.61	1.55	0.82		4.22	2.42	2.80	0.48	0.40
La	15	18	19	11		59	25	29	27	27
Ce	33	44	45	24		124	55	63	52	52
Pr	4.63	6.59	6.75	3.41		17.0	7.37	8.58	6.18	6.74
Nd	22	34	34	17		81	35	39.0	25.0	28
Hf	3.96	7.18	7.22	3.14		12.0	6.36	6.86	4.68	3.88
Sm	5.70	9.67	9.53	4.14		19.0	8.28	10.0	5.05	5.65
Eu	2.07	3.32	3.16	1.74		6.36	2.77	3.13	1.19	1.51
Gd	6.29	12.0	11.0	4.74		19.0	8.32	9.42	4.57	4.80
Tb	0.90	1.91	1.70	0.67		2.63	1.11	1.38	0.60	0.64
Dy	5.76	13.0	11.0	4.19		16.0	6.84	8.30	3.96	3.88
Ho	1.10	2.59	2.26	0.78		2.75	1.26	1.50	0.75	0.74
Er	2.89	7.31	6.06	2.04		6.90	3.10	3.89	2.11	2.04
Tm	0.40	0.99	0.86	0.26		0.91	0.41	0.51	0.32	0.28
Yb	2.58	6.89	5.74	1.55		5.74	2.66	3.33	2.09	2.02
Lu	0.35	0.96	0.79	0.21		0.74	0.37	0.46	0.31	0.29

Table 3. Representative microprobe analyses (wt%) of clinopyroxene, hornblende, and spinel in greenstones from the Hangay region. The ferric iron content of spinel was estimated assuming spinel stoichiometry.

Rock	Basalt						Dolerite						Porphyric basalt					
Sample	#01						#02						#07					
Mineral	core	rim	core	rim	core	rim	core	rim	core	rim	core	rim	core	rim	core	rim	core	rim
SiO2	52.07	50.97	51.95	51.21	51.51	49.35	52.64	49.65	52.49	51.96	52.52	52.41	52.77	51.00	53.32	50.68	52.55	49.95
TiO2	0.59	0.52	0.60	0.76	0.59	1.19	0.70	1.75	0.66	0.67	0.64	0.81	0.78	0.99	0.67	1.35	0.81	1.53
Al2O3	2.81	2.61	2.65	3.06	2.45	2.47	2.98	3.03	2.37	2.96	2.19	2.69	2.42	2.02	2.01	2.75	2.64	3.06
Cr2O3	0.99	0.92	0.84	1.01	0.51	0.06	0.92	0.06	0.50	0.83	0.47	0.20	0.52	0.03	0.30	0.07	0.40	0.04
FeO	5.46	5.05	5.30	5.98	5.72	14.40	5.18	12.83	5.74	5.26	5.68	6.68	6.82	16.02	7.26	12.52	6.67	12.12
MnO	0.06		0.04		0.24	0.30	0.00	0.34	0.13	0.14	0.06	0.19	0.14	0.51	0.15	0.28	0.20	0.22
MgO	17.07	16.43	16.83	16.29	16.77	12.39	16.99	13.80	16.99	16.74	17.17	16.52	16.54	12.28	16.88	13.09	16.56	13.26
CaO	20.55	20.33	20.56	20.56	19.91	17.36	20.92	17.85	20.88	20.69	20.78	20.51	20.56	17.31	20.12	19.10	20.57	19.58
Na2O		0.01		0.03			0.09	0.20	0.10	0.14	0.13	0.10	0.10	0.38	0.14	0.36	0.29	0.34
Total	99.60	96.85	98.77	98.90	97.71	97.51	100.41	99.52	99.85	99.39	99.63	100.10	100.64	100.53	100.84	100.21	100.71	100.09
O=	6	6	6	6	6	6	6	6	6	6	6	6	6	6	6	6	6	6
Si	1.914	1.924	1.923	1.902	1.930	1.919	1.916	1.882	1.927	1.914	1.931	1.924	1.928	1.935	1.944	1.908	1.920	1.884
Ti	0.016	0.015	0.017	0.021	0.017	0.035	0.019	0.050	0.018	0.018	0.018	0.022	0.021	0.028	0.018	0.038	0.022	0.043
Al	0.122	0.116	0.116	0.134	0.108	0.113	0.128	0.135	0.103	0.129	0.095	0.116	0.104	0.090	0.086	0.122	0.114	0.136
Cr	0.029	0.027	0.025	0.030	0.015	0.002	0.026	0.002	0.014	0.024	0.014	0.006	0.015	0.001	0.009	0.002	0.012	0.001
Fe^{2+}	0.168	0.160	0.164	0.186	0.179	0.469	0.158	0.407	0.176	0.162	0.174	0.205	0.208	0.508	0.221	0.394	0.204	0.382
Mn	0.002	0.000	0.001	0.000	0.008	0.010	0.000	0.011	0.004	0.004	0.002	0.006	0.004	0.016	0.005	0.009	0.006	0.007
Mg	0.935	0.925	0.929	0.902	0.936	0.718	0.922	0.780	0.930	0.919	0.941	0.904	0.901	0.694	0.917	0.734	0.902	0.745
Ca	0.809	0.822	0.815	0.818	0.799	0.723	0.816	0.725	0.821	0.816	0.818	0.807	0.805	0.704	0.786	0.770	0.805	0.791
Na		0.001		0.002			0.006	0.015	0.007	0.010	0.009	0.007	0.007	0.028	0.010	0.027	0.021	0.025
Total	3.995	3.990	3.990	3.996	3.992	3.989	3.991	4.007	4.000	3.996	4.002	3.997	3.994	4.005	3.995	4.005	4.005	4.016
Mg#	0.848	0.853	0.850	0.829	0.839	0.605	0.854	0.657	0.841	0.850	0.844	0.815	0.812	0.577	0.806	0.651	0.816	0.661

FeO* is total iron as FeO.

Table 3. (Continued).

Rock	Porphyric basalt						Picrite						Microdolerite (groundmass Cpx)					
Sample	#11						#12						#14					
Mineral	core	rim	core	rim	core	rim	core	rim	core	rim	core	rim	core-gm	rim-gm	core-gm	rim-gm	core-gm	rim-gm
SiO2	50.99	48.61	50.57	49.43	48.93	47.39	52.47	51.05	52.12	49.97	51.66	50.98	51.70	50.62	50.25	50.25	50.99	50.43
TiO2	0.69	1.23	0.65	0.78	0.74	1.24	0.57	0.93	0.52	1.32	0.60	1.04	0.59	0.68	0.74	0.91	0.51	0.63
Al2O3	2.39	2.95	1.88	1.47	2.23	2.61	2.43	1.85	2.59	2.34	2.68	1.44	1.59	1.45	3.31	3.71	2.65	2.93
Cr2O3	0.35	0.18	0.11	0.11	0.20	0.04	0.54	0.00	0.89	0.09	0.87	0.03	0.08	0.00	0.46	0.17	0.72	1.03
FeO	6.52	9.21	7.05	9.27	6.90	9.60	5.93	15.62	5.32	12.82	5.47	12.86	9.22	11.35	6.17	7.47	5.34	5.33
MnO	0.12	0.19	0.13	0.17	0.19	0.21	0.10	0.40	0.03	0.27	0.14	0.38	0.23	0.32	0.21	0.18	0.14	0.10
MgO	16.04	14.02	15.94	14.75	14.93	13.49	16.93	13.31	16.89	13.16	16.57	14.27	16.67	15.30	15.46	15.74	15.88	15.70
CaO	20.21	19.27	19.04	18.22	19.71	18.33	20.64	16.12	20.69	17.94	20.17	16.96	17.18	16.32	20.46	19.03	21.22	21.11
Na2O	0.19	0.29	0.19	0.17	0.27	0.22			0.15	0.32	0.09	0.22			0.07	0.19	0.05	0.08
Total	97.50	95.94	95.55	94.36	94.10	93.12	99.62	99.29	99.18	98.23	98.25	98.18	97.26	96.03	97.13	97.66	97.52	97.34
O=	6	6	6	6	6	6	6	6	6	6	6	6	6	6	6	6	6	6
Si	1.925	1.892	1.946	1.947	1.922	1.902	1.930	1.947	1.923	1.919	1.924	1.950	1.959	1.961	1.904	1.895	1.920	1.905
Ti	0.020	0.036	0.019	0.023	0.022	0.037	0.016	0.027	0.014	0.038	0.017	0.030	0.017	0.020	0.021	0.026	0.015	0.018
Al	0.106	0.135	0.085	0.068	0.103	0.123	0.105	0.083	0.112	0.106	0.117	0.065	0.071	0.066	0.148	0.165	0.118	0.131
Cr	0.011	0.006	0.003	0.003	0.006	0.001	0.016	0.013	0.026	0.003	0.026	0.001	0.002	0.000	0.014	0.005	0.021	0.031
Fe^{2+}	0.206	0.300	0.227	0.305	0.227	0.322	0.182	0.000	0.164	0.412	0.170	0.411	0.292	0.368	0.195	0.236	0.168	0.168
Mn	0.004	0.006	0.004	0.006	0.006	0.007	0.003	0.498	0.001	0.009	0.004	0.012	0.007	0.010	0.007	0.006	0.005	0.003
Mg	0.902	0.813	0.915	0.866	0.875	0.807	0.928	0.757	0.929	0.753	0.920	0.814	0.942	0.884	0.873	0.885	0.891	0.884
Ca	0.817	0.803	0.785	0.769	0.830	0.788	0.813	0.659	0.818	0.738	0.805	0.695	0.698	0.677	0.830	0.769	0.856	0.854
Na	0.014	0.022	0.014	0.013	0.020	0.017			0.010	0.024	0.007	0.017			0.005	0.014	0.004	0.006
Total	4.004	4.013	3.998	4.000	4.011	4.007	3.994	3.984	3.998	4.001	3.990	3.995	3.988	3.986	3.997	4.001	3.998	4.000
Mg#	0.814	0.730	0.801	0.740	0.794	0.715	0.836	1.000	0.850	0.646	0.844	0.664	0.763	0.706	0.817	0.789	0.841	0.840

FeO* is total iron as FeO.

Table 3. (Continued).

Rock	Dolerite						Basalt						Basalt					
Sample	#15						#28						#36					
Mineral	core	rim	core	rim	core	rim	core	rim	core	rim	core	rim	core	rim	core	rim	core	rim
SiO2	52.37	50.77	53.93	52.61	52.73	52.79	51.26	51.10	50.79	50.87	50.88	52.35	51.91	52.01	51.11	50.59	50.58	50.87
TiO2	0.76	0.84	0.53	0.68	0.57	0.83	0.67	0.81	0.81	0.78	0.61	0.65	0.76	0.81	0.63	0.84	0.59	0.78
Al2O3	2.75	5.02	1.78	1.60	2.44	1.42	2.15	2.47	2.14	2.43	2.14	1.27	2.27	1.42	2.12	2.98	2.22	2.22
Cr2O3	0.24		0.15	0.14	0.14	0.13	0.40	0.35	0.28	0.33	0.44	0.14	0.35	0.07	0.16	0.74	0.46	0.35
FeO	7.84	10.33	6.90	11.01	8.06	12.36	6.12	6.37	6.62	6.53	5.94	7.31	6.69	10.44	6.20	6.35	5.46	5.83
MnO		0.26	0.12	0.13	0.13	0.51								0.31	0.19	0.21		0.16
MgO	15.72	13.34	17.25	15.18	16.35	14.86	16.18	15.97	15.88	15.95	16.07	15.96	16.88	16.60	16.39	16.03	16.33	16.49
CaO	20.88	17.04	20.54	18.87	20.43	18.19	20.21	20.29	19.95	19.98	20.13	19.79	19.76	16.73	20.07	19.70	19.89	19.96
Na2O	0.17	1.14	0.10	0.25	0.08		0.14	0.09	0.18	0.11	0.06	0.56	0.11	0.00			0.41	
Total	100.74	98.74	101.29	100.46	100.95	101.07	97.14	97.46	96.65	96.99	96.27	98.03	98.73	98.38	96.88	97.44	96.06	96.66
O=	6	6	6	6	6	6	6	6	6	6	6	6	6	6	6	6	6	6
Si	1.921	1.907	1.953	1.953	1.929	1.957	1.936	1.926	1.933	1.927	1.938	1.966	1.929	1.957	1.936	1.908	1.930	1.929
Ti	0.021	0.024	0.014	0.019	0.016	0.023	0.019	0.023	0.023	0.022	0.017	0.018	0.021	0.023	0.018	0.024	0.017	0.022
Al	0.119	0.222	0.076	0.070	0.105	0.062	0.096	0.110	0.096	0.108	0.096	0.056	0.100	0.063	0.094	0.133	0.100	0.099
Cr	0.007	0.000	0.004	0.004	0.004	0.004	0.012	0.011	0.008	0.010	0.013	0.004	0.010	0.002	0.005	0.022	0.014	0.011
Fe^{2+}	0.240	0.324	0.209	0.342	0.247	0.383	0.193	0.201	0.211	0.207	0.189	0.230	0.208	0.328	0.197	0.200	0.174	0.185
Mn	0.000	0.008	0.004	0.004	0.004	0.016								0.010	0.006	0.007		0.005
Mg	0.860	0.747	0.931	0.840	0.892	0.821	0.911	0.897	0.901	0.901	0.912	0.893	0.935	0.931	0.925	0.901	0.929	0.932
Ca	0.821	0.685	0.797	0.750	0.801	0.722	0.818	0.820	0.813	0.811	0.821	0.797	0.787	0.674	0.814	0.796	0.813	0.811
Na	0.012	0.083	0.007	0.018	0.006		0.010	0.007	0.013	0.008	0.005	0.041	0.008				0.030	
Total	4.001	4.000	3.996	4.000	4.003	3.987	3.996	3.994	3.999	3.995	3.992	4.006	3.998	3.988	3.996	3.991	4.011	3.994
Mg#	0.782	0.697	0.817	0.711	0.783	0.682	0.825	0.817	0.810	0.813	0.828	0.795	0.818	0.739	0.824	0.818	0.842	0.834

FeO* is total iron as FeO.

Table 3. (Continued).

Rock	Basalt						Porphyric basalt						High-Mg andesite (Microphenocrysts)						High-Mg andesite (Microphenocrysts)					
Sample	#2701-1						#2701-2						#41						#42					
Mineral	core	rim	core	rim	core	rim	core	rim	core	rim	core	rim	core	rim	core	rim	core	rim	core	rim	core	rim	core	rim
SiO2	50.02	50.62	50.54	50.25	50.44	48.97	50.77	51.55	50.92	51.01	50.58	51.56	52.85	52.37	51.57	51.68	50.55	51.82	48.13	50.50	48.15	50.78	48.78	50.51
TiO2	0.47	0.49	0.58	0.62	0.54	0.87	0.48	0.90	0.92	0.84	0.67	0.74	0.30	0.33	0.50	0.40	0.70	0.48	1.66	0.86	1.42	0.90	1.06	0.56
Al2O3	2.58	2.51	2.07	2.60	2.16	2.66	3.33	1.73	2.23	2.83	2.35	1.77	0.88	1.09	2.04	1.79	2.72	1.91	6.09	4.13	4.55	3.38	4.57	2.86
Cr2O3	0.75	0.73	0.78	0.65	0.53	0.08	1.20	0.09	0.13	0.31	0.29	0.20	0.29	0.34	0.56	0.91	0.16	0.53	0.11	0.11	0.16	0.24	0.32	0.39
FeO	4.93	5.03	5.04	5.48	5.29	7.58	4.27	8.52	8.16	6.58	7.38	8.59	4.81	4.64	4.49	4.37	5.95	4.96	8.07	6.51	6.53	5.76	5.55	4.87
MnO																								
MgO	16.37	16.54	16.52	16.21	16.23	15.35	16.60	16.30	15.55	16.24	15.75	17.54	17.93	16.67	16.41	16.40	15.63	16.44	14.12	14.83	13.92	15.34	14.56	15.57
CaO	19.42	19.34	19.28	19.48	19.30	18.37	20.42	18.54	19.01	19.72	19.49	16.60	20.10	21.46	21.23	21.37	20.94	21.21	20.72	22.05	21.47	21.89	21.24	21.75
Na2O	0.12	0.00	0.00	0.04	0.06	0.10	0.02	0.07	0.12	0.06	0.10	0.00	0.00	0.06	0.05	0.11	0.10	0.02	0.23	0.20	0.11	0.15	0.11	0.11
Total	94.67	95.23	94.81	95.32	94.55	93.98	97.09	97.70	97.05	97.59	96.62	97.01	97.15	96.95	96.86	97.03	96.74	97.37	99.11	99.19	96.30	98.45	96.20	96.62
O=	6	6	6	6	6	6	6	6	6	6	6	6	6	6	6	6	6	6	6	6	6	6	6	6
Si	1.928	1.937	1.944	1.927	1.946	1.920	1.907	1.946	1.936	1.918	1.929	1.949	1.978	1.972	1.944	1.946	1.920	1.946	1.807	1.881	1.852	1.899	1.866	1.917
Ti	0.014	0.014	0.017	0.018	0.016	0.026	0.013	0.025	0.026	0.024	0.019	0.021	0.008	0.009	0.014	0.011	0.020	0.013	0.047	0.024	0.041	0.025	0.030	0.016
Al	0.117	0.113	0.094	0.117	0.098	0.123	0.147	0.077	0.100	0.126	0.106	0.079	0.039	0.048	0.091	0.080	0.122	0.084	0.269	0.181	0.206	0.149	0.206	0.128
Cr	0.023	0.022	0.024	0.020	0.016	0.003	0.036	0.003	0.004	0.009	0.009	0.006	0.009	0.010	0.017	0.027	0.005	0.016	0.003	0.003	0.005	0.007	0.010	0.012
Fe^{2+}	0.159	0.161	0.162	0.176	0.171	0.248	0.134	0.269	0.259	0.207	0.235	0.271	0.151	0.146	0.141	0.138	0.189	0.156	0.253	0.203	0.210	0.180	0.178	0.155
Mn																								
Mg	0.941	0.943	0.947	0.927	0.934	0.897	0.929	0.917	0.881	0.911	0.895	0.989	1.000	0.936	0.922	0.921	0.885	0.921	0.790	0.823	0.798	0.855	0.831	0.881
Ca	0.802	0.793	0.794	0.801	0.798	0.772	0.822	0.750	0.774	0.794	0.796	0.673	0.806	0.866	0.857	0.862	0.852	0.853	0.833	0.880	0.885	0.877	0.871	0.884
Na	0.009			0.003	0.004	0.008	0.001	0.005	0.009	0.004	0.007			0.004	0.004	0.008	0.007	0.002	0.017	0.014	0.008	0.011	0.008	0.008
Total	3.993	3.981	3.981	3.988	3.983	3.996	3.989	3.992	3.990	3.993	3.998	3.987	3.990	3.991	3.990	3.993	4.000	3.991	4.019	4.010	4.005	4.003	4.000	4.001
Mg#	0.855	0.854	0.854	0.840	0.845	0.783	0.874	0.773	0.773	0.815	0.792	0.785	0.869	0.865	0.867	0.870	0.824	0.855	0.757	0.802	0.792	0.826	0.824	0.850

FeO* is total iron as FeO.

Table 4. LA-ICP-MS trace element and REEs (ppm) data for clinopyroxenes from the Hangay greenstones.

Rock	Picrite	Basalt	Basalt	High-Mg andesite		
Sapmle	#12	#12	#36	#41	#41	#42
Mineral	Cpx	Rim	Cpx	Cpx	Amp	Cpx
Ti	2629	3793	3718	2151	16013	2979
V	277	368	276	232	712	195
Cr	4751	5489	1921	2075	63	1119
Co	49	48	50	38	62	30
Ni	150	155	168	66	78	60
Rb	0.02	0.02	0.01	0.19	5	11.90
Sr	17.41	19.00	19.32	32.48	271	116.08
Y	6.69	10.00	9.01	15.23	39	12.51
Zr	6.61	14.00	9.50	23.77	76.29	34.43
Nb	0.06	0.10	0.05	0.06	5.33	0.46
Ba	0.15	0.49	0.12	1.04	168.56	65.37
La	0.38	0.62	0.50	2.15	8.28	2.15
Ce	1.86	3.00	2.53	10.05	35.03	8.83
Pr	0.38	0.59	0.51	1.80	5.97	1.57
Nd	2.38	3.78	3.43	10.01	32.34	8.89
Sm	0.99	1.51	1.42	3.18	9.42	2.72
Eu	0.38	0.55	0.53	0.74	2.16	0.81
Gd	1.35	2.05	1.86	3.35	9.12	2.81
Tb	0.22	0.33	0.31	0.52	1.32	0.42
Dy	1.46	2.21	2.00	3.33	8.33	2.65
Ho	0.27	0.42	0.37	0.64	1.56	0.50
Er	0.71	1.10	0.97	1.68	4.09	1.33
Tm	0.09	0.15	0.13	0.23	0.54	0.18
Yb	0.59	0.94	0.80	1.48	3.44	1.16
Lu	0.08	0.13	0.11	0.20	0.44	0.16
Hf	0.33	0.70	0.45	1.21	3.24	1.35
Th	0.00	0.00	0.00	0.14	0.23	0.33
Ta	0.0023	0.0080	0.0034	0.01	0.29	0.03

Table 5. Representative microprobe analyses (wt%) of Chromian-spinel. The ferric iron content of spinel was estimated assuming spinel stoichiometry.

Rock	Basalt						Basalt						Basalt				Basalt			
Sample	#01						#34						#29				#2701-1			
Mineral	core	rim	core	rim	core	rim	core	rim	core	rim	core	rim	Core	Core	Core	Core	core	rim	core	rim
SiO_2	0.00	0.32	0.00	0.36	0.00	0.37	0.23	0.28	0.18	0.29	0.22	0.27	0.29	0.24	0.28	0.27	0.28	0.25	0.27	0.27
TiO_2	1.26	1.30	1.12	1.16	1.15	1.32	1.15	1.11	1.09	1.08	1.16	1.06	0.96	1.29	1.09	1.12	1.14	1.49	1.03	1.12
Al_2O_3	15.21	14.15	14.76	13.12	14.61	13.02	16.39	16.69	15.98	14.81	18.05	16.83	17.22	16.72	18.59	18.03	20.10	13.91	15.93	14.81
Cr_2O_3	44.33	45.20	44.59	44.93	44.67	44.10	43.98	41.62	42.29	41.70	41.35	41.06	42.73	35.49	40.72	39.41	36.92	36.47	39.28	37.80
FeO*	22.54	26.28	22.67	27.18	22.60	28.28	22.59	26.15	24.19	25.02	19.45	25.02	23.89	31.67	20.19	22.61	20.91	31.25	23.51	25.57
MnO	0.06	0.27	0.13	0.11	0.17	0.11	0.20	0.14	0.09	0.43	0.07	0.06	0.18	0.74	0.08	0.25	0.18	0.32	0.32	0.10
MgO	10.11	9.12	9.65	7.97	9.45	7.93	10.93	8.24	9.01	7.44	12.59	8.89	9.83	6.14	12.47	9.90	11.22	4.47	8.16	7.79
CaO	0.04		0.02		0.05		0.01	0.08	0.02	0.07	0.05	0.06	0.00	0.00	0.11	0.03	0.05	0.07	0.17	0.55
Total	93.55	96.64	92.94	94.83	92.70	95.13	95.48	94.31	92.85	90.84	92.94	93.25	95.10	92.29	93.53	91.62	90.80	88.23	88.67	88.01
O=	4	4	4	4	4	4	4	4	4	4	4	4	4	4	4	4	4	4	4	4
Si	0.000	0.011	0.000	0.012	0.000	0.013	0.008	0.010	0.006	0.010	0.007	0.009	0.010	0.008	0.009	0.009	0.009	0.009	0.010	0.010
Ti	0.032	0.033	0.029	0.030	0.030	0.034	0.029	0.028	0.028	0.029	0.029	0.027	0.024	0.034	0.027	0.029	0.029	0.042	0.028	0.031
Al	0.612	0.559	0.600	0.534	0.597	0.528	0.640	0.670	0.649	0.624	0.708	0.679	0.678	0.694	0.724	0.729	0.804	0.617	0.677	0.638
Cr	1.196	1.198	1.216	1.226	1.224	1.200	1.152	1.121	1.152	1.178	1.087	1.111	1.128	0.987	1.063	1.069	0.990	1.085	1.120	1.092
Fe^{3+}	0.128	0.156	0.126	0.155	0.120	0.178	0.135	0.133	0.129	0.120	0.133	0.137	0.127	0.234	0.141	0.125	0.129	0.195	0.127	0.189
Fe^{2+}	0.515	0.580	0.528	0.629	0.535	0.637	0.491	0.613	0.568	0.628	0.408	0.579	0.540	0.698	0.417	0.523	0.464	0.788	0.583	0.592
Mn	0.002	0.008	0.004	0.003	0.005	0.003	0.006	0.004	0.003	0.013	0.002	0.002	0.005	0.022	0.002	0.007	0.005	0.010	0.010	0.003
Mg	0.514	0.456	0.496	0.410	0.488	0.407	0.540	0.418	0.463	0.396	0.624	0.453	0.489	0.322	0.614	0.506	0.567	0.251	0.439	0.424
Ca	0.001	0.000	0.001	0.000	0.002	0.000	0.000	0.003	0.001	0.003	0.002	0.002	0.000	0.000	0.004	0.001	0.002	0.003	0.007	0.022
Total	3.000	3.000	3.000	3.000	3.000	3.000	3.000	3.000	3.000	3.000	3.000	3.000	3.000	3.000	3.000	3.000	3.000	3.000	3.000	3.000
Cr#	0.662	0.682	0.670	0.697	0.672	0.694	0.643	0.626	0.640	0.654	0.606	0.621	0.625	0.587	0.595	0.594	0.552	0.637	0.623	0.631
YCr	0.618	0.626	0.626	0.640	0.631	0.630	0.598	0.583	0.597	0.613	0.564	0.577	0.583	0.516	0.551	0.556	0.515	0.572	0.582	0.569
YFe3+	0.066	0.082	0.065	0.081	0.062	0.093	0.070	0.069	0.067	0.062	0.069	0.071	0.066	0.122	0.073	0.065	0.067	0.103	0.066	0.099
Mg#	0.500	0.440	0.484	0.394	0.477	0.390	0.524	0.406	0.449	0.387	0.604	0.439	0.475	0.316	0.596	0.492	0.550	0.241	0.430	0.417

FeO* is total iron as FeO.

Table 5. (Continued).

	Rock	Picrite						Picrite						Ferropicrite					
	Sample	#12						#12082602B						#31					
rim	Mineral	core	rim	core	rim	core	rim	core	rim	core	rim	core	rim	core	rim	core	rim	core	rim
0.27	SiO_2	0.20	0.28	0.20	0.21	0.28	0.27	0.32	0.23	0.26	0.33	0.27	0.30	0.28	0.00	0.00	0.30	0.45	0.39
1.12	TiO_2	1.01	1.12	0.94	1.34	0.98	0.94	1.12	1.15	1.06	0.95	1.18	1.10	1.36	1.50	1.49	1.40	1.59	1.30
14.81	Al_2O_3	17.33	14.68	17.26	16.74	17.70	16.65	16.22	14.94	14.67	14.37	16.62	16.21	13.41	11.92	14.47	16.07	14.55	11.93
37.80	Cr_2O_3	42.74	42.50	41.18	38.75	41.66	40.25	46.45	44.54	45.83	45.07	44.16	42.83	46.47	40.27	45.00	41.90	44.12	40.63
25.57	FeO*	21.39	27.56	25.12	30.02	24.95	29.14	21.67	23.97	20.33	23.80	18.62	22.95	22.08	33.83	20.03	21.84	20.02	30.11
0.10	MnO	0.25	0.29	0.14	0.03	0.18	0.32	0.14	0.42	0.16	0.04	0.30	0.09	0.09	1.33	0.08	0.17	0.08	0.92
7.79	MgO	11.24	7.62	9.87	7.08	8.75	5.55	11.21	8.72	10.59	8.68	12.80	9.62	10.41	1.25	12.37	11.04	12.23	3.79
0.55	CaO							0.02	0.06	0.09		0.04	0.05	0.00	0.06	0.11	0.00	0.11	0.03
88.01	Total	94.16	94.05	94.71	94.17	94.50	93.12	97.15	94.03	92.99	93.24	93.99	93.15	94.10	90.16	93.55	92.72	93.15	89.10
4	O=	4	4	4	4	4	4	4	4	4	4	4	4	4	4	4	4	4	4
0.010	Si	0.007	0.010	0.007	0.007	0.009	0.009	0.010	0.008	0.009	0.011	0.009	0.010	0.010	0.000	0.000	0.010	0.015	0.015
0.031	Ti	0.025	0.029	0.024	0.035	0.025	0.025	0.027	0.030	0.027	0.025	0.029	0.028	0.035	0.043	0.038	0.036	0.040	0.037
0.638	Al	0.681	0.599	0.681	0.678	0.704	0.690	0.624	0.605	0.592	0.588	0.649	0.653	0.539	0.538	0.574	0.644	0.579	0.533
1.092	Cr	1.126	1.163	1.089	1.053	1.112	1.119	1.198	1.209	1.241	1.236	1.156	1.157	1.254	1.219	1.197	1.126	1.178	1.217
0.189	Fe^{3+}	0.129	0.161	0.169	0.185	0.115	0.123	0.103	0.111	0.095	0.104	0.119	0.112	0.118	0.157	0.153	0.139	0.132	0.147
0.592	Fe^{2+}	0.467	0.637	0.534	0.678	0.589	0.734	0.488	0.577	0.488	0.586	0.397	0.544	0.512	0.926	0.411	0.482	0.434	0.807
0.003	Mn	0.007	0.009	0.004	0.001	0.005	0.010	0.004	0.012	0.005	0.001	0.008	0.003	0.003	0.043	0.002	0.005	0.002	0.030
0.424	Mg	0.558	0.393	0.492	0.363	0.440	0.291	0.545	0.446	0.541	0.449	0.632	0.490	0.530	0.071	0.621	0.559	0.616	0.214
0.022	Ca	0.000	0.000	0.000	0.000	0.000	0.000	0.001	0.002	0.003	0.000	0.001	0.002	0.000	0.002	0.004	0.000	0.004	0.001
3.000	Total	3.000	3.000	3.000	3.000	3.000	3.000	3.000	3.000	3.000	3.000	3.000	3.000	3.000	3.000	3.000	3.000	3.000	3.000
0.631	Cr#	0.623	0.660	0.615	0.608	0.612	0.619	0.658	0.667	0.677	0.678	0.641	0.639	0.699	0.694	0.676	0.636	0.670	0.695
0.569	YCr	0.582	0.605	0.562	0.550	0.576	0.579	0.622	0.628	0.644	0.641	0.601	0.602	0.656	0.637	0.622	0.590	0.624	0.642
0.099	YFe3+	0.067	0.084	0.087	0.096	0.060	0.064	0.053	0.058	0.049	0.054	0.062	0.058	0.062	0.082	0.079	0.073	0.070	0.077
0.417	Mg#	0.545	0.382	0.480	0.348	0.428	0.284	0.527	0.436	0.526	0.434	0.614	0.474	0.508	0.071	0.602	0.537	0.587	0.210

FeO* is total iron as FeO.

Table 5. (Continued).

Rock	Ferropicrite						High-MG andesite (Spl in Cpx)						High-MG andesite (Spl in Ol)						High-Mg andesite			
Sample	#32						#41												#42			
Mineral	core	rim	core	rim	core	rim	core	rim	core	rim	core	rim	core	rim	core	rim	core	rim	core	core	core	core
SiO_2	0.28	0.28	0.38	0.24	0.21	0.23	0.28	0.40	0.38	0.42	0.66	0.82	1.10	1.10	0.27	0.30	0.27	0.35	0.30	0.30	0.22	0.27
TiO_2	1.41	1.33	1.46	1.41	1.38	1.47	0.73	1.01	1.20	1.32	0.48	0.93	1.34	0.79	0.48	0.60	0.45	0.55	1.04	1.04	0.69	1.53
Al_2O_3	17.57	17.87	14.77	13.28	14.93	14.25	9.87	9.71	7.92	9.93	10.54	8.99	13.63	12.79	10.77	8.18	12.12	11.95	14.17	14.17	16.83	13.18
Cr_2O_3	39.94	39.04	43.99	44.35	43.70	43.52	45.46	42.91	41.74	42.49	44.85	40.38	37.44	44.05	49.21	46.19	49.63	49.43	37.86	37.86	40.24	36.38
FeO*	22.04	22.76	20.25	21.47	20.56	23.28	27.98	30.08	27.07	27.47	22.88	26.40	32.00	25.88	23.36	25.33	21.07	20.30	30.56	30.56	22.94	32.37
MnO	0.03	0.28	0.14	0.17	0.13	0.15	0.14	0.31	0.18	0.26	0.44	0.18	0.40	0.21	0.43	0.35	0.17	0.28	0.28	0.28	0.28	0.29
MgO	11.64	11.28	12.16	10.48	12.13	9.86	6.83	6.90	6.81	7.46	8.04	7.48	7.86	11.23	9.04	7.09	10.05	11.25	8.19	8.19	11.86	8.34
CaO	0.04	0.08	0.06	0.07	0.03	0.13	0.29	0.38	0.40	0.45	0.24	0.47	0.09	0.13	0.04	0.07	0.07	0.12	0.13	0.13	0.16	0.09
Total	92.95	92.92	93.21	91.47	93.07	92.89	91.58	91.70	85.70	89.80	88.13	85.65	93.86	96.18	93.60	88.11	93.83	94.23	92.53	92.53	93.22	92.45
O=	4	4	4	4	4	4	4	4	4	4	4	4	4	4	4	4	4	4	4	4	4	4
Si	0.009	0.009	0.013	0.008	0.007	0.008	0.010	0.015	0.015	0.015	0.025	0.032	0.038	0.037	0.009	0.011	0.009	0.012	0.010	0.010	0.007	0.009
Ti	0.036	0.034	0.037	0.037	0.035	0.038	0.020	0.028	0.035	0.037	0.013	0.027	0.035	0.020	0.013	0.017	0.012	0.014	0.027	0.027	0.017	0.040
Al	0.694	0.707	0.587	0.547	0.594	0.579	0.424	0.416	0.364	0.431	0.462	0.408	0.556	0.501	0.445	0.366	0.493	0.480	0.584	0.584	0.664	0.545
Cr	1.059	1.036	1.173	1.226	1.167	1.187	1.308	1.231	1.286	1.236	1.319	1.229	1.024	1.157	1.363	1.386	1.354	1.332	1.046	1.046	1.064	1.008
Fe^{3+}	0.157	0.171	0.139	0.136	0.154	0.142	0.208	0.269	0.250	0.229	0.143	0.246	0.274	0.230	0.148	0.191	0.111	0.136	0.295	0.295	0.222	0.347
Fe^{2+}	0.461	0.468	0.432	0.492	0.427	0.530	0.644	0.644	0.632	0.617	0.569	0.604	0.652	0.490	0.536	0.613	0.497	0.442	0.598	0.598	0.420	0.602
Mn	0.001	0.008	0.004	0.005	0.004	0.004	0.004	0.010	0.006	0.008	0.014	0.006	0.012	0.006	0.013	0.011	0.005	0.008	0.008	0.008	0.008	0.009
Mg	0.582	0.564	0.612	0.546	0.611	0.507	0.371	0.373	0.396	0.409	0.446	0.429	0.405	0.556	0.472	0.401	0.517	0.571	0.427	0.427	0.591	0.436
Ca	0.001	0.003	0.002	0.003	0.001	0.005	0.011	0.015	0.017	0.018	0.010	0.019	0.003	0.005	0.002	0.003	0.003	0.004	0.005	0.005	0.006	0.003
Total	3.000	3.000	3.000	3.000	3.000	3.000	3.000	3.000	3.000	3.000	3.000	3.000	3.000	3.000	3.000	3.000	3.000	3.000	3.000	3.000	3.000	3.000
Cr#	0.604	0.594	0.666	0.691	0.663	0.672	0.755	0.748	0.779	0.742	0.741	0.751	0.648	0.698	0.754	0.791	0.733	0.735	0.642	0.642	0.616	0.649
YCr	0.554	0.541	0.618	0.642	0.609	0.622	0.674	0.643	0.677	0.652	0.685	0.653	0.552	0.613	0.697	0.713	0.691	0.684	0.543	0.543	0.546	0.531
YFe3+	0.082	0.089	0.073	0.071	0.081	0.074	0.107	0.140	0.132	0.121	0.074	0.131	0.148	0.122	0.076	0.098	0.057	0.070	0.153	0.153	0.114	0.183
Mg#	0.558	0.547	0.586	0.526	0.589	0.489	0.365	0.367	0.385	0.399	0.439	0.415	0.383	0.532	0.468	0.395	0.510	0.564	0.416	0.416	0.585	0.420

FeO* is total iron as FeO.

Table 6. Representative microprobe analyses (wt%) of hornblende. The ferric iron content of spinel was estimated assuming spinel stoichiometry.

Rock	High-Mg andesite (Microphenocrysts)						
Sample	#41						
Mineral	core	rim	core	rim	core	rim	core
SiO_2	40.82	41.05	42.50	42.60	41.43	42.68	43.18
TiO_2	3.35	2.78	2.82	2.83	3.25	2.98	2.47
Al_2O_3	11.29	10.94	10.61	10.86	11.42	11.16	9.51
Cr_2O_3	0.03	0.06	0.08	0.10	0.09	0.05	0.01
FeOT	10.44	9.54	10.04	9.38	11.67	10.12	10.71
MgO	13.90	13.85	14.64	14.85	13.38	14.85	14.32
CaO	11.04	11.00	11.45	11.79	11.15	11.16	10.84
Na_2O	2.75	2.51	2.49	2.61	2.73	2.40	2.30
K_2O	0.61	0.70	0.76	0.72	0.72	0.72	0.56
Total	94.24	92.42	95.39	95.74	95.85	96.13	93.90
O=	23	23	23	23	23	23	23
Si	6.22	6.34	6.37	6.35	6.24	6.33	6.56
Ti	0.38	0.32	0.32	0.32	0.37	0.33	0.28
Al	2.03	1.99	1.87	1.91	2.03	1.95	1.70
Cr	0.00	0.01	0.01	0.01	0.01	0.01	0.00
Fe^{2+}	1.33	1.23	1.26	1.17	1.47	1.26	1.36
Mg	3.16	3.19	3.27	3.30	3.00	3.29	3.24
Ca	1.80	1.82	1.84	1.88	1.80	1.77	1.77
Na	0.81	0.75	0.72	0.76	0.80	0.69	0.68
K	0.12	0.14	0.15	0.14	0.14	0.14	0.11
Total	15.85	15.78	15.81	15.82	15.85	15.77	15.70
Mg#	0.70	0.72	0.72	0.74	0.67	0.72	0.70

T-total Fe as FeO.